UNIVERSIDADE Ð COIMBRA

João Pedro Dias Aveiro

ASSESSING THE PHOTOMETRIC AND ASTROMETRIC CAPABILITIES OF THE ELT METIS IMAGER ON THE CENTRE OF THE MILKY WAY

Dissertação no âmbito do Mestrado em Astrofísica e Instrumentação para o Espaço orientada pelo Doutor Carlos Correia e pelo Professor Doutor Nuno Peixinho, e apresentada ao Departamento de Física e ao Departamento de Matemática da Faculdade de Ciências e Tecnologia da Universidade de Coimbra

Setembro de 2023

Abstract

Assessing the photometric and astrometric capabilities of the ELT METIS Imager on the centre of the Milky WAY

by João Aveiro

The forthcoming generation of Extremely Large Telescopes (ELTs), boasting apertures ranging from 25 to 40 meters, promises unparalleled advancements in astronomical imaging and spectroscopy. The European Southern Observatory's Extremely Large Telescope (ESO ELT) stands as a pinnacle project in this new era of ground-based observatories, poised to catalyse transformative scientific discoveries.

Improvements in astrometry and photometry, derived from the expected increase in sensitivity and angular resolution of Extremely Large Telescopes (ELTs), will empower otherwise challenging astronomical observations, such as imaging closed-packed stellar clusters and the analysis of stellar orbits near the supermassive object Sagittarius A* at the centre of the Milky Way. The ample capabilities of the Extremely Large Telescope (ELT) Mid-infrared ELT Imager and Spectrograph (METIS) in the mid-infrared (MIR) photometric bands make it the ideal instrument for the study of these science cases. However, no estimation of the predicted astrometric performance of this instrument is available in the literature. As such, a critical need exists for an assessment of METIS's anticipated astrometric performance to gauge its suitability for diverse observation targets.

This thesis undertakes an in-depth evaluation of the capabilities of the METIS instrument in L' band imaging. With this purpose in mind, a pipeline for generating realistic images of the Galactic Centre is first introduced. Subsequently, the inverse problem is tackled, leveraging a well-established photometry and astrometry toolkit to analyse the generated synthetic images and extract precise position and flux data of stellar sources.

From the analysis conducted herein, an estimate of the astrometric precision for the METIS imager in L' is provided. Furthermore, the feasibility of using existing general-purpose software pipelines for performing high-precision astrometry is explored. Finally, this study includes a thorough investigation of extra error sources that were not previously taken into account, resulting in the development of a detailed astrometric error budget.

Keywords: *Extremely Large Telescope, Mid-infrared ELT Imager and Spectrograph, high-precision astrometry, Galactic Centre, mid-infrared astronomy.*

Resumo

Assessing the photometric and astrometric capabilities of the ELT METIS Imager on the centre of the Milky WAY

by João Aveiro

A próxima geração de Telescópios Extremamente Grandes (ELTs), com aberturas variando de 25 a 40 metros, promete avanços sem paralelo na aquisição de imagem e espectroscopia astronômicas. O Extremely Large Telescope (ELT) do Observatório Europeu do Sul (ESO) destaca-se como um projeto de destaque nesta nova era de observatórios terrestres, pronto para catalisar descobertas científicas transformadoras.

As melhorias em astrometria e fotometria, decorrentes do aumento esperado na sensibilidade e resolução angular dos ELTs, possibilitarão realizar observações astronômicas desafiantes, como a observação de aglomerados estelares densamente povoados e a análise das órbitas estelares próximas ao objeto supermassivo Sagitário A* no centro da Via Láctea. As amplas capacidades do instrumento METIS (Mid-infrared ELT Imager and Spectrograph) do ELT nas bandas fotométricas de infravermelho médio (MIR) fazem dele o instrumento ideal para o estudo destes casos científicos. No entanto, não existe estimativa do desempenho astrométrico previsto deste instrumento na literatura. Como tal, existe uma necessidade crítica de avaliar o desempenho astrométrico esperado do METIS e a sua adequação para diversos alvos de observação.

Esta tese tem como objetivo avaliar detalhadamente as capacidades do instrumento METIS em observações diretas da banda L'. Com este propósito em mente, começa-se por introduzir o processo de geração de imagens realistas do Centro Galáctico. Subsequentemente, o problema inverso é abordado, utilizando um conjunto bem estabelecido de ferramentas de fotometria e astrometria para analisar as imagens sintéticas geradas e extrair dados precisos de posição e fluxo de fontes estelares.

A partir da análise realizada nesta tese, é fornecida uma estimativa da precisão astrométrica para as observações diretos do METIS na banda L'. Adicionalmente, é explorada a viabilidade de se utilizar softwares de uso geral existentes para análise de astrometria de alta precisão. Por fim, este estudo inclui uma análise alargada de fontes de erros adicionais que não foram previamente consideradas, resultando no desenvolvimento de um detalhado orçamento de erros astrométricos.

Palavras-Chave: *Extremely Large Telescope, Mid-infrared ELT Imager and Spectrograph, astrometria de alta-precisão, Centro Galático, astronomia de radiação infravermelha média.*

Contents

List of Figures

Acronyms

AO adaptive optics

CFO common fore optics

CLI command-line interface

DIT detector integration time

DL diffraction limit

ELT Extremely Large Telescope

ELTs Extremely Large Telescopes

ePSF effective PSF

ESO European Southern Observatory

METIS Mid-infrared ELT Imager and Spectrograph

MIR mid-infrared

NIR near-infrared

PSF point spread function

SCAO single-conjugate adaptive optics

SNR signal-to-noise ratio

SR Strehl ratio

STScI Space Telescope Science Institute

VLT Very Large Telescope

Chapter 1

Introduction

The genesis of this thesis is motivated by a novel generation of $25 - 40$ m-class ground-based astronomical observatories - the Extremely Large Telescopes (ELTs) - with first-light expected in the current decade. Specifically, the focus of this work is geared towards the European Southern Observatory (ESO) Extremely Large Telescope (ELT) and, more precisely, the astrometric capabilities of the first-light instrument Mid-infrared ELT Imager and Spectrograph (METIS), which will operate in photometric bands of wavelength $\sim 3 - 14\,\mu$m.

The objective of this introductory chapter is to contextualise the topics discussed in this thesis and provide a general overview of its contents and overall objectives going forward. This introduction starts by briefly describing the historical background that preceded and motivated the inception of these next-generation observatories. Following on, a more detailed overview of ELTs will be presented, describing the overall characteristics and technical difficulties of such instruments. Lastly, an overview of technical aspects, characteristics, and science objectives of the METIS will be detailed at the end of this chapter, leading to the description of the fundamental objective of this thesis and its structure.

Before going further, it should be noted that in this work only *relative astrometry* is addressed. As such, the term *astrometry* is always employed in this sense.

The inception of astronomical observation

For millennia, the stars have been the object of great wonder and mystery for all of humankind, whilst also serving as the cradle of great scientific achievements. No more than the unaided eye and the relentless work of names such as Claudius Ptolemy and Nicolaus Copernicus allowed for great advancements in our knowledge about outer space and our own world.

Nevertheless, it was the advent of the telescope in the 17th century, which inception and numerous improvements we owe to the great minds of the likes of Lippershey, Galileo, Kepler, and Newton, that the manifest limitation of the human eye was overcome. As a result, centuries of significant discoveries and scientific breakthroughs ensued, elevating electromagnetic observation as the primary and undisputed source of knowledge about our Universe - which only recently has been joined by another contender with the dawn of gravitational wave detection.

For the last centuries, the clear focus was set on building larger telescopes (more precisely, of larger aperture diameter, D), motivated by the resulting increase in angular resolution ($\propto \lambda/D$) and light collecting area ($\propto D^2$).

This limitation was, for the most part, lifted by the development of adaptive optics (AO) systems for atmospheric compensation in the second half of the 20th century [4]. In turn, this development has enabled the current era of large aperture (~ 10 m) ground-based telescopes.

Current generation telescopes

Currently, there are a plethora of telescopes and observatories, both ground-based and space-based, in ample operation and taking part in state-of-the-art scientific research. Although it is not the purpose of this work to extensively analyse the availability and capabilities of current-generation observatories, it is essential to address some of the most competitive instruments which have partaken in the astronomical revolution of the past decades, namely in the context of this work - i.e. high-precision astrometry.

ESO Very Large Telescope (VLT)

The Very Large Telescope (VLT) is ESO's current flagship facility in operation for ground-based astronomy, located in Cerro Paranal in the Atacama Desert (Chile). It is comprised of an array of four main Unit Telescopes (UT) with 8.2 m primary mirrors, as well as four movable 1.8 m Auxiliary Telescopes (AT). These telescopes are fitted with a multitude of instruments, providing ample direct imaging and spectrographic capabilities from the visible to the mid-infrared (MIR). Additionally, it is also possible to operate both the UT and the AT arrays together on the basis of interferometry with the Very Large Telescope Interferometer (VLTI).

The VLT has empowered numerous high-impact astronomical discoveries over the years[1]. A key motivator of this thesis is the work related to the monitoring and study of stellar orbits around the supermassive compact object Sagittarius A* at the centre of the Milky Way [5, 6], in works that motivated the award of the 2020 Nobel Prize in Physics[2] to Reinhard Genzel.
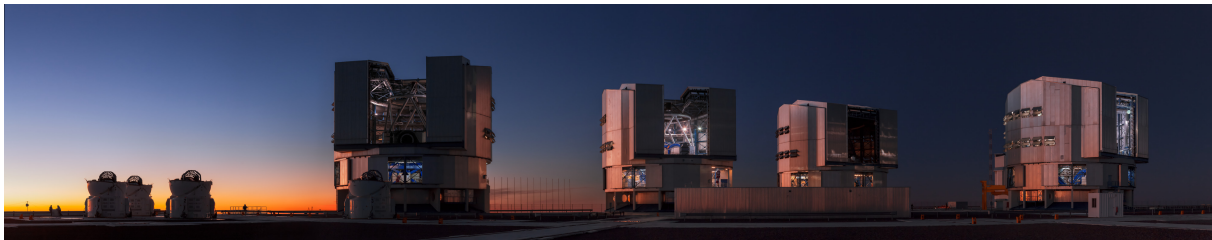
Figure 1.1: *ESO Very Large Telescope (VLT)* (Credit: ESO)

W. M. Keck Observatory

The W. M Keck Observatory, located at the summit of the Mauna Kea volcano (Hawaii, United States of America), consists of two twin 10 m telescopes, making them some of the largest in the world in operation. Over the years, it has also contributed to invaluable scientific findings[3]. In symbiosis with the VLT, it has a critical in the study of the Galactic Centre, most notably in the analysis of the dynamics near Sagittarius A* [7, 8]. These are key motivators for the award of the 2020 Nobel Prize in Physics to Andrea Ghez.

In the crowded centre of the Milky Way, the W.M. Keck telescopes have achieved an astrometric centroiding uncertainty of $\approx 200\,\mu$as in the near-infrared (NIR) [8]. In [6] a precision $\approx 300\,\mu$as is reached with the VLT. These achievements require extensive calibration efforts and rely mostly on point spread function (PSF)-fitting approaches to perform astrometry and photometry.

---

[1]See https://www.hq.eso.org/public/science/top10/.

[2]See https://www.nobelprize.org/prizes/physics/2020/summary/.

[3]See https://astrobiology.nasa.gov/missions/keck/.

Figure 1.2: *W. M. Keck Observatory* (Credit: W.M. Keck Observatory)

The limiting factors for astrometry in the Galactic Centre are detailed in [9]. This work also identifies the ability to extract the PSF from the scientific images as critical in improving astrometric performance. It is also proposed to complement the PSF extracted from the science field with techniques such as PSF reconstruction from AO wavefront sensor data - e.g. [10]. Nevertheless, $\approx 100 - 200\,\mu as$ is defined as the expected astrometric precision limit achievable in direct imaging of crowded fields with this class of telescopes, only surpassable with larger apertures or interferometric approaches [9]. Indeed, the VLTI Gravity instrument [11] has achieved sub-$100\,\mu as$ precision at an interferometry baseline of more than $100\,m$ [12]. Nonetheless, with a limiting magnitude K = 20 and restricted to NIR, this instrument is not competitive with ELTs with considerably larger collecting area and able to operate in other photometric bands, e.g. L', M, N (MIR) [13].

Next-generation Extremely Large Telescopes (ELTs)

The era of the extremely large telescopes (ELTs) is now at its dawn. These telescopes will provide unprecedented capabilities compared to current observatories, mainly due to their large aperture ($\sim 25 - 40$m) and state-of-the-art instrumentation.

The three main ELTs proposals under development are:

- The **Giant Magellan Telescope (GMT)**, developed by an international consortium mostly led by several American universities and research institutions, is located in the Las Campanas Observatory (Chile) and will encompass a $25\,m$ primary mirror;

- The **Thirty Meter Telescope (TMT)**, also lead by an international consortium, is planned to be constructed at Mauna Kea, Hawaii (U.S.A);

- The **Extremely Large Telescope (ELT)**, an endeavour by the European Southern Observatory, with a $39\,m$ primary mirror and is under construction in the Cerro Armazones (Chile).

All these telescopes are planned to include multiple state-of-the-art instruments covering wavelengths from the visible to the mid-infrared (MIR), as well as advanced adaptive optics systems allowing for diffraction-limited performance in most cases. For a more detailed discussion of these instruments and other proposals of ELTs see [14].

The Extremely Large Telescope

The European Southern Observatory (ESO) Extremely Large Telescope (ELT) is a groundbreaking astronomical observatory currently under construction in the Atacama Desert of northern Chile. At approximately $39\,m$ in diameter, its main segmented mirror will be the largest among the three ELTs under construction and will provide unprecedented angular resolution and light-gathering capabilities. After completion, it will include three first-light scientific instruments:

- High Angular Resolution Monolithic Optical and Near-infrared Integral field spectrograph (**HARMONI**)

- Mid-infrared ELT Imager and Spectrograph (**METIS**)

- Multi-AO Imaging Camera for Deep Observations (**MICADO**)

While the HARMONI will be focused on integral field spectroscopy work, the METIS and MICADO will be the main imagers empowering the ELT, each catering for different photometric bands of the electromagnetic spectrum.
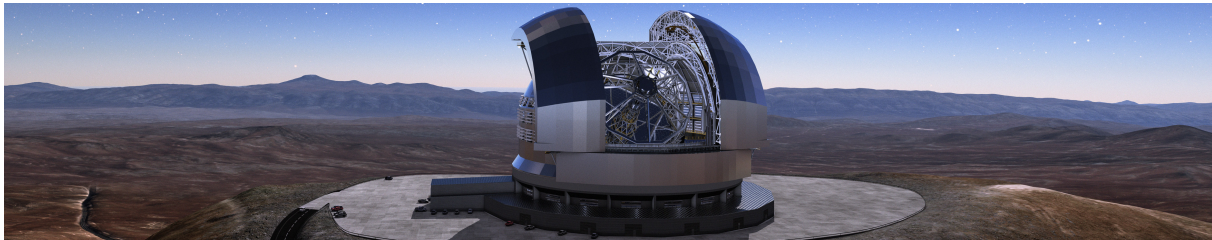
Figure 1.3: *Extremely Large Telescope (ELT)* (Credit: ESO)

The Mid-infrared ELT Imager and Spectrograph (METIS)

Of the planned first-light ELT instruments, the METIS will be the only providing diffraction-limited imaging and spectrography in the mid-infrared L'/M ($\sim 2.9 - 5.3\,\mu$m), and N ($\sim 7.6 - 13.8\,\mu$m) bands.

Science cases

Several scientific cases have been identified for this instrument [13, 15], such as:

- Study of the Galactic Centre

- Proto-planetary disks and planet formation

- Analysis of the properties of exoplanets

- Growth of Supermassive Black Holes

- Formation history of the Solar System

- High-mass star formation and evolution

Of these, the study of the Galactic Centre is of seminal importance for this work, encompassing several scientifically significant topics of paramount importance [13]. These include e.g. the study of stellar dynamics around the Sagittarius A*, as well as the formation and evolution of massive young star clusters located in close proximity. Beyond the central stellar cluster, the circumnuclear ring of ionised gas and warm dust also exhibits brightness in the MIR, and is another interesting target for observation. Finally, the capabilities of METIS will empower the study of the interstellar medium, e.g. with the analysis of absorption lines and thin dust filaments. More details of these and other science goals are presented in [13], as well as a vast list of literature references motivating these goals.

Instrument baseline

Deriving from the requirements imposed by the proposed science-cases, the following instrument baseline was defined:

1. Diffraction-limited imagers for both L'/M and N bands, with a field-of-view of about $11'' \times 11''$ and $18'' \times 18''$, respectively. These allow for coronography (L' and N), low-resolution long slit spectroscopy (all bands), and polarimetry (N band).

2. An integral field unit (IFU) high-resolution spectrograph for the L'/M bands, with a field of view of approximately $0.4'' \times 1.5''$ and spectral resolution $R \sim 100\,000$.

The diffraction-limited resolution is achieved by the implementation of an single-conjugate adaptive optics (SCAO) system.

The role of the METIS in high-precision astrometry

The improvements in angular resolution and collecting power brought by the ELTs is expected to have a profound impact in precision astrometry [16]. In [17], it is estimated that 30 m-class AO-enabled telescopes are in theory able to achieve astrometric precisions of the order of $\sim 10\,\mu\text{as}$ or below, although on the premise of careful characterisation and control of systematic errors. This objective is also identified e.g. in the MICADO baseline targets [18], though the inherent calibration difficulty is reiterated and a more conservative precision of $\sim 50\,\mu\text{as}$ is often assumed. This value is in agreement with the astrometric error budget provided in [16]. For the Thirty Meter Telescope (TMT), a detailed error budget analysis predicts $\sim 40\,\mu\text{as}$ of astrometric precision, granted the presence of several calibration and science objects in the field-of-view [19]. Although the 10 µas target seems unachievable in the initial configuration of upcoming ELTs, the expected astrometric precision of $\sim 40-50\,\mu\text{as}$ makes these observatories highly competitive with space-borne alternatives[20].

MICADO, specifically, is designed to leverage the scale of the ELT for the specific goal of achieving high-precision astrometry [18]. The METIS instrument, despite sharing the main optical train with MICADO - and thus harnessing the outstanding angular resolution and collecting power of the ELT - was not designed with a similar main goal. Nevertheless, the METIS is unmatched in its imaging capabilities in the MIR. This will allow to extend the spectral coverage of the study of the Galactic Centre with the ELT, providing direct imaging and spectroscopic observations, which are symbiotic with the other instruments.

An in-depth analysis of the astrometric capabilities of the METIS has not been addressed in the literature. Motivated by its unique capabilities in the study of the galactic centre, it is of great scientific importance to analyse the astrometric performance of this instrument, including estimating an astrometric error budget detailing the main limiting factors in achievable performance.

Objectives & Structure of this work

The core objective of this work is to study the astrometric performance of the ELT METIS instrument in direct imaging in the L' band, with the specific target of the galactic centre having been selected for this purpose. This study encompasses the generation and astrometric analysis of simulated images provided by the L'/M band imager, as well a review of the system properties and estimation of the astrometry error budget. An overview of the structure of this work is now presented.

Generating realistic images of the centre of the Milky Way

Due to the ongoing construction of ELT and without an existing analogue from which one may base their analysis, the availability of data products - e.g. direct images, observed spectra - is restricted to that synthetically generated. Since the credibility of any scientific analysis is highly dependent on the rigour and realism of the data utilised, the first of the following chapters of this work focuses precisely on this: generating high-quality synthetic images based on the properties of the ELT METIS instrument. In Chapter 2, a complete description of the pipeline used for the generation is provided, along with various tests and validation of its correctness. At last, several images are obtained using the methods described.

Extracting point sources from images

Following the description of the synthetic image generation, the focus is geared towards the methodology of the inverse problem, that is, extracting point sources from the said images. In Chapter 3, a brief summary of readily available software for photometric and astrometric work is provided, followed by a more descriptive overview of the specific software pipeline subsequently utilised in this work.

   The focus on readily available astrometry/photometry extraction software is motivated by two factors:

1. No custom image reduction and astrometry/photometry pipelines for this specific instrument are publicly or easily available to the general scientific community;

2. It is important to evaluate how well-established, general-purpose astrometry pipelines fare in analysing next-generation ELTs images.

   The last point is particularly pertinent since widely used photometry/astrometry software, such as DAOPhot [21] and SExtractor[22], have been developed in the 1980s and 1990s, in an era where adaptive optics was still an early development and generally the available telescopes were smaller. The scale of the ELTs, the use of segmented mirrors and active optics, and the ample use of adaptive optics result in much more complex PSFs. As a result, it is critical to analyse the feasibility of using the PSF-fitting capabilities of these software packages for high-precision astrometry. Hence, this is assumed to be a secondary research goal of this work.

Analysis of the astrometric performance

Having discussed the methodology to approach both the direct and the inverse problems presented in the previous chapters, the end goal of this work is finally addressed in Ch. 4, i.e. estimating the astrometric performance of the METIS in direct imaging of the Centre of our Galaxy. With this purpose in mind, in Sec. 4.1, the generated images are analysed with the proposed photometry/astrometry pipeline and the expected astrometric precision in simulated data is estimated. Additionally, the performance and limitations of the astrometry pipeline are addressed in this section. Subsequently, in Sec. 4.2, a more in-depth error budget, including effects not considered in the simulated images is, defined from both theoretical considerations and literature review. This more detailed error estimation is compared with MICADO, and the importance of the METIS for high-precision astrometry is contextualised.

Conclusions and Outlook

At last, a brief summary of the results achieved in this work is presented in Ch. 5, along with a final discussion addressing the research objectives of the present work. Additionally, various remarks motivating future work are summarised.

Chapter 2

The direct problem: Generating realistic images of the Galactic Centre

The observation of an arbitrary object by an imaging system might be described by:

$$I_{im}(x,y) = \text{PSF}(x,y) * O(x,y) + \xi(x,y) \qquad (2.1)$$

where PSF is the system point spread function, O is the target object spatial flux distribution function, ξ is the noise component, x and y angular position in the sky projected on the system's focal plane, and $*$ is the convolution operator. However, this description largely masks the precise definition and specificities of each of these quantities, of which a correct description is required.

With this purpose in mind, a more detailed overview of the pipeline used for image generation is first presented. This is followed by a more careful depiction of each of its building blocks, such as the definition of the point-spread function used, the composition and properties of the optical train of the ELT/METIS system, and a description of the imaging detector effects. With this, realistic images for the proposed system based on a point-source object catalogue of the centre of the Milky Way are attained.

Simulating the ELT METIS instrument

The images expected to be obtained by the METIS LM-band imager system are simulated using a modified version of the `ScopeSim` package [23], consequently relying on the system parameters - i.e. optical train definition, detector model characteristics, etc. - provided by the associated `irdb` package [24].

In this work, only unresolved point sources are considered. These are specified in a source catalogue defining their position in the sky and the respective monochromatic flux for $\lambda = 3.785\mu$m (L' photometric band). The image generation pipeline used to generate realistic observations of this target implemented closely follows the model presented in (2.1). We start by considering a discrete frame of the exact dimensions and plate scale as the METIS LM-band imager detector, onto which each point source in the catalogue is positioned, disregarding the system PSF or any other effects. This frame - henceforth referred to as the *point-source frame* - is then scaled by the optical efficiency of both the atmosphere and the optical train comprised of the ELT system and the METIS instrument. Thereupon, the convolution of this frame with the field-varying system PSF is computed, and the resulting image is combined with a background frame of atmospheric background and optical element thermal emission contributions. It is then applied to the combined frame all the additional detector effects and characteristics, such as its quantum efficiency, various noise contributions, and linearity response.

2.1   System point spread function

The point spread function (PSF) describes the impulse response of a focused optical system. More intuitively, the PSF of a system defines the angular distribution resulting from a point source - e.g. unresolved stars. Its correct depiction is crucial for any optical simulation task since it plays a key role in the process of image formation - see Eq. (2.1).

In this section, the METIS PSF is presented against the backdrop of the difficulties of imaging through the atmosphere and the improvements brought upon by adaptive optics correction, which is a key element for achieving high-resolution imagery with any large-scale ground-based telescope. Additionally, some technical aspects of using PSF arrays in digital image simulation and processing are addressed, namely with respect to pixel rescaling - or *resampling* - and the modelling of spatial variability.

Imaging through turbulence

The Earth's atmosphere is intrinsically coupled to any astronomic observation achieved with any ground-based telescopes. In the widely successful Kolmogorov turbulence model [25], the atmosphere is modelled by an energy transfer process in which the energy resulting from wind shear or convection in large-scale structures of the atmosphere is transferred to smaller-scale structures until the turbulent regime is not sustainable, upon which it is dissipated as heat. This dissipation is achieved for small, turbulent eddies achieving a dimension defined as l_0, known as the inner-scale of the turbulence, and which are considered to be statistically homogenous, isotropic, and independent of the large-scale structure.

Effects such as this turbulent motion and temperature fluctuations cause variations in the refraction index of the atmosphere, consequently originating phase distortions in the propagated wavefront of an astronomical source. The mean square wavefront phase variance over the diameter of the telescope pupil, D, is estimated by [26]:

$$\sigma_1^2 \approx 1.03(D/r_0)^{5/3} \tag{2.2}$$

with r_0 the Fried parameter, derived from [27]. This can be interpreted as the lateral distance over which the wavefront phase is highly correlated[1] [1].

In this regime, an observed point source object will be imaged as a multitude of small speckles of angular size $\propto \lambda/D$ resulting from interference within the telescope's aperture diameter, D, spread over an angle $\propto \lambda/r_0$. Note, however, that r_0 is a statistical parameter which varies quickly in time - such as the structure of the atmospheric turbulence. As a result, the speckle pattern will differ during the course of long exposures and the integrated intensity of a point source imaged through turbulence will result in an unresolved profile of width $\propto \lambda/r_0$ - also known as the *seeing disk* - see Fig. 2.1.

This parameter is statistical in nature and depends on the atmosphere's properties; for normal atmospheric conditions at a good observation site, $r_0 \sim 1\,\text{m}$ for the L' band[2].

Adaptive optics

The impact of atmospheric turbulence on astronomical observations can be minimised by wavefront compensation, achieved in practice with adaptive optics (AO) systems [4] - see Fig. 2.2.

---

[1]In fact, note that for $D = r_0$ one gets $\sigma_1^2 \approx 1\,\text{rad}^2$, that is, r_0 is the length scale for which the variance is approximately one square radian.

[2]Assuming $r_0 \sim 10\,\text{cm}$ for $\lambda = 500\,\text{nm}$ [28]. To extrapolate to L', take into consideration $r_0 \propto \lambda^{6/5}$ [29].
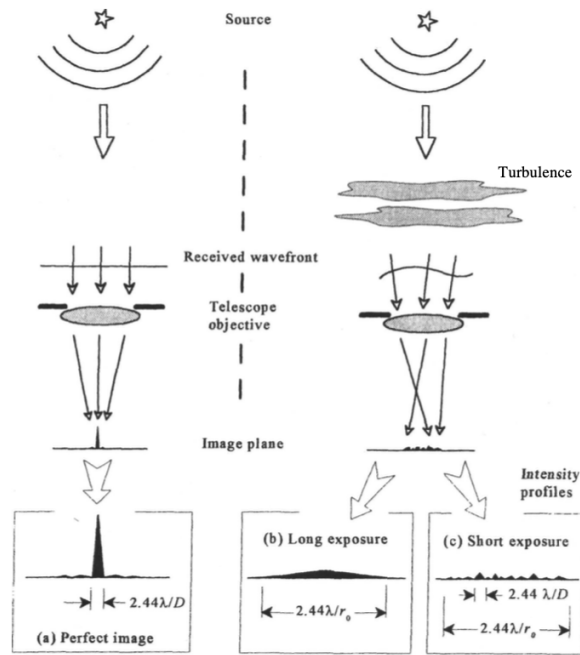
Figure 2.1: Effects of turbulence on the image of a star. *From: Hardy (1998)*[1].

The working principle of this technology resides in the inclusion of a wavefront corrector - usually a deformable mirror - which compensates the optical path difference incurred by the atmospheric turbulence in the imaged wavefront. Other required components include a wavefront sensor, which is responsible for the estimation of the wavefront distortion from a guide source, as well as the control system, which manages the AO system by estimating and delivering the control signal for the corrective devices based on the wavefront sensor reading, amongst other functionality.
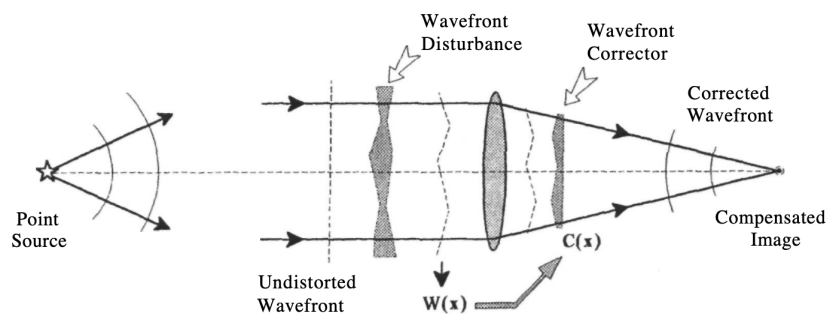
Figure 2.2: Principle of wavefront compensation. *From: Hardy (1998)* [1].

Usually, the successful sensing of the wavefront by the wavefront sensor relies on the presence of a guide source, such as an unresolved reference star. Since this is not always easily achievable, more recent developments opt to include laser beacons, which reflect on the atmosphere and produce laser guide stars (LGS). Nevertheless, for the METIS instrument, a straightforward single conjugate adaptive optics (SCAO) system is implemented, relying on a single natural guide-star (NGS).

One limitation of adaptive optics derives from the fact that from a certain angular separation, the turbulence becomes highly uncorrelated. This results in the correction estimated along a certain direction - namely, on axis with the guide star - not being optimal for the observation target, which might be located at an angular distance of several seconds of arc. This effect is

commonly known as *anisoplanicity* or *isoplanatic error*, and its practical effect on an observation amounts to a loss in the quality of the AO correction variable across the field - see Fig. 2.3. In turn, this limitation results in a degradation of the peak of PSF, leading to a reduction in the peak intensity of point sources and a decrease of their signal-to-noise ratio (SNR). A good measure for this effect is the Strehl ratio (SR), defined as:

$$SR = \frac{PFS(0,0)}{PFSDL(0,0)} \tag{2.3}$$

where PFS is the real system PSF and PFS_{DL} is the diffraction limited PSF.

In practice, the SR derived from an AO system is far from unity, due not only to the effect of anisoplanatism but also other physical and technical limitations - see [29].

The relative impact (or scaling factor) on the Strehl ratio due to anisoplanicity is estimated by [29]:

$$R \propto e^{-(\theta/\theta_0)^{5/3}} \tag{2.4}$$

where θ is the offset angle between the guide source and the observation target, and:

$$\theta_0 = 0.314 \frac{r_0 \cos\gamma}{\bar{h}} \tag{2.5}$$

is the isoplanatic angle [29], which is a function of the Fried parameter, r_0, the zenith angle, γ, and a weighted average of the turbulent atmospheric layers altitude, $\bar{h}$.

For a guide source at zenith and assuming general values of $r_0 = 1.0\,\text{m}$ (L') and $\bar{h} = 2\times10^3\,\text{m}$, Eq. (2.5) leads to:

$$\theta_0 \approx 32''$$

For e.g.[3] $\theta = 6.0''$, from Eq. (2.4) this results in :

$$R \approx 0.945$$

i.e. a decrease of about $5.5\,\%$ of the Strehl ratio.
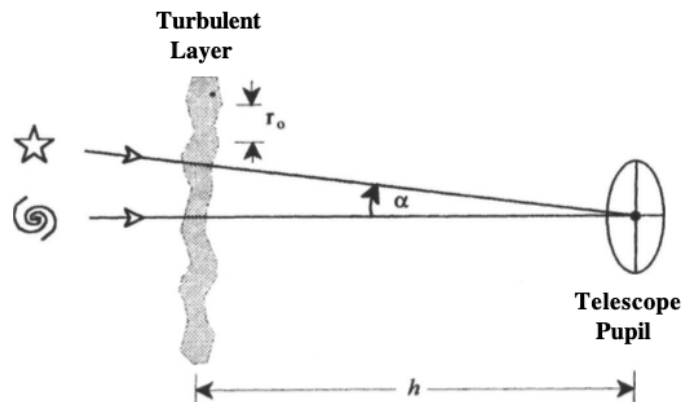
Figure 2.3: Basis of angular anisoplanatism. *From: Hardy (1998)* [1].

The effect of anisoplanacity is specifically pertinent for the METIS due to its single conjugate adaptive optics system and its reliance on existing natural guide stars within its field-of-view. As such, to obtain rigorous and realistic images, it is critical that this field-variability is considered in the simulation process.

---

[3]Approximately equivalent to considering the source guide is at the centre of the field-of-view and the observation target is at its edge, or vice-versa.

A plethora of other effects and technical limitations constrain the effective performance of AO correction. The full description and simulation of an AO system is a highly complex task which largely exceeds the focus of this work. As such, realistic PSFs of the ELT/METIS generated with the `COMPASS` simulation platform [30] were provided by the METIS consortium. The METIS PSF was computed for different positions across the field-of-view defined by a 7×7 regular grid with separation $\Delta\theta = 2''$ centred at the centre of the observed field - cf. figure 2.4. In result, the grid spans over a $12'' \times 12''$ sky region - effectively covering the observed field-of-view ($\approx 11'' \times 11''$). Any PSF defined in this grid is referred to as a *fiducial PSF*.
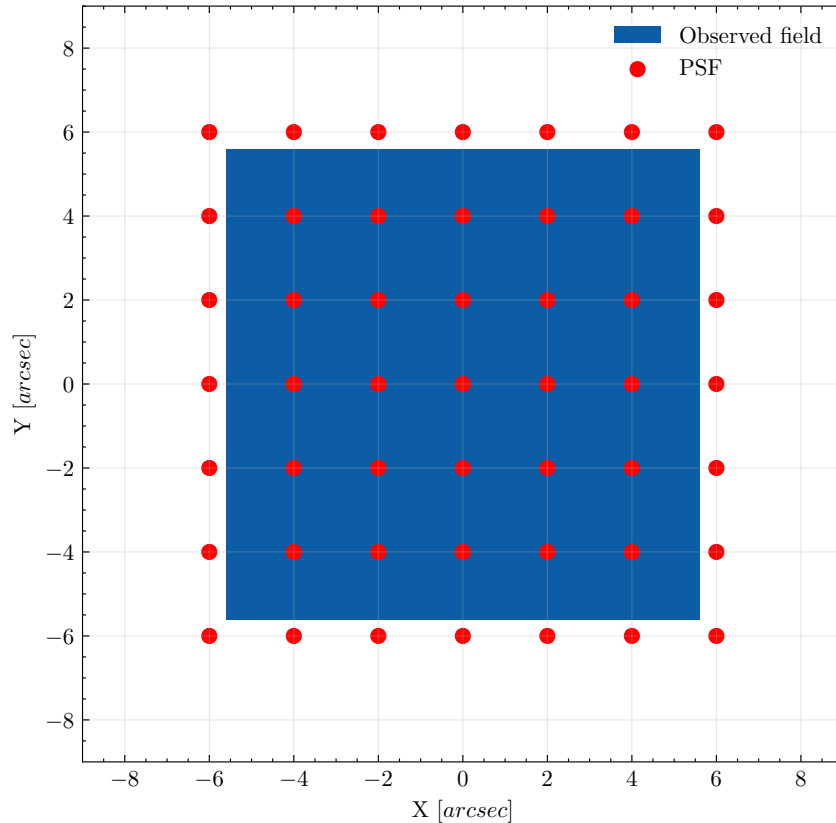
Figure 2.4: Positions of fiducial PSFs across the observed field-of-view.

The PSFs comprising this grid are presented in Fig. 2.5.

Comparing the simulated PSF at the centre of the field with the diffraction-limited case - see Fig. 2.6 - one may observe noticeable differences. Motivated by the effects of the atmosphere and imperfect AO correction, the central core in the simulated PSF suffered a reduction in its peak amplitude - i.e. a decrease in Strehl ratio. As a consequence, the energy of the peak has been spatially distributed, resulting in a higher *noise floor*[4].

Although the METIS instrument achieves near diffraction-limited performance with high SR, it is clear that the effects of the atmosphere and the (partial) AO correction lead to variations in the amplitude and morphology of the PSF. These, in turn, might impact the astrometry and photometry of the images generated by the instrument.

As a quick practical test of this hypothesis, let us determine the centroid of the PSF directly. The centre of mass of a pixel intensity distribution in an image, or variations of it, are often used as an estimation of the centroid of point source objects. This can be obtained by computing

---

[4]In the sense that any contribution additional to the ideal impulse response is noise.
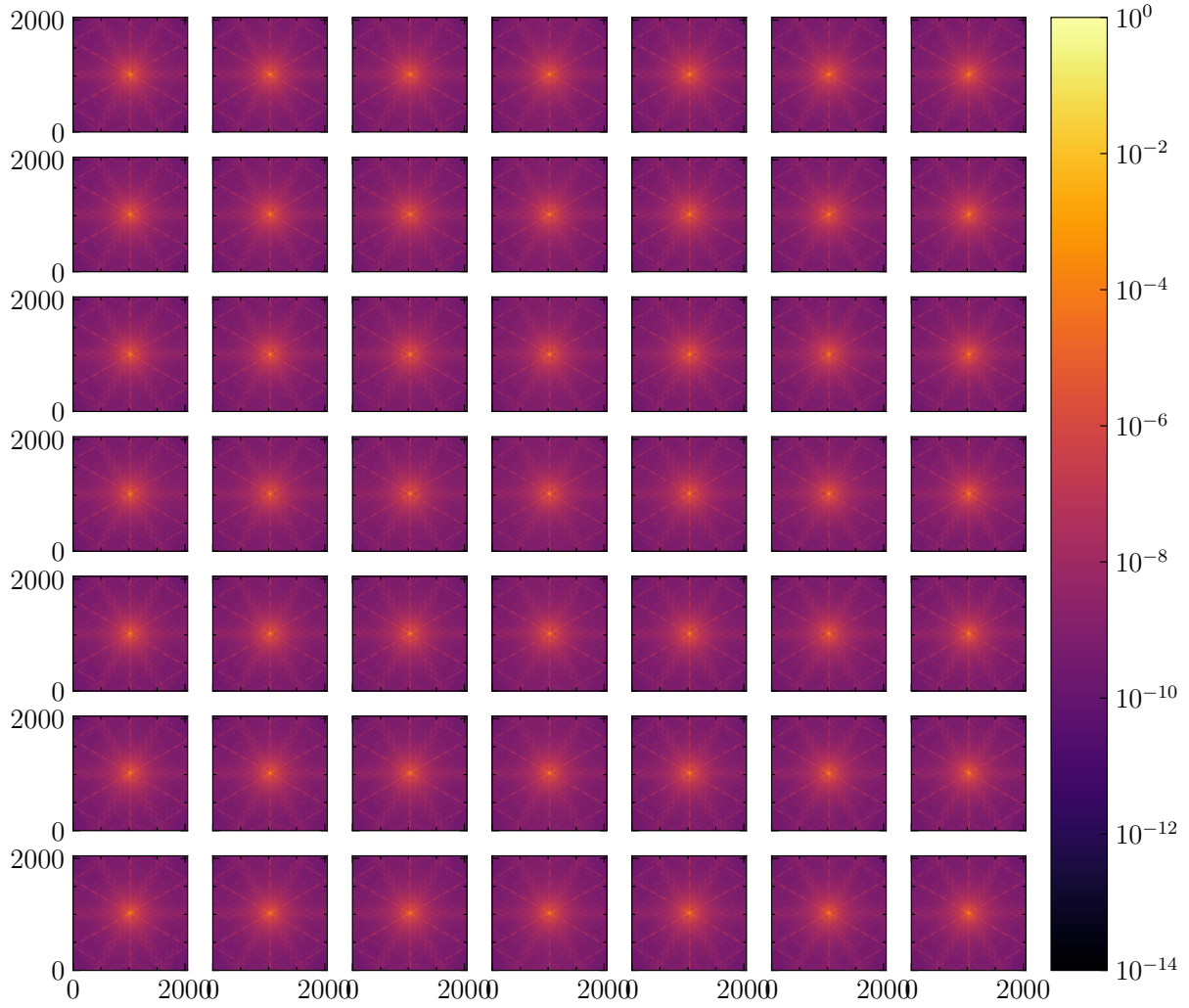
Figure 2.5: Grid of simulated METIS PSFs provided by the `COMPASS` software.

normalised first-order moments of the PSF:

$$\bar{x} = \frac{M_{10}}{M_{00}} = \frac{\sum\limits_{i=1}^{w}\sum\limits_{j=1}^{h} i I(i,j)}{\sum\limits_{i=1}^{w}\sum\limits_{j=1}^{h} I(i,j)} \tag{2.6}$$

and

$$\bar{y} = \frac{M_{01}}{M_{00}} = \frac{\sum\limits_{i=1}^{w}\sum\limits_{j=1}^{h} j I(i,j)}{\sum\limits_{i=1}^{w}\sum\limits_{j=1}^{h} I(i,j)} \tag{2.7}$$

with $\bar{x}$ the $\bar{y}$ the estimated centroid coordinates, w and h the width and the height of the image, respectively, and M_{kl} the kl-th order image moment defined by:

$$M_{kl} = \sum\limits_{i=1}^{w}\sum\limits_{j=1}^{h} i^k j^l I(i,j) \tag{2.8}$$
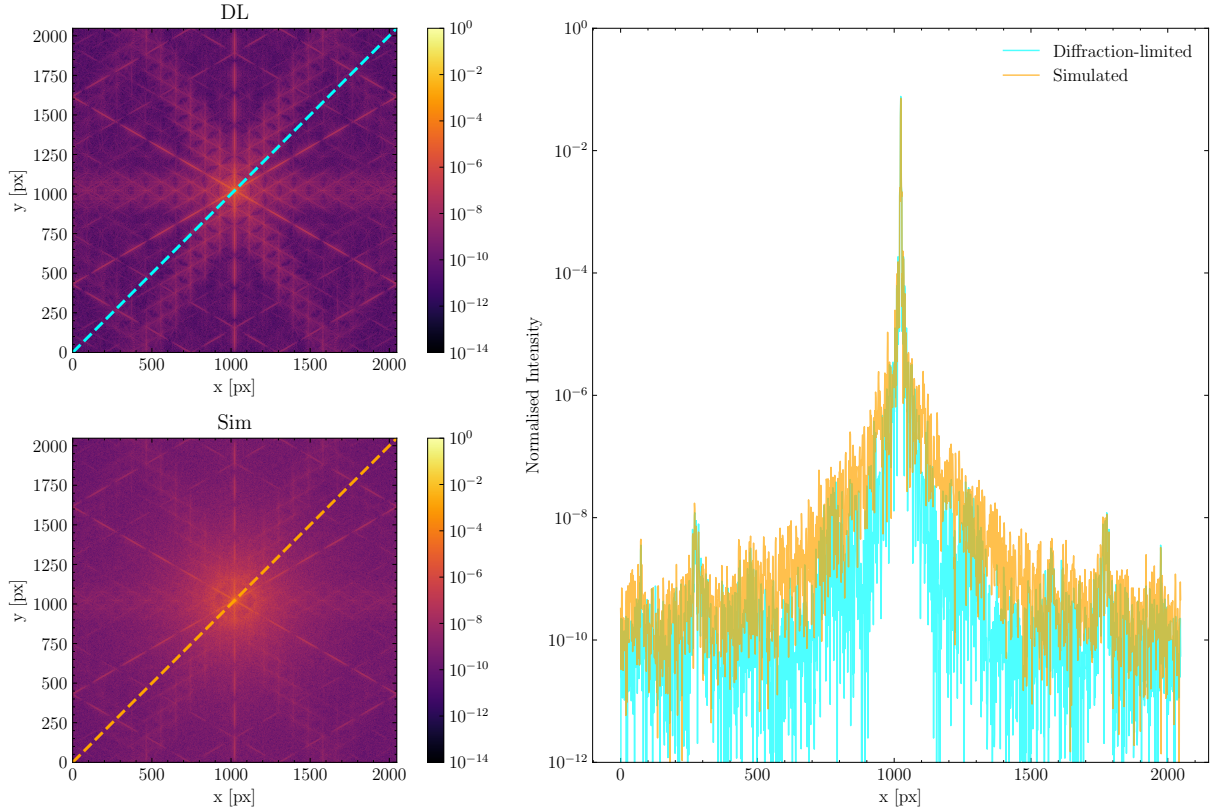
Figure 2.6: Comparison of the pixel intensity values of the diffraction-limited
ELT PSF and the METIS simulated PSF.

From (2.6) and (2.7), the estimated centroid of the ideal diffraction-limited ELT PSF is:

$$\bar{x}_{\mathrm{DL}} - x_0 = -6.03 \times 10^{-4}\,\mathrm{px} = -3.30\,\mu\mathrm{as}$$

$$\bar{y}_{\mathrm{DL}} - y_0 = -6.09 \times 10^{-4}\,\mathrm{px} = -3.33\,\mu\mathrm{as}$$

whilst for the end-to-end PSF at the centre of the field it is:

$$\bar{x}_{\mathrm{E2E}} - x_0 = 1.69 \times 10^{-1}\,\mathrm{px} = 9.26 \times 10^2\,\mu\mathrm{as}$$

$$\bar{y}_{\mathrm{E2E}} - y_0 = 7.35 \times 10^{-2}\,\mathrm{px} = 4.02 \times 10^2\,\mu\mathrm{as}$$

where (x_0, y_0) are the centre coordinates of the PSF frame. With this, it is concluded that even the most basic astrometric estimation can be highly impacted by the effects of atmospheric turbulence and its correction by the AO system.

Concluding, in the case of the METIS instrument, AO allows to seemingly overcome the angular resolution limitation originating from atmospheric turbulence. However, AO correction is only partial, leading to variations in the morphology of the PSF and degradation of the SR - see Fig. 2.6. These effects have direct implications on any astrometric estimation, impacting e.g. the centroid estimation of a point source.

This further motivates the necessity of 1) rigorously defining the system's PSF in order to ensure the realism of the simulated images and 2) achieving a correct depiction of the PSF to enable the study of high-precision astrometry - a requirement well identified in the literature - see e.g. [31, 9]

2.1.1 Handling field-variable point-spread functions

By default, the pipeline provided by the `ScopeSim`/`irdb` packages assumes a field-constant PSF, which is then convolved with the point-source frame. However, the expected system PSF showcases significant variations across the imaged field. This variability must be reflected in the simulated images for a realistic reproduction of the system performance.

To overcome this challenge, one might opt to utilise the `FieldVaryingPSF` class[5] provided by `ScopeSim`. This implementation allows for providing multiple PSFs along with a look-up map for defining which PSF should be used for each image region. However, this leads to sharp discontinuities of the PSF used at the edges of the regions. This effect may be minimised by providing a large number of PSFs (effectively increasing the sampling of the PSF grid across the field) or, ultimately, by providing a PSF for each pixel position of the image frame. This procedure, however, results in a considerably large (and effectively unfeasible) number of PSF simulations.

In this work, this limitation is effectively overcome by considering an alternative approach in which the effective PSF (ePSF) at each pixel position is computed by bi-linear interpolation of the provided PSF grid[6].

This functionality is not available in the core package, having been implemented for this specific task. A description of this approach is presented below, and some tests of its implementation is provided in Appendix A.

Method description

Consider a pixel with a centre position corresponding to sky coordinates (x, y). Since the PSF grid covers the observed field, any pixel in the detector frame will be bounded by four fiducial PSFs: $\mathbf{PSF}(x_1, y_1, i, j)$, $\mathbf{PSF}(x_2, y_1, i, j)$, $\mathbf{PSF}(x_1, y_2, i, j)$, and $\mathbf{PSF}(x_2, y_2, i, j)$, where $\mathbf{PSF}$ is the function that maps coordinates $(x, y) \in G$ in the set of grid positions, G, to a PSF array - $\mathrm{PSF}_{x,y}(i, j)$ - defined at that position in the field, and (i, j) the respective pixel raster coordinates. The effective PSF, $\mathbf{ePSF}$, is, in turn, the mapping of continuous coordinates (x, y) to the PSF array defined at that position in the field.

Assuming linearity, the $\mathbf{ePSF}$ at some point (x, y_1) is obtained by the weighted mean (linear interpolation) of the $\mathbf{PSF}$s for $y = y_1$:

$$\mathbf{ePSF}(x, y_1, i, j) = \frac{x_2 - x}{x_2 - x_1}\mathbf{PSF}(x_1, y_1, i, j) - \frac{x_1 - x}{x_2 - x_1}\mathbf{PSF}(x_2, y_1, i, j) \qquad (2.9)$$

Similarly, one can obtain the effective $\mathbf{ePSF}$ for some point x along $y = y_2$:

$$\mathbf{ePSF}(x, y_2, i, j) = \frac{x_2 - x}{x_2 - x_1}\mathbf{PSF}(x_1, y_2, i, j) - \frac{x_1 - x}{x_2 - x_1}\mathbf{PSF}(x_2, y_2, i, j) \qquad (2.10)$$

Finally, the ePSF at any position (x, y) is the the result of the weighted mean along the x axis of the $\mathbf{ePSF}$ functions defined at $y = y_1$ and $y = y_2$:

$$\mathbf{ePSF}(x, y, i, j) = \frac{y_2 - y}{y_2 - y_1}\mathbf{ePSF}(x, y_1, i, j) - \frac{y_1 - y}{y_2 - y_1}\mathbf{ePSF}(x, y_2, i, j) \qquad (2.11)$$

---

[5]See: https://github.com/AstarVienna/ScopeSim/blob/9baaebf0cfc7824c1bd487e456e30ab7990c81aa/scopesim/effects/psfs.py#L701.

[6]For other cases where linear interpolation was used to model PSF variability see e.g. [31, 32].

Substituting Eq. (2.9) and (2.10) in Eq. (2.11) leads to:

$$
\begin{aligned}
\mathbf{ePSF}(x, y, i, j) = {} & \frac{y_2 - y}{y_2 - y_1} \frac{x_2 - x}{x_2 - x_1} \mathbf{PSF}(x_1, y_1, i, j) \\[2mm]
& - \frac{y_2 - y}{y_2 - y_1} \frac{x_1 - x}{x_2 - x_1} \mathbf{PSF}(x_2, y_1, i, j) \\[2mm]
& + \frac{y_1 - y}{y_2 - y_1} \frac{x_2 - x}{x_2 - x_1} \mathbf{PSF}(x_1, y_2, i, j) \\[2mm]
& - \frac{y_1 - y}{y_2 - y_1} \frac{x_1 - x}{x_2 - x_1} \mathbf{PSF}(x_2, y_2, i, j)
\end{aligned}
\tag{2.12}
$$

which more intuitively demonstrates that bi-linear interpolation is effectively the weighted mean of the four closest fiducial PSFs.

As specified, the effective PSF, $\mathbf{ePSF}$, is computed at each pixel position of the detector frame using this approach, thus achieving a pseudo-continuous variation of the PSF across the field.

2.1.2   Point-spread function resampling

The PSF arrays presented in the previous sections have a distinct pixel scale ($d_{\mathrm{pix}} = 6.88\,\mathrm{mas}$) to that of the detector ($d_{\mathrm{pix}} = 5.47\,\mathrm{mas}$). As such, a resampling - i.e. rescaling of the pixel size - of each PSF is required before the discrete convolution with the object irradiance distribution function (also an array) can be computed.

The resampling is achieved with the bi-cubic interpolation method, considering the pixel sky coordinates of the PSF and of the detector derived from the respective world coordinate system (WCS) data. For this purpose, the `interpolate.interpn` function provided by the `scipy` package [33] is used.

Some tests of this method in the context of this work is presented in Appendix B.

2.2   Point-source definition

This chapter is focused on the methodology of simulating images from a catalogue of point sources. These can be idealised as a point emitter of photons, described by a scaled Dirac delta function. This description, however, breaks down in the computational realm, where one is constrained by the usage of discrete data structures. As such, it is of the utmost importance that the definition of said sources is correct and does not incur in any appreciable artificial errors in its astrometric and photometric analysis derived from its computational representation.

In this section, we tackle this problem and assert the astrometric and photometric correctness of the definition of point sources in the point source frame of the simulation pipeline.

2.2.1   Point source flux

Definition of point source flux in `ScopeSim`

We start by analysing the flux of a single point source object, derived from its magnitude and source spectrum - in this case, the Vega spectrum.

For this purpose, the default `ScopeSim/irdb` configuration for the METIS instrument in LM-band imaging mode is considered. Following, the majority of the effects and elements of the system are disabled, leading to a system comprised of an ideal detector (i.e. no noise,

perfect linearity, infinite full-well capacity, unity quantum efficiency), and a perfect optical system (i.e. perfect reflectance for reflective elements, perfect transmittance for transmissive elements, without thermal emission), with the L' filter left active. Additionally, the convolution with the system PSF is still performed, with caution to guarantee that the sum of the discrete PSF array is equal to unity and its dimension smaller than the detector frame.

With these means, an observation of a test point source with Vega magnitude $m_V = 0$ is defined at the centre of the field[7] is simulated, leading to a total count sum in the resulting frame of:

$$\sum_{i=1}^{w_{\text{img}}} \sum_{j=1}^{h_{\text{img}}} I_{\text{det}}^*(i,j) = 5.498 \times 10^{11} \text{ counts/s}$$

where I_{det} is the pixel intensity in the detector - here considering no noise, and unitary quantum efficiency and photo-electron conversion gain.

Comparison with numerical estimations using `synphot`

As a means of comparison, let us henceforth compute an estimation of the photon flux of a point source object based solely on the Vega source spectrum and the filter considered. The expected photon flux is given by:

$$F_0 = \int_0^\infty d\lambda \; V_g(\lambda) T(\lambda) \tag{2.13}$$

where V_g is the Vega spectral photon distribution, and T is the dimensionless filter transmission curve.

The `synphot` package[8] [34] allows for easy computation of such estimation, out-of-the-box providing the Vega source spectrum, helper classes for defining and applying filters to spectra, and numerical methods for integrating the resulting spectra across the desired wavelength interval. The following estimation relies exclusively on the methods provided by this package.

The Vega source spectrum provided by the `synphot` package - Fig. 2.7a - is scaled by the L' band optical filter included in the `ScopeSim`/`irdb` definition of the METIS LM-imager - Fig. 2.7b.

The resulting spectrum is integrated from $\lambda_{\text{min}} = 3.3\,\mu\text{m}$ to $\lambda_{\text{max}} = 4.3\,\mu\text{m}$ - thus wholly enveloping the bandpass region of the filter considered - using a step of $\Delta\lambda = 1\,\text{nm}$. This leads to the zero-point flux in photons per unit of time per unit of area for the considered spectrum and filter:

$$f_0 = 5.638 \times 10^8 \, \text{ph/s/m}^2$$

---

[7]That is, coincident with the centre position of the central pixel of the simulated frame. This is not a requirement for the simulation, but it allows for determining the maximum pixel intensity of a point source object. This result will become useful for determining the signal-to-noise ratio and optimising the detector integration time of observations.

[8]`synphot` is a widely used Python package geared towards the simulation and handling of photometric data and spectra. It has been developed by the Space Telescope Science Institute (STScI) development team, and it is part of Astropy's affiliated package list.

(a) Vega spectrum
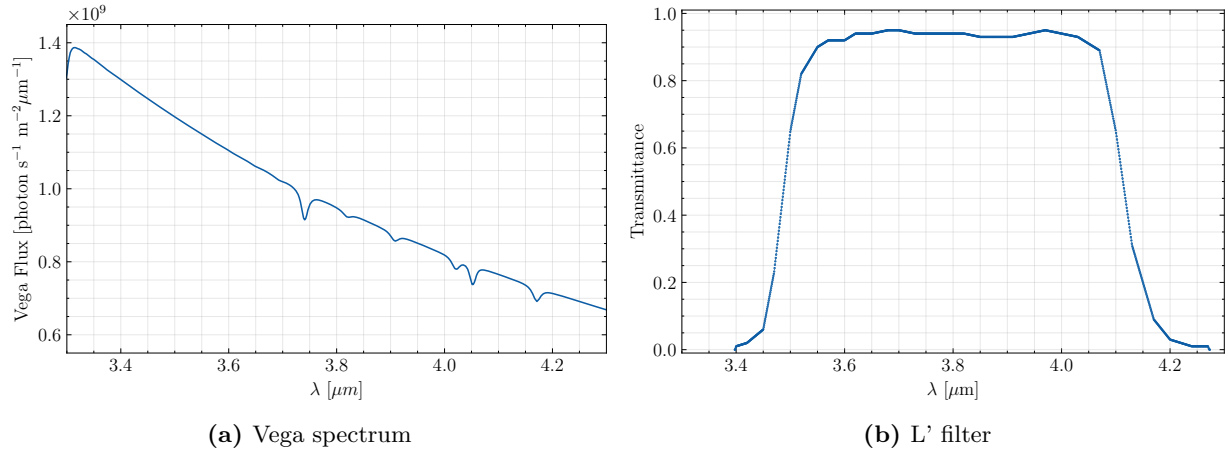
(b) L' filter

Figure 2.7: Vega spectrum flux (left) and L' photometric bandpass filter relative transmittance (right).

Approximating the telescope pupil to a circular mirror of effective diameter[9] $D = 36.9\,\text{m}$, with a circular central obstruction of diameter[10] $d = 10.95\,\text{m}$, we obtain an effective pupil area, A_{pupil}:

$$A_{\text{pupil}} = \frac{\pi}{4}\left(D^2 - d^2\right) \approx 9.752 \times 10^3\,\text{m}^2$$

which leads to a total zero-point flux for the instrument:

$$F_0 = f_0 A_{\text{pupil}} = 5.498 \times 10^{11}\,\text{ph/s}$$

which is in agreement with the result obtained previously from the simulation, considering a detector conversion gain of $G = 1\,\text{ph/e}^-$. Thus, the resulting flux for any given magnitude $m_{\text{L}'}$ is:

$$F(m_{\text{L}'}) = F_0\,10^{-0.4\,m_{\text{L}'}} \tag{2.14}$$

In conclusion, we confirm that the definition of the flux of a point source in the simulation pipeline provides a detector flux which is identical to that obtained by considering only the Vega spectrum and the filter used.

2.2.2   Point source positioning

The correct spatial description of a point source on a finite, discrete reference frame is crucial for recovering its real position in the sky. In particular, we are interested in defining the approach to project point sources, as described by a set of sky coordinates and a flux, onto a discrete frame to which it can subsequently be applied the convolution with the system PSF. In this section, the method used to achieve this is described.

---

[9]This is the value considered in the `ScopeSim` ELT configuration. This seemingly deviates from the often mentioned 39 m scale for the primary mirror but should be assumed as an effective approximation that better estimates the area of the pupil assuming a circular shape, which is not the case due to the segmented nature of this mirror. This approach is also used here to allow for direct comparison of the estimations derived from `ScopeSim`.

[10]Again, due to the shape of the pupil mirror's segments, the central obstruction is not circular and this is an effective approximation of its diameter.

Method description

In the proposed approach, the point source flux is constricted in an area corresponding to a single pixel[11], but this area not necessarily coinciding with a pixel in the detector frame - i.e. it may assume any continuous position. Thus, the resulting flux may be spread[12] across a detector area of $2 \times 2\mathrm{px}^2$, with the fraction of flux in each detector pixel corresponding to its overlap with the idealised point source pixel.

Let us assume four adjacent pixels in the detector frame - P_{11}, P_{21}, P_{12}, and P_{22}, assuming positions $P_{ij} \to (x_i, y_j)$ - bounding an idealised point source pixel P_s centred at position (x, y). The intensity of this idealised source pixel weighted by its overlap with the detector frame results in the intensity of these pixels corresponding to:

$$P_{11} = (x_2 - x)(y_2 - y)P_s$$

$$P_{21} = (x - x_1)(y_2 - y)P_s$$

$$P_{12} = (x_2 - x)(y - y_1)P_s$$ (2.15)

$$P_{22} = (x - x_1)(y - y_1)P_s$$

An intuitive interpretation of this approach is provided in Appendix C.

Testing the positioning method

A finite support array of size 2048×2048 pixels is considered, and a point source is defined in the frame following the procedure described previously. Then, the resulting array is convolved with a simple, illustrative system PSF - namely, the diffraction-limited ELT PSF presented in figure **??**. Finally, the centroid of the point source is computed using the `fwcentroid` routine provided by the `poppy` package [35]. This process is repeated for different point source positions, namely in the range $y = 0 \wedge x \in [0.0, 1.0)$ px and $x = 0 \wedge y \in [0.0, 1.0)$ px with step 0.05 px, where (x, y) are the sky coordinates projected in the detector frame and $(x, y) = (0, 0)$ corresponding to the centre position of the central pixel in the frame. The resulting error of the estimated centroid position for both cases is presented in Fig. 2.8.

We conclude that, for the case considered, the extraction of the centroid of a point source object in a noise-free frame can be achieved with an error less than 0.05%, corresponding to $\sim 1\,\mu\mathrm{as}$, on each axis. As such, the degeneracy in the positioning of point source objects with sub-pixel precision mentioned previously is lifted. Consequently, this method is used for the image generation pipeline.

---

[11]In the point source reference frame - that is, before convolution with the system PSF - thus, the system's diffraction is not yet considered. This corresponds simply to the digitised spatial irradiance distribution function of the point sources considering the detector's sampling.

[12]Once again, here it is only described the effect of positional sampling in an idealised system (i.e. $D \to \infty$). It is only after the convolution with the system's PSF that any point source flux will be dispersed over a larger area - in theory, infinitely large; in practice, of the size of the computational PSF array.
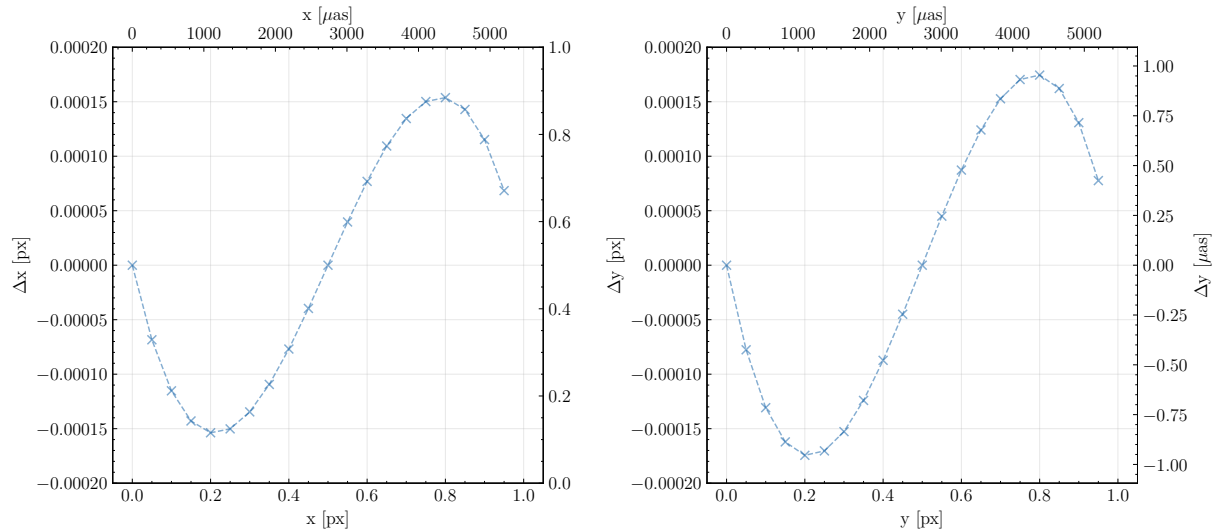
Figure 2.8: Estimated x (left) and y (right) centroid coordinates of points sources at pixel positions $y = 0$ with variable x (left) and $x = 0$ with variable y (right)

2.3   Modelling the optical system

The optical design of any state-of-the-art scientific telescope - and, specifically, that of the ELT/METIS instrument - is a complex task, usually relying on extensive modelling and simulation efforts [36, 37, 38, 39]. Additionally, due to shortcomings [40, 41] such as limitations in the fabrication of the optical elements, transient variations in their properties (e.g. thermal expansion), and difficulties in its characterisation - more so for an instrument not yet built - the effective optical performance of the real system might deviate from the theoretical and simulated predictions. These effects are partially introduced in the image formation pipeline by means of the end-to-end simulated PSF, without their concrete parametrisation being the purpose of this section.

In this section, we turn our focus to the transmittance, reflectance, and emissivity of each optical element[13]. These are generally well-parameterised properties for most materials and optical elements assumed and incur, arguably, the most significant photometric impact on the imaged target.

The purpose of this section is two-fold: firstly, give an overview of the composition of the optical train of the L' imager down to every single optical element, and secondly, provide estimations for the optical throughput and thermal emission of each optical segment.

Estimating the thermal emission of an optical element

To estimate the thermal emission of the optical elements or assemblies thereof, we rely on a practical simulation approach similar to that described in section 2.2.1. Here, we rely on an idealised system comprised of said element or assembly, the *L'* filter, the normalised PSF response, and an ideal detector. More so, the optical elements are considered to have homogeneous temperatures and to be in thermal equilibrium with the environment unless otherwise stated. Additionally, no photon noise is considered. An empty field - i.e. with no point-source objects - is simulated,

---

[13]Here, we assume the atmosphere as any other optical element of the system, with well-defined transmittance, reflectance, and emissivity values.

with the resulting pixel intensity assumed to be the thermal emission of the segment per pixel per unit time.

Estimating the optical throughput of an optical segment

Similarly, the estimation of the optical throughput of one optical segment or medium is accomplished by simulating an observation of a test point source assuming an ideal system - i.e. in the presence of only said segment, the optical L' filter, the normalised PSF response, and an ideal detector. The relative throughput for each element or medium is estimated by[14]:

$$\eta_i = \frac{\sum_{i=1}^{n_{\text{pix}}} \left[I_{\text{det}}(i) - I_{\text{bg}}(i) \right]}{F_{\text{ELT}}} \tag{2.16}$$

where I_{det} is the total detector counts, I_{bg} is the reading resulting from the background thermal emission, and F_{ELT} is the point-source object flux as provided by (2.14).

2.3.1 The atmosphere

The `ScopeSim` package relies on the sky models developed by S. Noll et al. (2012) [42] and A. Jones et al. (2013) [43] to attain the sky transmission curves and radiance spectra at the Cerro Armazones cite. This is made easily available through the `SkyCalc` application[15] and its associated command-line interface (CLI). The modelling of atmospheric extinction includes molecular and aerosol absorption, Rayleigh scattering by air molecules [44], and Mie scattering by aerosols [45]. The radiance model takes into consideration various effects [42], e.g. scattered moonlight and scattered starlight, zodiacal light, and molecular emission. Of these, molecular emission of the lower atmosphere dominates for the L band [42].

For the most part, the default configuration is used, with only the observatory/altitude ($h = 3060\,\text{m}$) and the airmass ($X = 1.20$) parameters modified by the `irdb` default configuration.

With the procedure specified previously, the atmosphere background emission is estimated from a `ScopeSim` simulation considering only this effect. The resulting background emission of the atmosphere, I_{atm}, is:

$$I_{\text{atm}} = 1.243\,96 \times 10^5 \,\text{photo}\,e^-/\text{s/px}$$

Additionally, the transmissivity of the atmosphere was estimated to be:

$$\eta_{\text{atm}} \approx 91.26\,\%$$

To motivate the credibility of these results, the atmospheric spectrum for the Armazones site was retrieved manually from the `SkyCalc` web service and these properties were calculated with the `synphot` package. This resulted in an agreement within $0.5\,\%$ of the results provided by `ScopeSim`.

2.3.2 The ELT/METIS optical train

The optical train comprised of the ELT telescope and the METIS instrument in L/M band imaging mode can be divided into three main optical segments:

---

[14]One should note that this does not represent the actual relative throughput of the respective elements. This is equivalent, in fact, to the integration of the spectral throughput of the element scaled by that of the selected filter for the filter's wavelength interval.

[15]See: https://www.eso.org/observing/etc/skycalc.

- **ELT common optics**: These are the common optical elements - including the pupil and main deformable mirrors - that are shared by every instrument present in the ELT;

- **METIS common fore optics (CFO)**: These are the common optical elements shared by every subsection of the METIS instrument;

- **METIS L/M band imager camera**: This is the optical segment exclusive to the operation of the L/M band imaging mode.

Let us now analyse each of these segments individually.

ELT common optics

The ELT encompasses a five-mirror optical design [36] which components are henceforth referred to as M1 (pupil mirror) through M5:

- **M1**: The primary (pupil) segmented mirror ($D_{\text{tel}} \approx 39\,\text{m}$);

- **M2** and **M3**: The secondary ($D_{\text{M2}} \approx 4.2\,\text{m}$) and tertiary ($D_{\text{M3}} \approx 4.0\,\text{m}$) mirrors which, along with M1, form the primary three-mirror anastigmat (TMA);

- **M4**: The main deformable mirror ($D_{\text{M4}} \approx 2.4\,\text{m}$) used for AO correction;

- **M5**: A tip-tilt mirror used for AO correction, field stabilisation, folding to and switching between Nasmyth focus points, amongst other functionality.
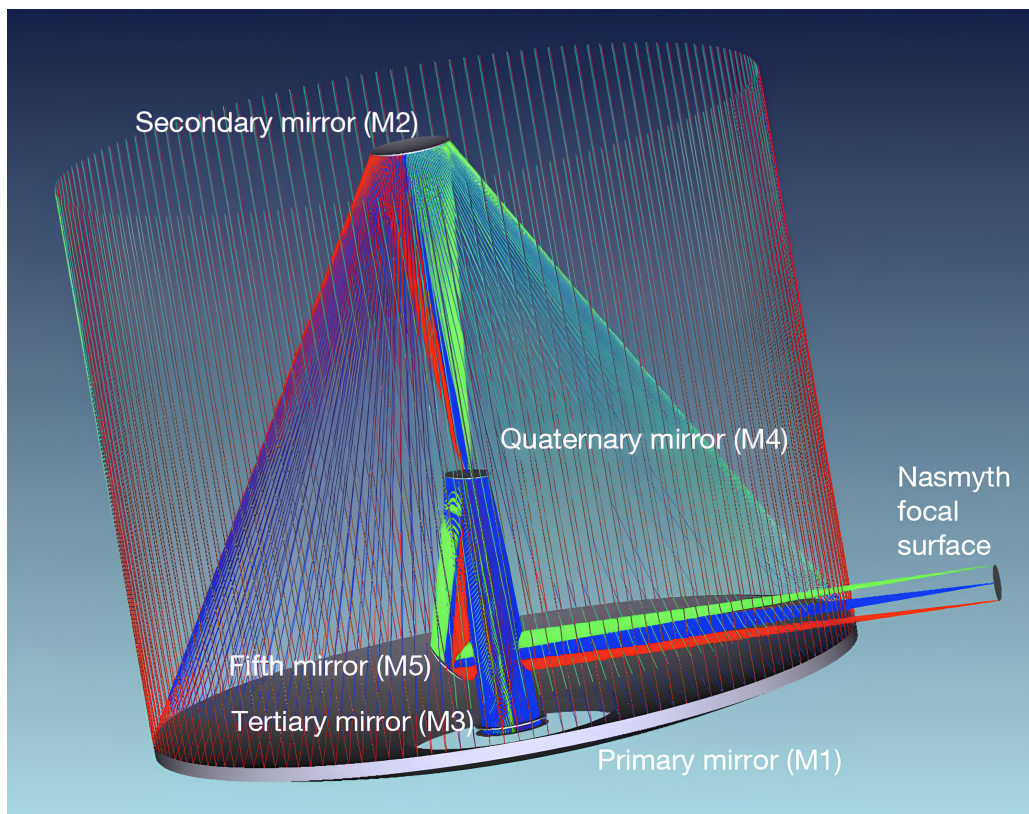
Figure 2.9: ELT M1-M5 optical design. *From: The E-ELT Construction Proposal* [2].

The reflectance and emissivity curves presented in Fig. 2.10 entail the contributions of mirrors M1 through M5.

(a) Mirror emissivity

(b) Mirror reflectance
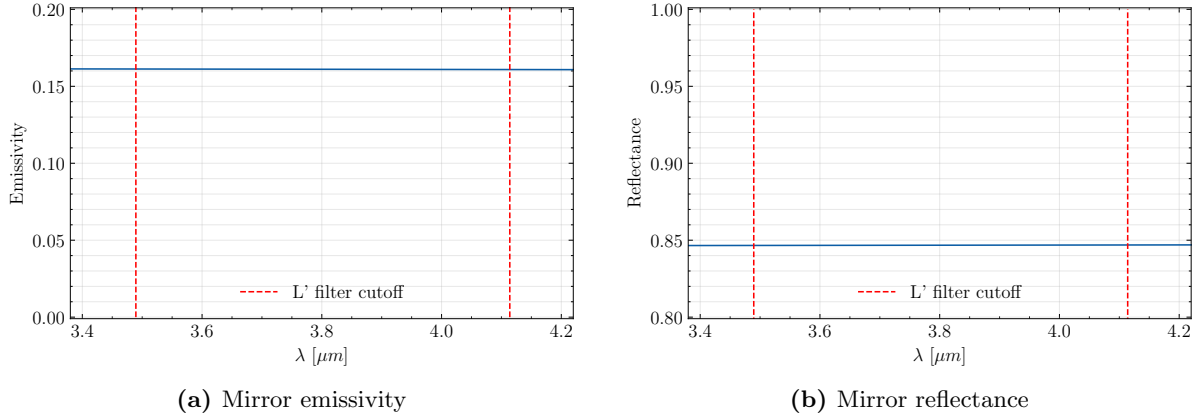
Figure 2.10: Optical properties of the ELT M1-M5 mirrors in the L' band used in the `ScopeSim` simulation

As described previously, the thermal emission of these elements is retrieved from the simulation of an idealised system considering no point-source objects. The resulting pixel intensity, I_{M1-M5}, for the background emission of the M1-M5 mirrors is:

$$I_{M1-M5} = 3.787\,46 \times 10^5 \,\text{photo}\,e^-/\text{s}/\text{px}$$

For attesting this result, a simple estimation of the thermal black-body emission of the primary ELT mirror (M1) can be easily obtained using the *synphot* package. Following the procedure in section 2.2.1, we start by considering a source spectral photon distribution - in this case, the black-body spectrum - and apply the *L'* bandpass filter throughput. The resulting flux incident on a single pixel is then provided by integrating over the wavelength for the surface area of the pupil mirror emitting over a solid angle covering the pixel area:

$$F_{M1} = \int_{\text{pixel}} d\Omega \int_{\text{pupil}} dA \int_0^{+\infty} d\lambda \; \epsilon(\lambda) B_\lambda(\lambda) T(\lambda) \tag{2.17}$$

with B_λ the spectral photon flux density for a black body, T the filter throughput, and ϵ the emissivity, assuming a homogeneous temperature.

For the L' band, the emissivity is considered practically constant, with $\epsilon \approx 0.16$. Integrating equation (2.17) considering $A_{\text{pupil}} = 9.752 \times 10^3 \,\text{m}^2$ and $\Omega = 5.47 \times 5.47 \text{mas}^2$, we obtain:

$$F_{M1} = 3.034\,32 \times 10^5 \,\text{photo}\,e^-/\text{s}/\text{px}$$

A discrepancy of $\sim 20\,\%$ in the estimated value and the simulations is encountered. One contributing factor results from the fact that in the simulation, the complete M1 through M5 optical train is considered, in opposition to our brief estimation for which we only consider the primary mirror M1. This contributes to a larger effective surface area in the simulation respective of the M2 through M5 mirrors - albeit their markedly smaller dimension. Nevertheless, before attempting to identify the source of this deviation, it is of interest to analyse its actual contribution to the veracity of the results.

As we have seen, thermal emission is directly related to the temperature of the optical elements. So far, we have considered a constant, homogenous temperature of $T = 282.15 \,\text{K} = 9\,°\text{C}$. Let us now consider a slightly higher temperature, perchance $T = 287.15 \,\text{K} = 14\,°\text{C}$; the resulting thermal emission of the M1 mirror, estimated with the same approach as before, is

then:

$$F_{\mathrm{M1}}^{T=287.15\,\mathrm{K}} = 3.815\,20 \times 10^5 \text{ photo e}^-/\mathrm{s/px}$$

whilst considering $T = 277.15\,\mathrm{K} = 4\,^\circ\mathrm{C}$ one obtains:

$$F_{\mathrm{M1}}^{T=277.15\,\mathrm{K}} = 2.393\,69 \times 10^5 \text{ photo e}^-/\mathrm{s/px}$$

This result represents a variation of approximately 25% for a mere ambient temperature difference of $\Delta T = 5\,\mathrm{K}$. This emphasises two important remarks: 1) Unless precise analysis of the performance of the instrument concerning the temperature of the warm optical elements is desired, the deviation observed between the simulation and the estimated value for the thermal emission of said components is not significant and may be seen as slight variation in the working temperature of the system; and 2) In operation, the dominating thermal emission of the warm elements is critical for defining the instrument's observation parameters and strategy, such as the detector integration time (DIT). Since it is not the scope of this work to further analyse the thermal stability of the system, henceforth, we will consider the constant temperature of $T = 282.15\,\mathrm{K}$ for the ground-level atmosphere and the warm optical elements assumed so far.

METIS common fore optics
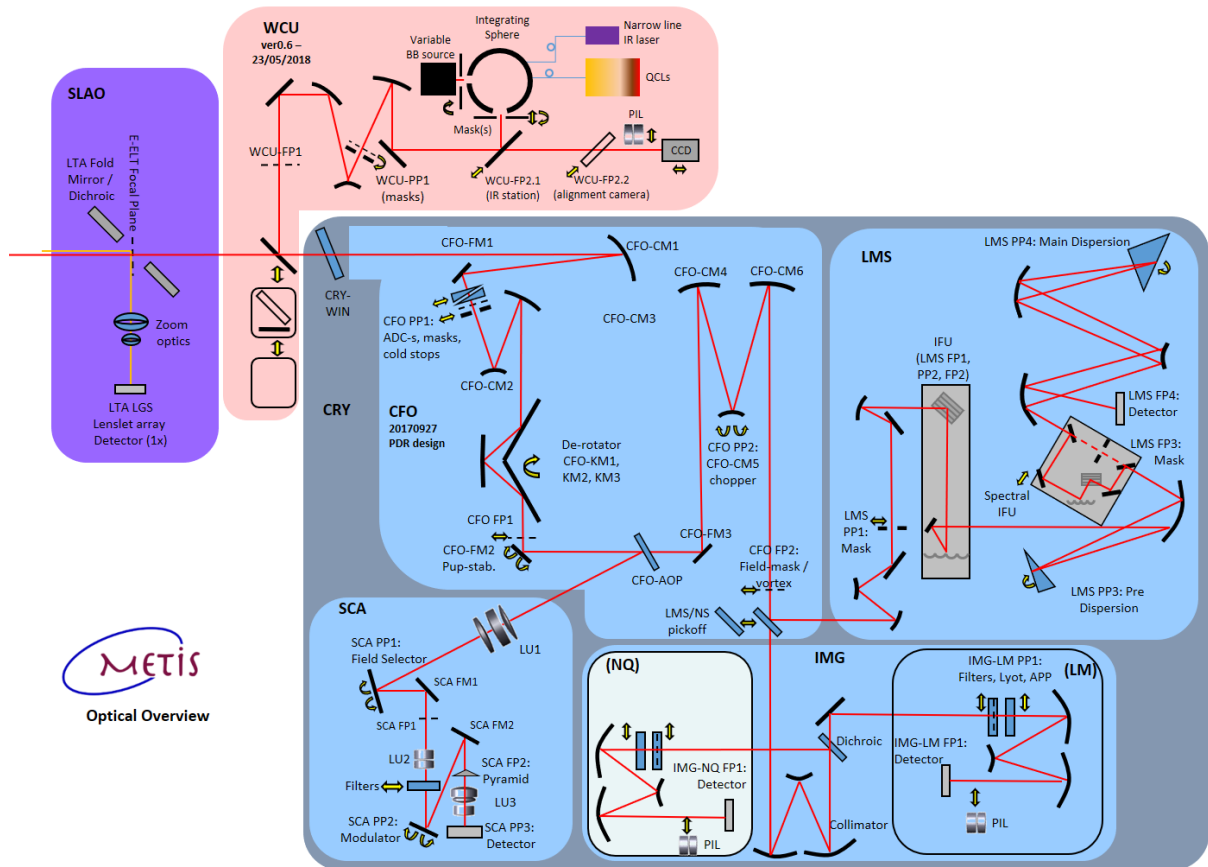
Figure 2.11: Diagram of the optical design of the METIS instrument and respective sub-systems. *From: Brandl et al. (2018) [3].*

The METIS instrument incorporates an optical section common to all optical branches and operation modes - the common fore optics (CFO) - see Fig. 2.11. The first stage of this section,

after the instrument's entry window, CRY-WIN, is a TMA comprised of mirrors CFO-CM1, CFO-CM2, and CFO-CM3, with a folding mirror, CFO-FM1, between the first and the second mirrors. This is followed by a de-rotator composed of mirrors CFO-KM1, CFO-KM2, and CFO-KM3. This is succeeded by a dichroic beam-splitter, CFO-AOP, placed between two folding mirrors, CFO-FM2 and CFO-FM3. Finally, the last stage of the CFO train is composed of a TMA comprised of mirrors CFO-CM4, CFO-CM5, and CFO-CM6. The respective optical properties of these elements are presented in Fig. 2.12.

(a) Mirror reflectance   **(b)** Dichroic beam-splitter transmittance
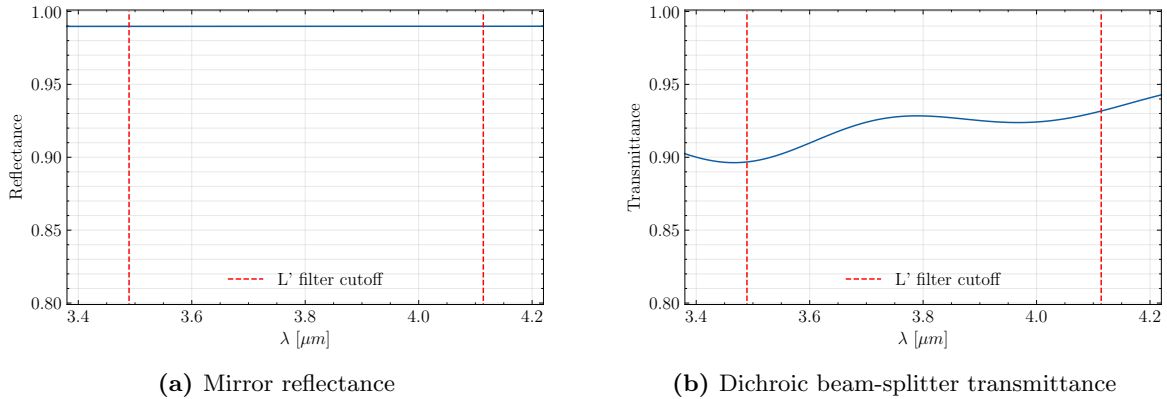
Figure 2.12: Optical properties of the METIS CFO mirrors (left) and dichroic element (right) in the L' band used in the `ScopeSim` simulation

Most of the optical elements comprising this section are contained within a cryostat, thus generally presenting very low thermal emission. This is not the case, however, for the entrance window. This transmissive optical element interfaces the instrument with the Nasmyth mount in which it is located and is consequently in contact with the non-thermally-controlled environment of the telescope's dome. The optical properties of these elements are presented in Fig. 2.13.

(a) Window emissivity   **(b)** Window transmittance
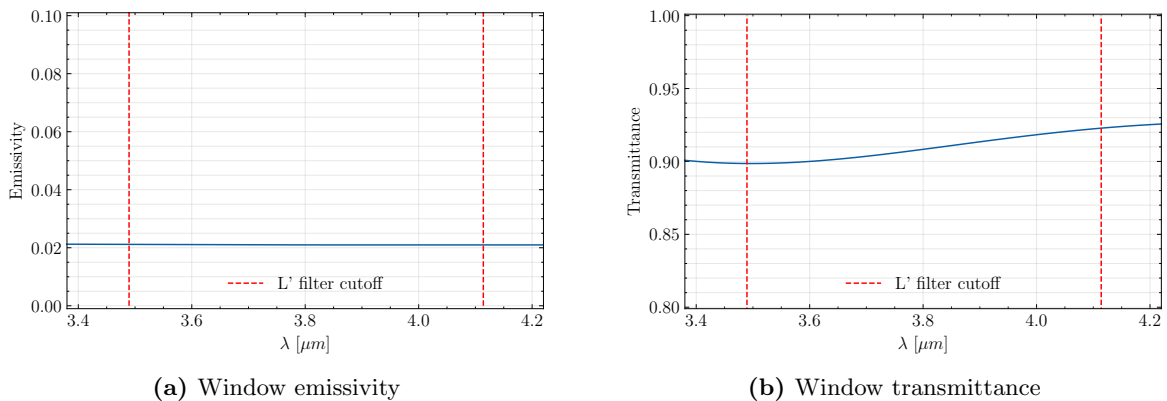
Figure 2.13: Optical properties of the METIS CFO entry window in the L' band used in the `ScopeSim` simulation

To estimate the total flux in the detector originating from this set of optical elements, we repeat the simulation approach described for the M1-M5 mirror, albeit now only considering the CFO and L' filter as the only active elements in the optical train. The resulting pixel intensity due to the thermal emission of the CFO, I_{CFO}, is:

$$I_{\mathrm{CFO}} = 2.8787 \times 10^4 \, \mathrm{photo\, e^-/s/px}$$

LM-band imager optics

The final optical elements in the imager optical branch are the camera optics before the HAWAII-2RG FPA. This segment is comprised of a TMA collimator shared with the N-band imager - mirrors IMG-M1, IMG-M2, and IMG-M3 - a dichroic beam-splitter - IMG-dichroic -, two folding mirrors - IMG-LM-FM1 and IMG-LM-FM2 -, and the camera TMA system - IMG-M1, IMG-M2, IMG-M3.

The mirrors described above are modelled as purely reflective elements with their reflectance a function of the photon wavelength, whilst an emissivity curve is additionally provided for the dichroic beam-splitter - see Fig. 2.14.

(a) Mirror reflectance

(b) Dichroic beam-splitter transmittance
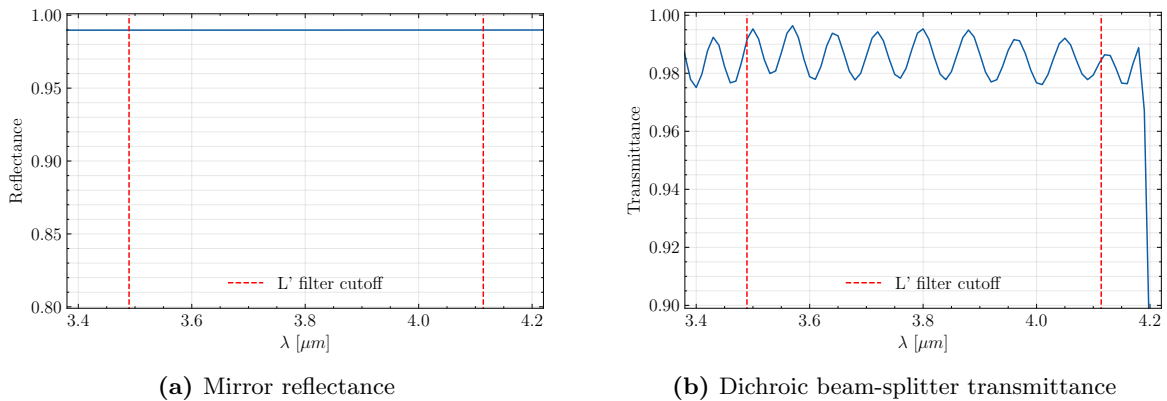
Figure 2.14: Optical properties of the METIS L'/M imager mirrors (left) and dichroic element (right) in the L' band used in the `ScopeSim` simulation

These are located inside the cryostat, with negligible thermal emission expected due to their extremely low temperature and small dimensions. Repeating the procedure presented for the previous optical sections, we obtain a pixel intensity due to thermal emission of the LM-band imager optics, I_{CAM}, equal to:

$$I_{\mathrm{CAM}} = 2.3957 \times 10^{-12}\,\mathrm{photo\,e^-/s/px}$$

2.3.3 Complete system throughput and emission

So far, we have evaluated the thermal emission and throughput (efficiency) of each section of the optical path individually. It is useful now to analyse the system as a whole.

The product of the individual segment throughputs provides the total relative throughput for the optical system and mediums:

$$\eta_{\mathrm{opt}} = \prod_{i=1}^{n_{\mathrm{el}}} \eta_i = 0.4372 \tag{2.18}$$

On the other hand, the resulting system emission is the combination of the emission of each section reduced by the throughput of the respective downstream elements. In a similar way as the in previous sections, we estimate the total system emission by considering a test system comprised of an ideal detector, the *L'* optical filter, and all the optical sections with non-null emission or non-ideal throughput - namely, the atmosphere, the M1-M5 mirrors, and the METIS common fore optics, cold stop, ADC, and L/M band imager camera. The resulting ideal pixel intensity - i.e. disregarding detector effects - for the partial system, including the components described, henceforth referred to as the *background intensity*, is:

$$I_{\mathrm{bg}}(i, j) = 2.966\,12 \times 10^5\,\mathrm{photo\,e^-/s/px}$$

2.4   Modelling the *focal plane array*

The detector - also referred to as an *image sensor* or *focal plane array* (FPA), and used interchangeably henceforth - and its associated readout and processing circuits are the core components that ensure the measurement of the field imaged by the optical train of a telescope. The solution selected for the METIS LM-band imager is based on a single *Teledyne HAWAII-2RG* integrated circuit, using a mercury cadmium telluride (HgCdTe) detector with a resolution of 2048×2048 px^2 and a pixel size of 18×18 µm^2.

Devices geared towards IR imaging based on THIS semiconductor compound still manifest the usual effects and limitations of their Si-based counterparts, e.g. limited quantum efficiency, the presence of dark current, and readout noise originated by the associated acquisition logic. These characteristics and effects are tightly linked to the resulting electronic background noise and the detector's ability to image astronomical sources, thus contributing significantly to the achievable signal-to-noise ratio. As a result, it is critical that these effects are well parameterised and modelled for the specified detector so as to provide accurate reproduction of the expected imaging capabilities of the instrument.

The following sections present a brief description of these effects and their definition in the simulation pipeline.

Quantum efficiency

The detection of the incoming photons by the sensor assumes its absorption and conversion to photo-electrons. The probability of the sensor to perform this absorption for subsequent conversion is referred to as *quantum efficiency*, η_{QE}, and it may be defined by absorbed photon flux, φ_{abs}, and the incident photon flux, φ_{total}:

$$\eta_{\mathrm{QE}} = \frac{\varphi_{abs}}{\varphi_{total}} \tag{2.19}$$

The quantum efficiency for the METIS detector is provided directly as a function of wavelength in figure 2.15.

Shot noise

The detection (i.e. measurement) of photons - *quantised particles* - follows a distribution which is statistical in nature - the shot noise. This phenomenon follows a Poisson distribution; as such, its standard deviation, σ_{shot}, corresponds to:

$$\sigma_{\mathrm{shot}} = \sqrt{N} \tag{2.20}$$

where N is the average photo-electron counts in the detector.

In the simulation pipeline, this effect is contemplated as an additive array to the detector counts following (2.20), where N is assumed the detector counts originating from background and source fluxes and dark current.
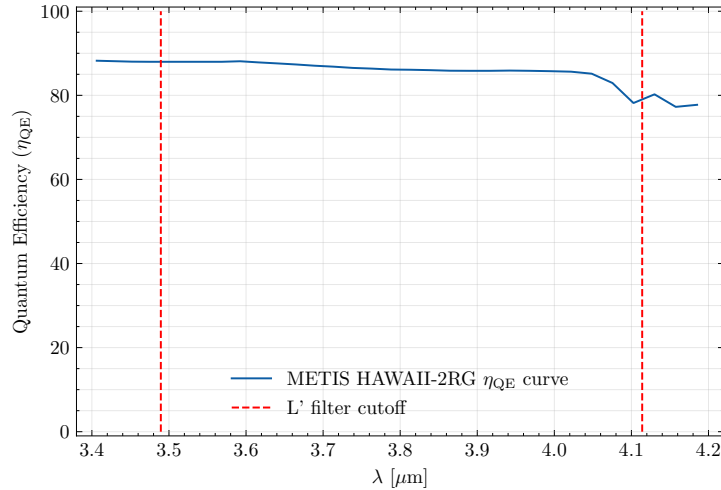
Figure 2.15: Quantum-efficiency curve for the Teledyne HAWAII-2RG midinfrared field plane array

Dark current

It is a known property that semiconductor-based photodetectors present non-null counts even in the absence of incident photons. This is due to the variety of effects that result in a charge current - *dark current* - in the detector, of which the thermionic emission is often dominant [ref].

This effect is modelled in the simulation pipeline by the addition of constant[16] and uniform flux, ϕ_{DC}, to the image frame, such that:

$$\phi_{\mathrm{DC}} = 0.05\,\mathrm{photo\,e^-/s/px}$$

Detector linearity

The linearity of a detector is a measure of proportionality between the incident flux and the resulting signal. Due to effects such as physical phenomena intrinsic to the detector's operation, degradation of its constituents, and manufacturing imperfections, this relation might deviate considerably from ideal.

The linearity curve for the HAWAII-2RG detector is provided in Fig. 2.16a. The linearity error is significant even for a state-of-the-art IR detector, such as the HAWAII-2RG - cf. Figure 2.16b. This effect is most noticeable at both extremes of the detectable incident flux.

This effect is modelled in the simulation pipeline by scaling the absorbed photon flux in the detector by the curve provided in Figure 2.16a.

---

[16]Disregarding shot noise, which has been addressed previously.

(a) Linearity curve

(b) Relative linearity deviation
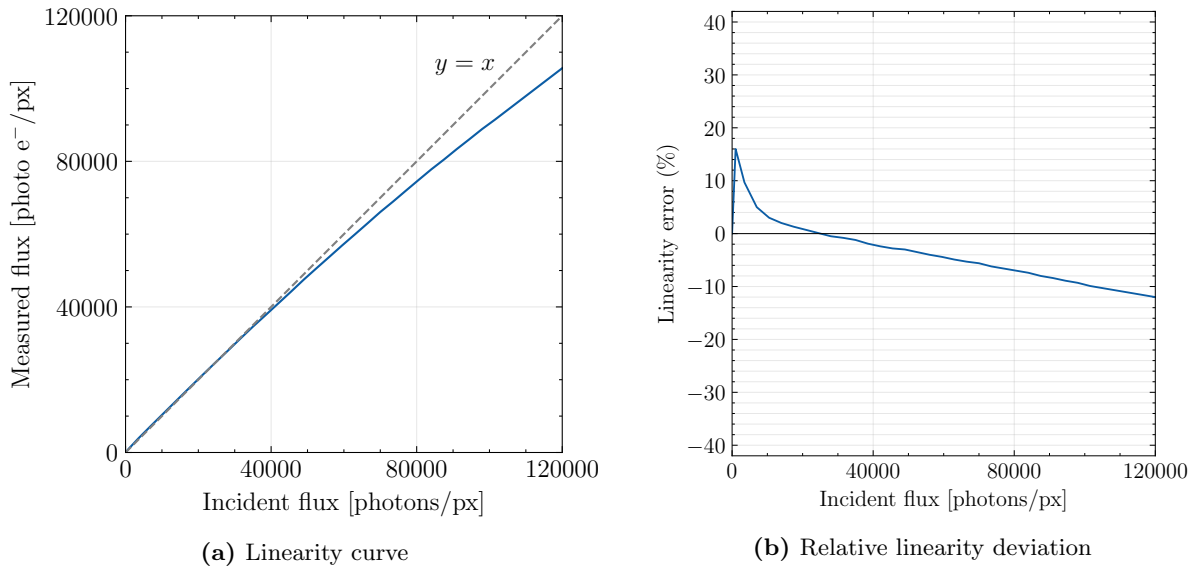
Figure 2.16: Linearity properties of the Teledyne HAWAII-2RG MIR FPA.

Readout noise

Detector readout noise is associated with the analogue-to-digital (A/D) conversion process taking place in the detector readout electronics. This arises from different effects, such as A/D conversion variability across the array and electronic noise in the associated circuits. Due to the complexity of these systems and their multitude of noise sources, a detailed description of this noise manifestation and the determination of its statistical distribution is a complex task which exceeds the scope of this work. Additionally, the detailed description of this effect is often not highly relevant for the purpose of image formation - more so in the photon-limited regime of operation of the detector - and can be assumed to follow a Gaussian distribution in ideal conditions [46, 47].

In the simulation pipeline, the readout noise per detector integration time (DIT) is sampled from a Gaussian distribution[17] with standard deviation σ_{RON}:

$$\sigma_{\mathrm{RON}} = 70 \, \mathrm{ph} \ \mathrm{e}^-/\mathrm{px}$$

2.5 Photometric considerations

2.5.1 Source and background photo-electron counts

So far, we have only been concerned with the integrated flux originating from a point source object - see Sec. 2.2.1. However, it is useful to define the maximum pixel intensity resulting from said source. This estimation relies on the specific PSF used since it represents, by definition, the impulse response of the system. Assuming an ideal case, we consider the normalised diffraction-limited PSF with its core (i.e. maximum value) pixel-centred. As a result, the maximum value

---

[17]The readout noise statistical distribution is usually assumed to be centred at some bias value. In the simulation, however, no bias is considered. Although this might seem unrealistic - since the readout noise can assume negative values - it leads to seemingly the same result after the image reduction procedure - assuming this procedure can correctly subtract the bias value. Thus, the detector readout noise is emulated in the generation pipeline by this distribution with a null mean value for simplicity.

of the diffraction limit PSF matrix, PSF_{DL}:

$$\eta_{\text{PSF}}^{1 \times 1} = \max \text{PSF}_{\text{DL}}(i, j) = 0.0476 \tag{2.21}$$

defines the scaling factor, $\eta_{\text{PSF}}^{1 \times 1}$, that allows to quickly convert between the point-source flux F - see Eq. (2.14) - and the resulting maximum pixel intensity in the detector, $I_{\text{det}}^{1 \times 1}$, for the diffraction-limited case. As said, the diffraction-limited PSF is an ideal case; for realistic observations, the maximum PSF value will be lower by a factor of, by definition, the SR - see Eq. (2.3). As such, the maximum noise-free pixel intensity in the detector, $I_{\text{det}}^{1 \times 1}$, for a point source of magnitude $m_{\text{L}'}$ is estimated by:

$$I_{\text{det}}^{1 \times 1} = \max I_{\text{det}}(i, j, m_{\text{V}}) = \eta_{\text{PSF}}^{1 \times 1} \cdot \text{SR} \cdot F(m_{\text{L}'}) \tag{2.22}$$

assuming, once again, a unitary detector photon-electron conversion gain and quantum efficiency.

Similarly, one can define the scaling factor for a 3×3px reference area ($\approx \text{FHWM}_{\text{PSF}}$) by considering the sum of the 3×3px kernel centred at the maximum valued diffraction-limited PSF pixel:

$$\eta_{\text{PSF}}^{3 \times 3} = \sum_{k=-1}^{1} \sum_{l=-1}^{1} \text{PSF}_{\text{DL}}(i_{max} + k, j_{max} + l) = 0.3170 \tag{2.23}$$

where $i_{max}, j_{max} = \text{argmax}_{ij} \text{PSF}_{\text{DL}}(i, j)$ are the raster coordinates for the maximum intensity pixel of the normalised diffraction limit PSF array, PSF_{DL}. Extrapolation to different (i.e. realistic) PSFs is not as straightforward as for case of 1×1px reference area since the Strehl ratio does not provide information about the topology of the PSF across the 3×3px kernel considered. Nevertheless, for the diffraction-limited case:

$$I_{\text{det}}^{3 \times 3}(DL) = \eta_{\text{PSF}}^{3 \times 3} \cdot F(m_{\text{L}'}) \tag{2.24}$$

The flux of a single point-source measured by the detector in a 1×1px reference area is estimated by the ideal noise-free maximum pixel intensity, $I_{\text{det}}^{1 \times 1}$ - cf. Equation (2.22) - scaled by the system throughput efficiency, η_{opt}, and by the detector quantum efficiency, η_{QE}:

$$\phi_{\text{src}}^{1 \times 1} = \eta_{\text{opt}} \, \eta_{\text{QE}} \, I_{\text{det}}^{1 \times 1} \tag{2.25}$$

Similarly, the reading in the detector resulting from background emission is estimated, in turn, by the background intensity, I_{bg} (cf. section **??**):

$$\phi_{\text{bg}} = \eta_{\text{opt}} \, \eta_{\text{QE}} \, I_{\text{bg}} \tag{2.26}$$

The total measured noise, ϕ_n, derives from all the previously defined noise components - namely, background emission, dark current, shot noise, and readout noise. Assuming that the mean value of the background, dark-current, and shot-noise photo-electron counts can be entirely subtracted from the produced images, the resulting reduced noise of the imager, ϕ_n', is the result of the remaining shot noise and the readout noise of the detector:

$$\phi_n' = \sqrt{(\phi_{\text{src}}^{1 \times 1} + \phi_{\text{bg}} + \phi_{\text{DC}}) \cdot \text{DIT} + \sigma_{\text{RON}}^2} \tag{2.27}$$

By analysing the different noise contributions in (2.27) - cf. Figure 2.17 - one can observe that the background emission generally grossly dominates the overall noise estimation, only identical in value of the readout-noise for extremely small DIT.
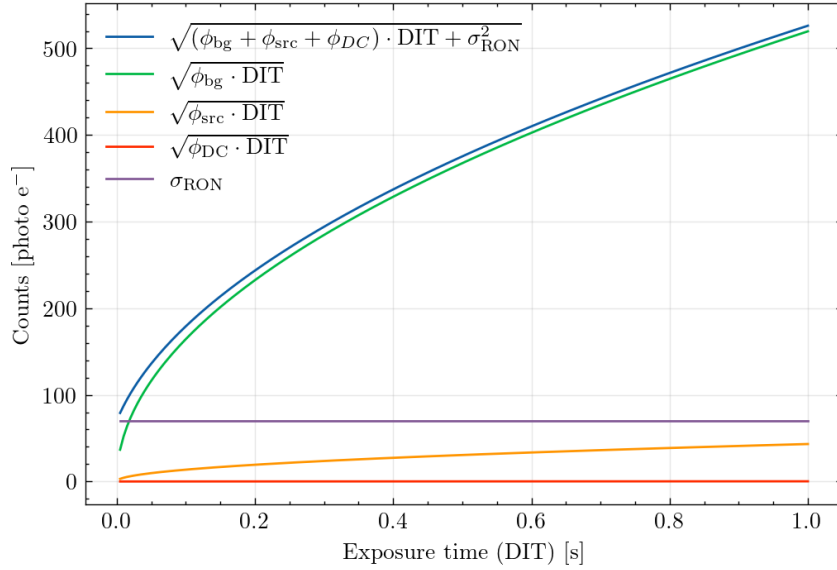
Figure 2.17: Photon and readout noise contributions as a function of DIT.

2.5.2 Signal-to-noise ratio (SNR) estimation

Considering that the background median can be removed, the signal-to-noise ratio, SNR, per detector integration time, DIT, can be approximated by [48]:

$$\mathrm{SNR_{DIT}} = \frac{\mathrm{DIT} \cdot \int_{\Omega_{\mathrm{SNR}}} \phi_{\mathrm{src}}\, d\Omega}{\sqrt{\omega_{\mathrm{SNR}} \cdot \left[(\phi_{\mathrm{bg}} + \phi_{\mathrm{DC}}) \cdot \mathrm{DIT} + \sigma_{\mathrm{RON}}^2\right] + \mathrm{DIT} \cdot \int_{\Omega_{\mathrm{SNR}}} \phi_{\mathrm{src}}\, d\Omega}} \tag{2.28}$$

where ϕ_{src} is the photo e$^-$ rate, Ω_{SNR} is the reference solid angle over which the source flux is calculated, and ω_{SNR} is the pixel reference area in pixels over which the background is estimated. The remaining variables retain the definition presented previously.

For an observation comprised of a number - NDIT - of exposures with duration DIT, the resulting SNR is given by:

$$\mathrm{SNR_{obs}} = f_{\mathrm{bg}}\, f_{\mathrm{NDIT}}\, \mathrm{SNR_{DIT}} \tag{2.29}$$

where

$$f_{\mathrm{NDIT}} = \frac{\mathrm{NDIT}}{\sqrt{\mathrm{NDIT}}} = \sqrt{\mathrm{NDIT}} \tag{2.30}$$

is the factor resulting from the increase of exposure frames, and f_{bg} is the background subtraction factor, with $f_{\mathrm{bg}} = \frac{1}{2}\sqrt{2}$ for a 2-point dither observation strategy, and $f_{\mathrm{bg}} = \frac{1}{2}$ for a chopping/nodding strategy.

It is clear that a unique, absolute SNR can't be defined as it varies with respect to the reference solid angle over which the source flux is estimated, Ω_{SNR}, and the reference area over which the background is estimated, ω_{SNR} - see Eq. (2.28). For the present case, it is useful to consider two distinct reference areas[18]:

- 1×1px, corresponding to the maximum of a pixel-centred point source;

- 3×3px, corresponding to $\approx$ FWHM of the point spread function;

---

[18]Considering the approximation of Ω_{SNR} to the pixel area identical to ω_{SNR}.

For a reference area of 1×1px for both the source and the background, one obtains:

$$\text{SNR}_{\text{obs}}^{1 \times 1} = f_{\text{bg}} \frac{\phi_{\text{src}}^{1 \times 1} \cdot \text{DIT} \cdot \sqrt{\text{NDIT}}}{\sqrt{(\phi_{\text{src}}^{1 \times 1} + \phi_{\text{bg}} + \phi_{\text{DC}}) \cdot \text{DIT} + \sigma_{\text{RON}}^2}} \tag{2.31}$$

where the noise term matches equation (2.27). Similarly, for a 3×3px reference area one obtains:

$$\text{SNR}_{\text{obs}}^{3 \times 3} = f_{\text{bg}} \frac{\phi_{\text{src}}^{3 \times 3} \cdot \text{DIT} \cdot \sqrt{\text{NDIT}}}{\sqrt{3^2 \cdot [(\phi_{\text{bg}} + \phi_{\text{DC}}) \cdot \text{DIT} + \sigma_{\text{RON}}^2] + \text{DIT} \cdot \phi_{\text{src}}^{3 \times 3}}} \tag{2.32}$$

2.5.3   Ideal detector integration time (DIT) estimation

Given Equation (2.28) defining the SNR for a single DIT, we denote that:

$$\text{SNR}_{\text{DIT}} \propto \frac{\text{DIT}}{\sqrt{\text{DIT}}} = \sqrt{\text{DIT}} \tag{2.33}$$

As such, it is advantageous to consider large integration times to increase the observation's SNR. However, close to the full-well limit of the detector, observe a drastic degradation in linearity is observed - cf. Fig. 2.16a -, which imposes a limitation on the integration times that can be practised. Additionally, a selection of large DIT imposes high absolute background counts in the detector, thus effectively limiting the flux resulting from stellar sources that can be imaged without saturation. As such, the selection of the DIT should balance the increase of SNR derived from its increase, the linearity error introduced, and the magnitude range to be observed without saturation.

It is denoted that the maximum detector pixel reading corresponding to the peak of a point-source of magnitude m_V derives from the object flux and the noise contributions:

$$I = \phi_{\text{src}}^{1 \times 1} + \phi_n \tag{2.34}$$

with the respective value for various magnitudes as a function of the detector integration time (DIT) presented in Fig. 2.18.
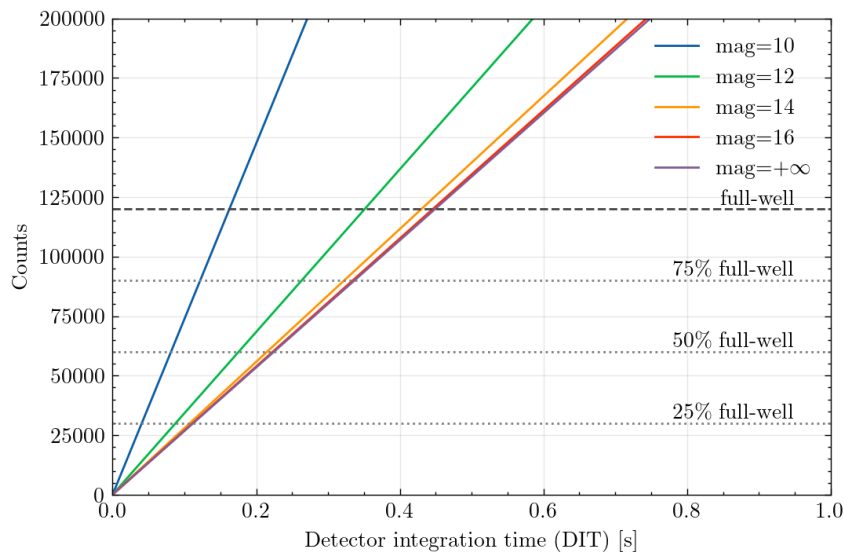
Figure 2.18: Maximum pixel counts as a function of DIT for various magnitude point sources.

From the analysis of Fig. 2.18, a fill-ratio target of $\sim 50\,\%$ of detector full-well is proposed. This shall allow for imaging without saturation sources with magnitude $L' \leq 11$, whilst resulting in a reasonably low linearity error $(< 5\,\%)$ for the faintest sources. From the analysis of Figure 2.18, it is estimated that the DIT corresponding to this fill-ratio target is approximately:

$$\text{DIT} = 0.2\,\text{s} \tag{2.35}$$

resulting from the intersection of the detector count curve for $\text{L}' = \infty$ with the proposed fill-ratio.

Although this value might seemingly lead to the gross saturation of lower-magnitude sources, it provides the optimal operating point for their higher-magnitude counterparts. This saturation is generally of no concern since these sources already present high SNR regardless of integration time, and their observation can be easily addressed by simply choosing appropriate exposure times or even relying on telescopes with significantly lower collecting power.

Finally, considering this DIT Eq. (2.31), it is possible to define the SNR curve for different magnitudes as a function of the complete exposure time (i.e. $\text{DIT} \cdot \text{NDIT}$) - see Fig. 2.19.
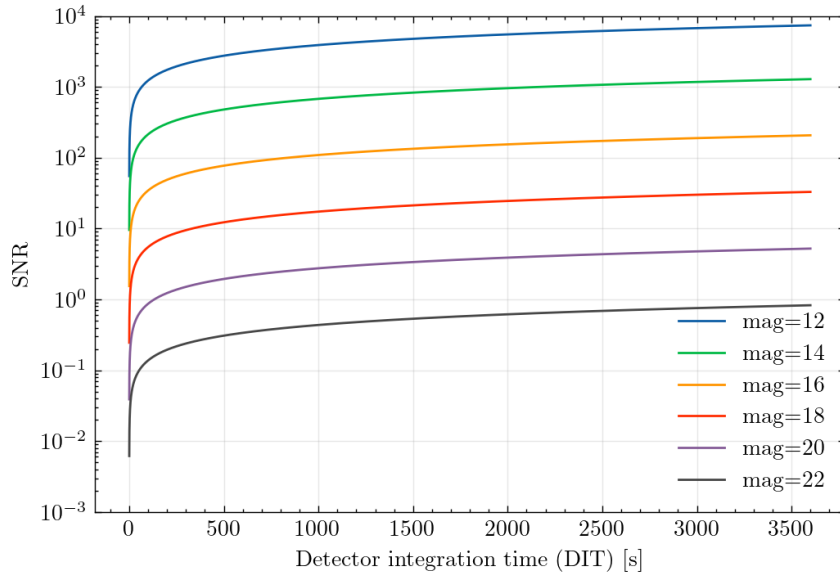
Figure 2.19: SNR as a function of integration time for reference area $1 \times 1\text{px}^2$.

2.6   Point-source catalogue

The point source catalogue used is derived from the VizieR Milky Way nuclear star cluster catalogue in Ks band [49, 50]. Based on [51], the authors have extrapolated this catalogue to the L' band assuming:

$$m_{\text{Ks}} - m_{\text{L}'} = 1.48 \pm 0.1$$

and synthetically expanded to higher magnitudes, assuming a spatially uniform distribution of sources. The magnitude distribution of the catalogue is presented in Fig. 2.20.

Of the provided catalogue, a patch of $10'' \times 10''$ is considered, centred at the middle point of the maximum and minimum coordinates for each axis[19]. This encompasses a total of $28\,804$ point source objects, with a limiting magnitude of $L' \approx 22$. The spatial distribution of the points sources in the catalogue is presented in Fig. 2.20.

---

[19]That is, the centre point of the patch coincides with the centroid of the minimum bounding box of the original catalogue.
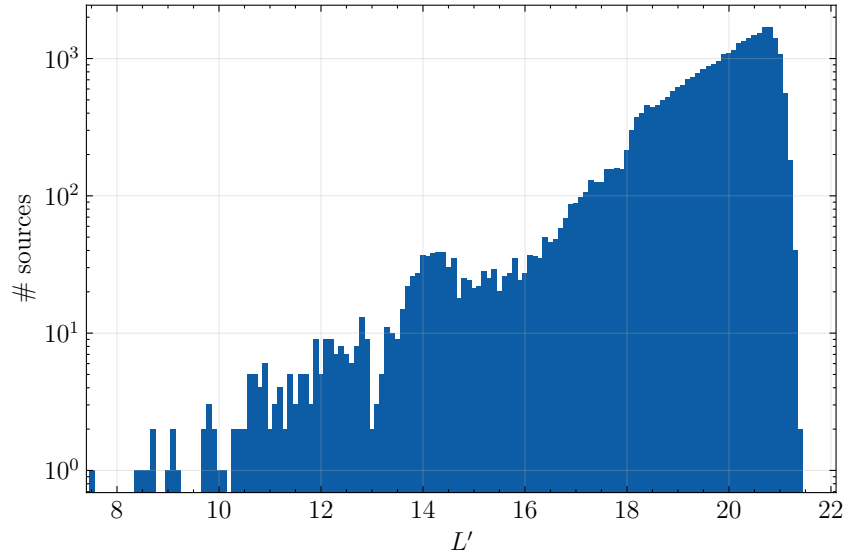
Figure 2.20: Histogram of L' magnitude for the objects in the catalogue considering a bin width of $\Delta L' = 0.1$.

(a) Full catalogue

(b) Magnitude $L' < 16$
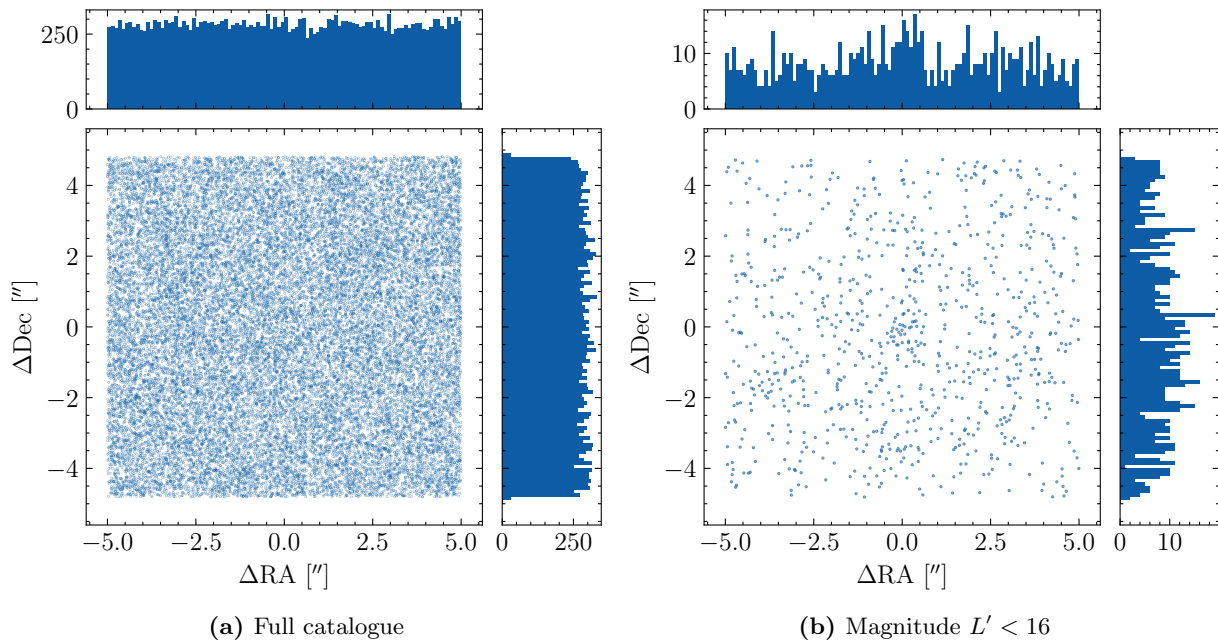
Figure 2.21: Objects in the observed field-of-view.

2.7 Generated images

A total of four images were simulated based on different point spread functions. All images were generated considering DIT = 0.2 s and NDIT = 18000, resulting in a total integration time of $t_{\text{exp}} = \text{DIT} \times \text{NDIT} = 3600$ s. No specific observation strategy was considered; therefore, the final images result from the integration of all the frames centred at the target.

For the first image - Fig. 2.22a - it was considered a field-constant Gaussian PSF with FWHM = 20.03 mas - approximately the resolving power of a circular pupil of the size of the ELT. This is an unrealistic case since it does not represent the diffraction pattern of the ELT pupil. Nevertheless, it is useful for comparison with the following cases since it does not present the effects of the complex morphology of the actual diffraction limited PSF.

The second image - Fig. 2.22b - was generated using the diffraction-limited PSF of the ELT. This is the ideal case for the specified aperture of the telescope, as it disregards atmospheric turbulence, AO correction, and other aberrations to the imaged wavefront.

The last two simulated images - Fig. 2.22c and Fig. 2.22d - were generated from end-to-end simulated PSFs, with the first assuming a field-constant PSF on axis with the AO guide star, and the latter introducing field-variability across the field-of-view. These are the most realistic images, including manifestations of atmospheric turbulence and AO correction.

(a) Gaussian PSF

(b) ELT diffraction limited PSF

(c) Field-constant METIS PSF

(d) Field-variable METIS PSF
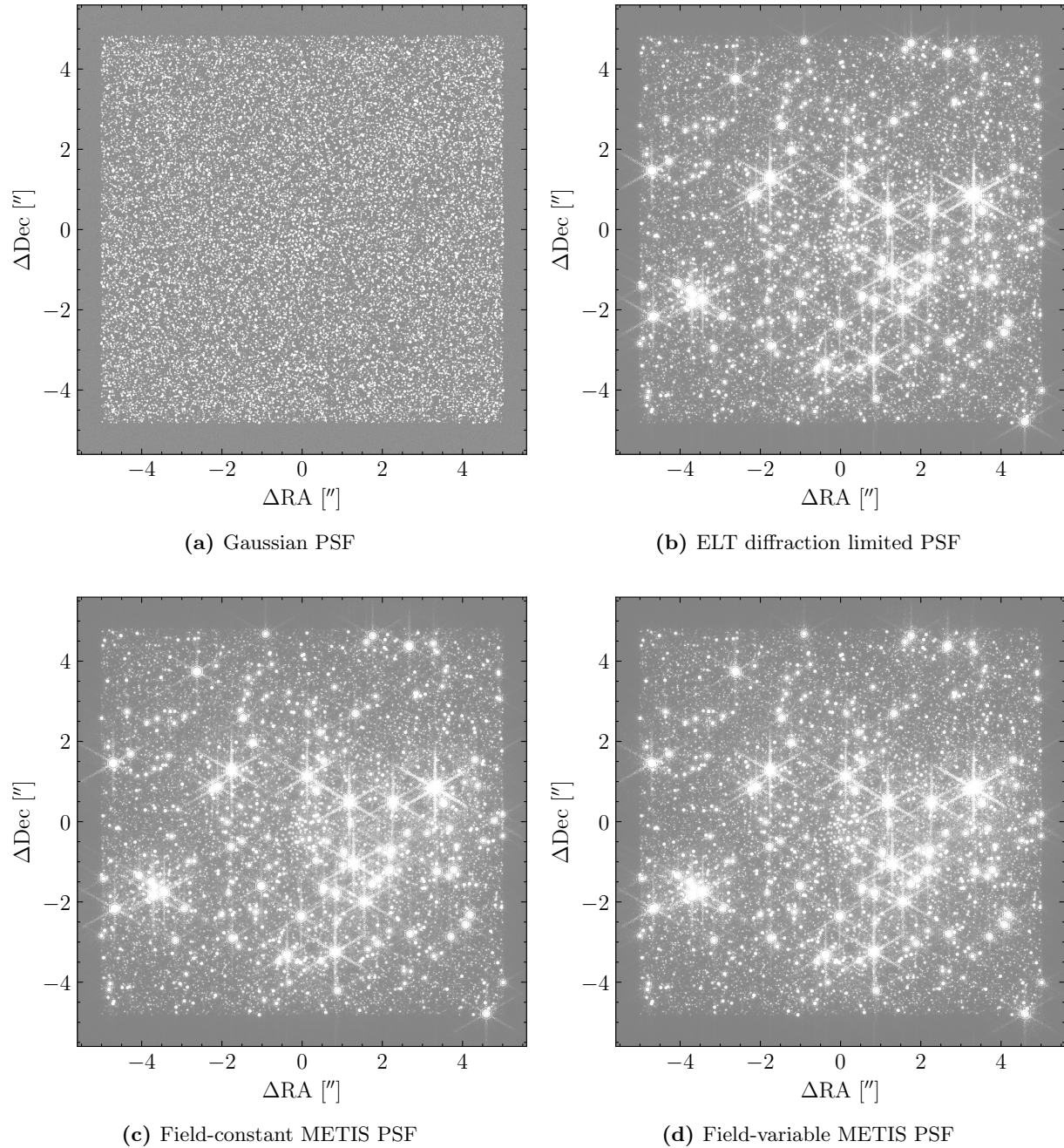
Figure 2.22: Images generated using the pipeline described.

Chapter 3

The inverse problem: Extracting point sources from images

Over the years, several tools for photometric and astrometric analysis of astronomical images have been developed. These range from general-purpose tools to custom pipelines developed for reducing data from specific instruments. Since no public (and stable) pipeline for this purpose has been provided for the METIS instrument, we will rely on the former family, the general-purpose tools. From these, we consider three of the arguably most widely used packages: Peter B. Stenson's DAOPhot [21] (and variation of thereof), AstrOmatic's `SExtractor` [22] along with its companion package PSFEx [52], used for PSF extraction, and `StarFinder` [53, 54].

DAOPhot

Peter B. Stetson's `DAOPhot` [21] is one of the oldest (1987) general-purpose photometry tools developed, yet it still assumes a dominant role in the field. Its focus relies on crowded field photometry, and despite more recent updates and newer versions of the package having been released, the core working principles and functionality have remained the same since its inception.

`DAOPhot` provides a collection of routines and utilities that can compose both aperture and PSF-fitting photometry/astrometry pipelines. A usual PSF-fitting pipeline can summarily be described:

1. First, the background is estimated and subtracted from the image to be reduced;

2. Next, high-luminosity point source objects are identified, and their centroid estimated;

3. Aperture photometry is performed on these sources;

4. A subset of the identified point source objects are selected and subsequently used to model the instrument's PSF.

5. The extracted PSF model is then fitted to the identified objects, thus providing better astrometric and photometric estimations. This process can be run iteratively by subtracting the fitted PSF profile for each star and retrying to identify and fit fainter stars that may have been occluded previously.

The `DAOPhot` PSF extraction procedure relies on fitting the extracted samples to one of the available analytical models - including Gaussian, Moffat [55], and Lorentz functions, amongst others. To increase the accuracy of this first-order approximation, it is possible to generate empirical look-up tables with corrections for the fitted model.

SExtractor/PSFEx

AstrOmatic's `SExtractor` [22] is a relatively more recent package (1996) with a core focus on extragalactic studies. Apart from stellar (point source) extraction, it also allows for star/galaxy

classification and the extraction of several galactic morphology parameters. For crowded field stellar astrometry, `SExtractor` became highly competitive with other offerings with the addition of model fitting and the release of the `PSFEx` companion package [52] for fitting empirical field-varying PSFs from observations.

The `SExtractor` pipeline is similar to the `DAOPhot`. Summarily, it is comprised of the following steps:

1. The background is estimated and subtracted from the provided image;

2. Objects (e.g. unresolved point sources) are identified based on their luminosity; optionally, a smoothing filter can be applied at this step to reduce spurious and close sources that might be blended are separated.

3. Astrometry is performed based on the methods available, such as centre-of-mass estimation and model (PSF) fitting;

4. Photometry is calculated based on an aperture approach or as part of the model fitting process.

Each of these steps shall be addressed in more detail in the following section.

The extraction of the PSF is performed separately by the `PSFEx` package. The unresolved objects used for this process can be manually provided by the user, or they can be automatically extracted during a first aperture photometry/astrometry run of `SExtractor`. Contrary to `DAOPhot`, the `PSFEx` routine may use a pixel basis for extracting/fitting the PSF model. Alternatively, others basis can be used, such as a Gauss-Laguerre basis or one provided by the user.

StarFinder

`StarFinder` [53, 54] is an `IDL` code geared towards the photometric and astrometric analysis of stellar fields. It relies in a pipeline which is overall similar to that of the previous packages, starting with background estimation subtraction, followed by star detection by thresholding, and finally PSF extraction and fitting. The PSF extraction can be done directly on the imaged field. Summarily, this is achieved in the image pixel basis by selecting several stellar samples, which are then cleaned (background-subtracted and contamination of nearby stars removed), re-centred, stacked, and its median calculated. The effects of anisoplanicity are introduced by the convolution of the extracted PSF with an elliptical Gaussian kernel. The parameters of the Gaussian profile are equally estimated from stellar samples extracted from various regions of the image and fitted to a spatially variable polynomial. Optional procedures, such as filtering and deblending of close sources - similar in purpose to the analogous methods in `SExtractor` - are also available. Similarly to `DAOPhot`, the source identification and fitting can be iterated with the identified sources subtracted from the image, thus providing better estimations for the local background level and

Why SExtractor/PSFEx?

All of the proposed packages are highly capable and widely used in astrometric and photometric work. Without clear evidence of the optimal choice for the observations in hand[1], it is of interest to perform a systematic analysis of the performance of each pipeline. Nevertheless, this exceeds

---

[1]Namely, of highly crowded fields imaged by extremely large telescope with segmented mirror pupils and adaptive optics.

the focus of this work, such that only one of the software packages shall be considered henceforth. To motivate this choice, a brief comparison of the capabilities and characteristics of the proposed options should be considered:

- **Capabilities:** All of these packages are highly capable for astrometric and photometric work and include a plethora of PSF extraction and fitting routines. Nevertheless, it should be noted that both StarFinder and SExtractor/PSFEx allow for pixel basis PSF extraction and fitting, whilst DAOPhot is restricted to the use of analytical models with optionally added look-up tables of empirical corrections.

- **Availability:** Both SExtractor/PSFEx and StarFinder are available online. SExtractor/PSFEx are licensed under a permissive GPLv3 license, whilst no license was easily identified for StarFinder. Finally, DAOPhot is not openly available online.

- **Requirements:** SExtractor and PSFEx are mostly developed in the C programming language, whilst DAOPhot is based on Fortran. Both of these languages are open standards with various high-quality open-source compilers available. On the other hand, StarFinder is based on IDL, a proprietary non-free programming language.

- **Documentation:** Documentation is available for all of these packages in the form of manuals, either provided by the developers or by third-party users. In this respect, SExtractor/PSFEx and DAOPhot provide arguably better documentation. Additionally, interactive online documentation is available for the SExtractor and PSFEx packages.

As demonstrated in Sec. **??**, the realist PSF of the ELT METIS instrument is considerably complex. To avoid introducing nonphysical constraints on the PSF morphology during the extraction procedure, it is preferable to opt for approaches relying on pixel basis - e.g. PSFEx and StarFinder - instead of analytical models - e.g. DAOPhot.

The availability of the code and of the associated software requirements also lead the selection criteria. In this regard, of the solutions analysed only SExtractor/PSFEx is openly available online and has free open-source dependencies.

More so, during experimentation, it was found that SExtractor/PSFEx had extremely compelling computational performance, allowed for vectorised mathematics parallelisation, and was designed to function with configuration files without the need for user input. These characteristics are crucial for automating the testing and final batch processing of different configurations.

For the described reasons and selection criteria, SExtractor/PSFEx were selected as the astrometry/photometry tools to be used in this work.

3.1 Using `SExtractor/PSFEx`

As specified previously, in this work, the `SExtractor` and `PSFEx` software packages are considered for the astrometric analysis of the simulated images. For this purpose, a model-fitting approach is considered, in which the PSF model is extracted directly from the observations. This approach is achieved with a pipeline composed of three major steps:

1. Aperture photometry

2. ePSF model extraction

3. ePSF model fitting

In the first step of the pipeline, in a process similar to the commonly known *aperture photometry*, the position and flux of point sources are extracted by `SExtractor`. This is achieved
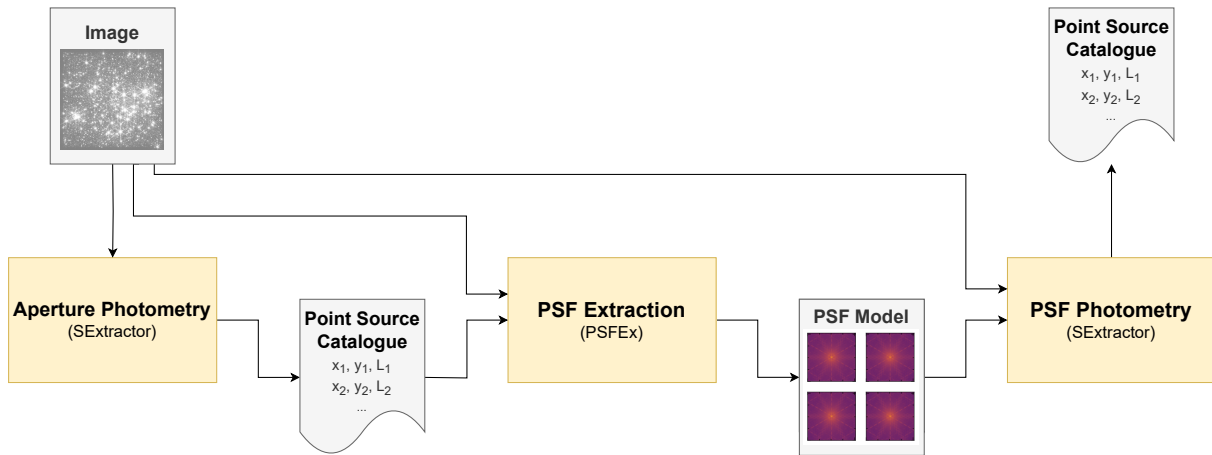
Figure 3.1: Block diagram of the 3-step astrometry/photometry pipeline.

based on the analysis of small patches of the image - *apertures* - and only detections with high flux and high SNR are considered at this stage.

The second step of the pipeline consists in extracting the effective PSF of the system by relying on the `PSFEx` package. This is achieved by fitting samples of (ideally) isolated point sources extracted in the previous step.

At last, the generated PSF model is used for the final extraction of point source objects with `SExtractor`. This is achieved using a model fitting approach, resulting in the final photometric/astrometric catalogue for the provided image.

To better understand and contextualise the building blocks of the proposed pipeline, a brief description of the tools and methods used is now presented.

SExtractor

The operation of the `SExtractor` software can be summarised by the following steps, performed sequentially and without user interaction, based on the configuration file provided:

1. ***Background estimation and subtraction:*** Mapping of background parameters (e.g. RMS noise) across the image and subsequent subtraction. These are estimated for patches of specified area and interpolated over the total area using a bi-cubic spline.

2. ***Image filtering:*** Optional step where a convolution of the image with a small filter kernel (e.g. $5 \times 5\text{px}^2$ FHWM = 3 px Gaussian) is performed mainly to reduce the impact of bad pixels, spurious high- or low-count pixels, etc.. This is only used for the detection of objects (i.e. point sources or galaxies), as the last photometry measurements are performed on the original image.

3. ***Object finding (thresholding):*** Possible objects are extracted from the background-subtracted and filtered image by segmenting groups of adjacent pixels above a defined pixel value threshold (e.g. some multiple of the background value estimation standard deviation).

4. ***Deblending:*** An attempt to separate individual objects that might have been identified in the previous step as a single entity is performed. Briefly, this is achieved by identifying groups of pixels within the segmented region interposed by lesser-valued pixels according to a defined threshold.

5. ***Perform astrometry:*** The centroid of the objects found is estimated. This can be achieved in various ways, such as:

   - Barycenter approach - By calculating the barycenter of the isophotal footprint - i.e. the group of pixels extracted in the object finding step;

   - Windowed centroid based on a Gaussian profile - similar to the previous method, but the integration is performed over a window defined by a Gaussian profile, which is iteratively scaled to the object;

   - Model fitting - The provided model is fitted to each object identified in the finding step. This is achieved by minimising a loss function[2] involving the background-subtracted pixel values of the detection and the model provided in the pixel basis, using the Levenberg-Marquardt algorithm [56, 57, 58].

6. ***Perform photometry:*** Photometry data is estimated for the detected objects. This step can be performed based on different approaches for selecting the region to be analysed. Some examples include using the isophotal area, using a flexible aperture, or using a user-defined circular aperture. Alternatively, the flux can be obtained as a result of the model fitting step in case a PSF model is provided.

This is a brief overview of the main steps of a standard `SExtractor` run. Some procedures have been omitted, mostly for simplicity, since they are either optional and only run if one of the resulting values is requested by the user, or they are related to the classification of galaxies and related parameter estimation, which is of no importance for the task in hand. For a more detailed overview, please see the original paper [22], the paper describing `PSFEx` and the implementation of model-fitting in `SExtractor` [52], and the existing documentation (https://sextractor.readthedocs.io/).

PSFEx

PSFEx is a SExtractor-associated package geared towards the extraction of models from astronomic images to further be used for PSF photometry. Its release only occurred much later than the appearance of the `SExtractor` software and was accompanied by the addition of model-fitting capabilities to the original `SExtractor`. The complete pipeline can summarised in two distinct steps:

1. The catalogue of patches - also referred to as *vignettes* - is examined, the samples representing point sources are identified, and an initial filtering is performed to discard samples that are not suitable for PSF extraction. Some accepted rejection criteria for a possible sample include:

   - being saturated

   - having a small SNR

   - displaying high ellipticity

   for all of which the user may provide suitable parameters.

2. The resulting good-quality patches are utilised to fit a PSF model in the pixel basis - i.e. *direct space* - without assuming a subjacent analytical function [52]. Additionally, it

---

[2]For more details see [52] and https://sextractor.readthedocs.io/en/latest/Model.html.

is possible to allow for variations of the PSF model as a function on any of the available parameters. In this case, this functionality is used to allow for variations with respect to the positions of the sample in the field-of-view, thus effectively modelling the field-variability of the PSF.

Finally, the fitted model is saved in a FITS file, which can be provided to SExtractor for PSF fitting photometry and astrometry.

Other functionality is available, though it won't be addressed here since it is not focal to the task at hand. This includes the computation of homogenisation kernels and the output of various debug and quality assessment files. For more information, see the original paper [52], and the existing documentation (`https://psfex.readthedocs.io/`).

Some remarks on the quality of the samples

For a descriptive field-varying effective PSF, it is important that multiple high-quality samples are considered [59]. Although the quality of the samples might be difficult to define quantitatively, some requirements might be assumed:

1. Present high SNR;

2. Not be saturated;

3. Be well separated from other sources;

4. Not include spurious noise contributions or other intensity variations resulting from effects other than the system PSF;

amongst others. Additionally, when considering a field-variable model, it is also important that there is an adequate number of samples spatially distributed across the observed field, so as to minimise degradation of the fit due to less sampled regions.

This selection process is sometimes done manually, more so when there is a limited number of quality samples - thus requiring that their selection is judicious due to the resulting low statistical variability of the ensemble - and/or when there are no routines or pipelines to perform this step automatically. However, since we are dealing with a considerably crowded field, it is feasible to extract a representative number of good-quality samples covering the entirety observed field-of-view, therefore no manual selection is required. This is aided by the fact that the `PSFEx` package already includes various routines and configuration parameters to ensure the quality of the sources selected, such as allowing to define a threshold for the SNR and omitting saturated samples.

Detection cross-matching with catalogue

Finalised the point-source object extraction steps of the pipeline, the final procedure contemplates the evaluation of the suggested detections with the original catalogue used for the generation of the images. For this, a simple algorithm is proposed by which a correct extraction is ... the closest detection proposal lying within less than $3\,\mathrm{px}$ in each axis from a matching object in the catalogue.

Settings

The `SExtractor`/`PSFEx` software packages provide default configuration files geared towards multi-purpose stellar and galactic photometric and astrometric work. The default settings were manually adapted based on the characteristics of the METIS instrument and the specific observation target of interest - the centre of the Milky Way. Upon this, some automated optimisation was performed. This was achieved by defining sets of possible values for several parameters and running the photometry/astrometry pipeline for the resulting parameter space. The final configuration was selected from the plethora of tested variations as the one that minimised the astrometric error.

The parameters used for all the steps in the pipeline, namely, the initial aperture photometry step, the PSF fitting from the extracted object samples, and the final model-fitting photometry procedure, are presented in Appendix D.

Chapter 4

Results and discussion

4.1 Astrometry of single integrated exposures

In this section, the proposed photometry/astrometry pipeline discussed in Chapter 3 is used for analysing the images generated in Chapter 2. Several cases are presented, assuming successively more realistic images. These span from the simplest image assuming a field-constant Gaussian PSF to the most realistic case based on the field-varying simulated PSF. This gradual progression is not without purpose, as it shall allow for constraining the impact of the increasing complexity (and realism) of the images.

4.1.1 Case I: Image generated using a Gaussian PSF

For the first case considered, the image is generated using a field-constant Gaussian PSF with a full-width-half-maximum (FWHM) equal to the diffraction-limited angular resolution for a circular pupil with $D = D_{\mathrm{ELT}}$. The resulting image is processed by the PSF-fitting SExtractor/PSFEx pipeline described in Section 3.1. Despite the image being generated with a field constant PSF, no constraints of the spatial variability of the fitted PSF model were assumed in the PSFEx routine. The resulting astrometric error as a function of magnitude is presented in Fig. 4.1.
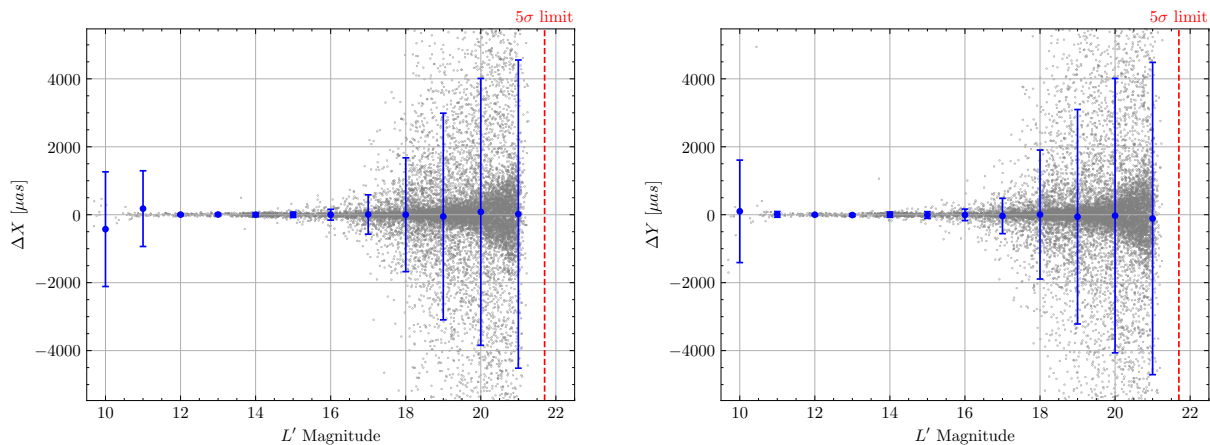
Figure 4.1: Astrometric error as a function of magnitude for the image generated using a Gaussian PSF. The blue markers represent the mean and standard deviation of the astrometric errors considering a bin width of $\Delta L' = \pm 0.5$

.

The theoretical astrometric precision limit [60] for a photon-limited system with a circular pupil of diameter D is:

$$\sigma_{\mathrm{meas}} \approx \frac{\lambda}{\pi D \sqrt{N}} \propto \frac{\mathrm{FWHM}}{\mathrm{SNR}} \tag{4.1}$$

where λ is the wavelength, N is the number of photo-electron counts in reference area of the detector resulting from the imaged source, SNR ($\propto \sqrt{N}$) is the photon-limited signal-to-noise ratio of the system[1], and FWHM ($\propto \lambda/D$) is the full-width at half-maximum of a noise-free point source assuming Fraunhoffer diffraction[2].

For the present case, however, the system is largely limited by the background flux - cf. Section 2.5.1. As such, Equation (4.1) is modified by considering the SNR estimations in Section 2.5.2 instead of the $\sqrt{N}$ term. Namely, it is considered the SNR for a reference area of $1 \times 1\mathrm{px}^2$, $\mathrm{SNR}_{\mathrm{obs}}^{1\times1}$ - cf. (2.31) -, as well as for the reference area[3] of $3 \times 3\mathrm{px}^2$, $\mathrm{SNR}_{\mathrm{obs}}^{3\times3}$ - cf. Eq. (2.32).

Figure 4.2: Standard deviation of astrometric error as a function of magnitude for the image generated using a Gaussian PSF. The red and green lines represent the ideal astrometric error as defined in Eq. (4.1) for SNR defined in $3 \times 3\,\mathrm{px}^2$ and $1 \times 1\,\mathrm{px}^2$ reference areas, respectively.

Some interesting considerations result from Figure 4.2. Firstly, for magnitudes $15 \leq L' < 20$, the standard deviation of the position of the extracted sources seems to follow the trend of the theoretical astrometric precision limit, approximately matching the limit for $\mathrm{SNR}_{\mathrm{obs}}^{1\times1}$, and exceeding it for $\mathrm{SNR}_{\mathrm{obs}}^{3\times3}$ by about $\sim 5\times$, which seems to be consistent with the literature [17].

For lower magnitudes, namely $12 \leq L' \leq 14$, the standard deviation of the experimental astrometric errors tapers off to an approximately constant value of $\approx 30\,\mu\mathrm{as}$, considerably higher than the proposed theoretical limit. Since in this case an ideal field-constant diffraction-limited Gaussian PSF is considered, this limiting value can be assumed as the minimum error mostly due to detector binning/sampling, crowding, and limitations of the photometry/astrometry pipeline itself. For $L' < 12$, however, the maximum pixel flux of a corresponding point source object reaches an operation point of high non-linearity of the detector - see Figure 2.16b - or it might even saturate - see Figure 2.18, resulting in the drastic deterioration in performance observed. Additionally, there are very few sources at these magnitudes; thus, any outliers - of which no filtering is performed - might have a significant statistical contribution.

Finally, for higher magnitudes - i.e. smaller source flux - the standard deviation seems to

---

[1]Assuming $\phi_{\mathrm{src}} \gg \phi_{\mathrm{bg}}, \phi_{\mathrm{DC}}, \sigma_{\mathrm{RON}}^2$, Equation (2.29) is reduced to:

$$\mathrm{SNR} \approx \frac{\phi_{\mathrm{src}} \cdot \mathrm{DIT} \cdot \sqrt{\mathrm{NDIT}}}{\sqrt{\phi_{\mathrm{src}} \cdot \mathrm{DIT}}} = \sqrt{\phi_{\mathrm{src}} \cdot \mathrm{DIT} \cdot \mathrm{NDIT}} = \sqrt{N}$$

considering $f_{\mathrm{bg}} = 1$.

[2]Or, more simply, the full-width at half-maximum of the PSF.

[3]This corresponds to $\approx$ FWHM of the diffraction-limited PSF.

transcend the theoretical limit. However, this is not a physical result, with this phenomenon possibly arising from the ΔX and ΔY distributions for $L' > 20$ exceeding the $\pm 3\,\mathrm{px}$ limit[4] imposed for the cross-matching algorithm. As such, one should be wary of quantitatively analysing the results for said magnitudes. Nevertheless, this is not significantly restricting since the theoretical precision limit for these magnitudes greatly falls behind in comparison with the expected performance of other current and future instruments geared towards precision astrometry [61, 62, 41]. Thus, further analysis should focus on $L' < 20$ where the ELT/METIS LM imager might theoretically provide meaningful astrometric precision.

4.1.2 Case II: Image generated with the diffraction-limited PSF

Now, we consider a more realistic case, in which the image is generated considering the diffraction-limited PSF assuming the actual ELT pupil M1 mirror[5]. A similar source extraction pipeline to the previous case is considered. The resulting astrometric error as a function of magnitude is presented in Fig. 4.3.
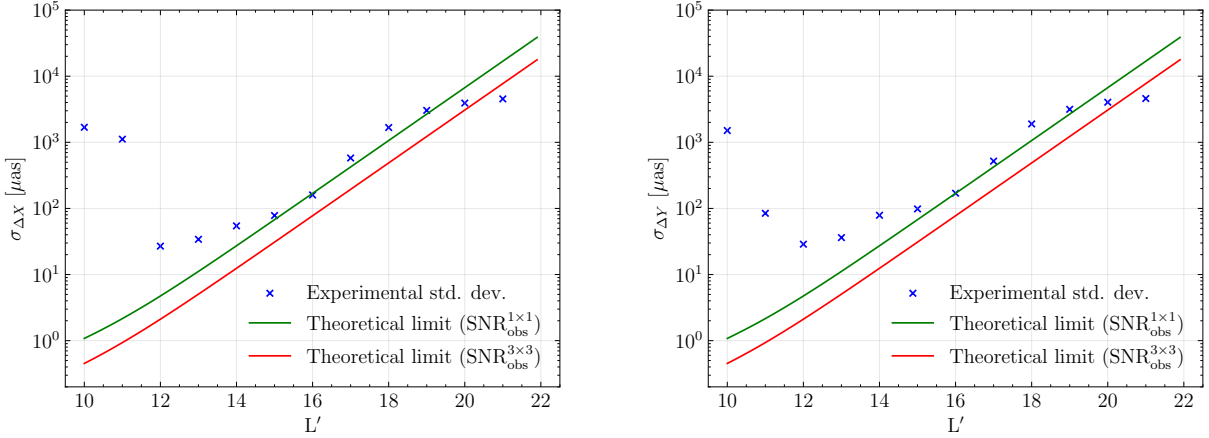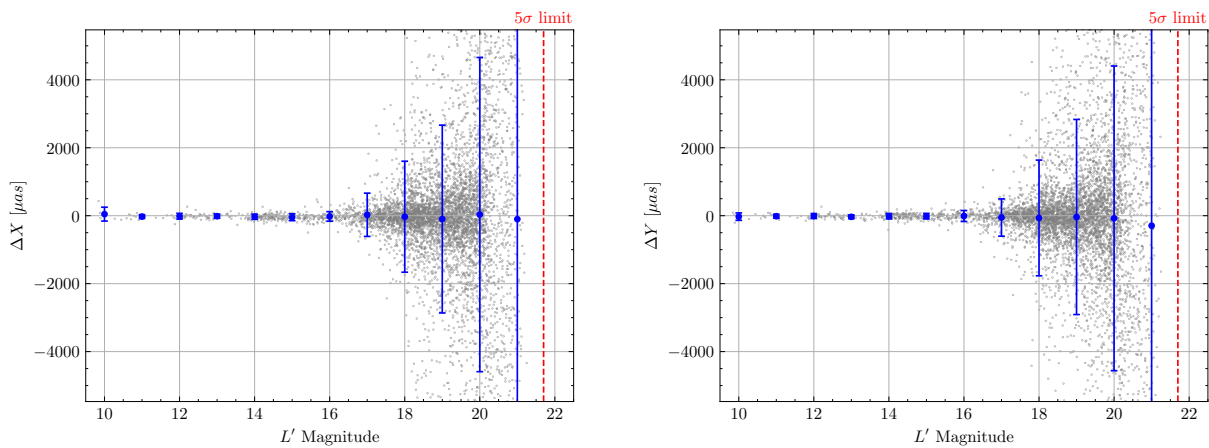

Figure 4.3: Astrometric error as a function of magnitude for the image generated using a diffraction-limited PSF. The blue markers represent the mean and standard deviation of the astrometric errors considering a bin width of $\Delta L' = \pm 0.5$.

This result does not differ drastically from the previous case, yet two main differences are notorious:

1. The sharp degradation for lower magnitudes occurs for $L' = 10$ instead of $L' \leq 11$;

2. There seems to be a more significant performance degradation for higher magnitudes.

A probable direct cause for 1. is the smaller amplitude of the peak of the ELT/METIS PSF in contrast with the Gaussian profile considered previously. Recalling (2.21), the peak value of the normalised[6] ELT diffraction-limited PSF array is:

$$\max \mathrm{PSF}_{\mathrm{ELT}} \approx 0.0476$$

whilst for the normalised Gaussian PSF with the same FWHM:

$$\max \mathrm{PSF}_{\mathrm{Gauss}} \approx 0.0593$$

---

[4]Corresponding to $\Delta X = 16.41\,\mathrm{mas}$, for the detector's pixel scale $d_{\mathrm{pix}} = 5.47\,\mathrm{mas/px}$.

[5]See Section 2.1.

[6]With respect to its integral.

This corresponds to a decrease of $\approx 20\%$ of the peak pixel source flux of a point-source object. Recalling that for $L' \sim 10$ one reaches the full-well limit of the detector - see Figure 2.18 -, this is enough to greatly reduce the number of saturated sources.

The decrease of the peak value of the PSF also results in a reduction of the objects' SNR. Since the astrometric precision is expected to be inversely proportional to the SNR - see Eq. (4.1) -, this might also motivate the overall impact on performance observed, more notoriously for higher magnitudes.
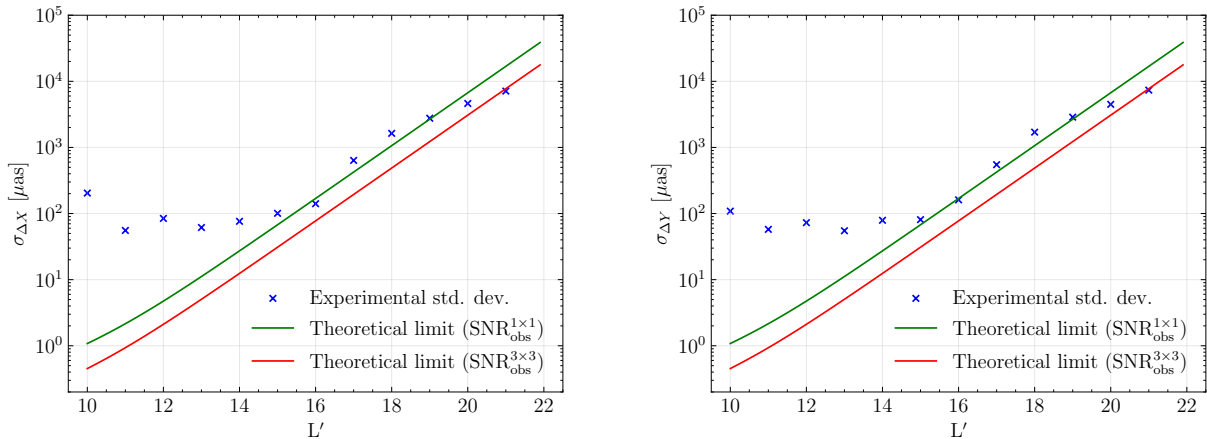
Figure 4.4: Standard deviation of astrometric error as a function of magnitude for the image generated using a diffraction-limited PSF. The red and green lines represent the ideal astrometric error as defined in Eq. (4.1) for SNR defined in $3 \times 3\,\mathrm{px}^2$ and $1 \times 1\,\mathrm{px}^2$ reference areas, respectively.

The astrometric precision seems, once again, to taper off to an almost constant value for lower magnitudes. However, comparing Fig. 4.2 and Fig. 4.4, there seems to be an increase by a factor of $2-3\times$ of the minimum achievable standard deviation relative to the previous case. This limit seems inconsequential of the SNR and, thus, it is unlikely to be a manifestation of the reduction in performance due to the decrease of peak PSF value. Since no other parameters of the simulation apart from the PSF utilised have been modified, this seemingly systematic limit is probably due to the increased complexity of the morphology of the PSF and the inability of the extraction pipeline to model it correctly.

4.1.3 Case III: Image generated with a field-constant end-to-end simulation PSF

As observed in Section 2.1, the simulated PSF for the METIS system differs considerably from the ideal diffraction-limited PSF due mostly to the contribution of atmospheric turbulence and its partial correction by the adaptive optics system. As such, the focus is now shifted towards the image, assuming the more realistic end-to-end PSF simulation. Here, the simulated PSF at the centre of the field[7] is utilised for the complete field-of-view - thus effectively assuming, once again, that the PSF is constant across the field. The resulting astrometric error as a function of magnitude is presented in Fig. 4.5.

It is easily noticeable that in contrast with the previous cases, a systematic error - or bias - arises for the mean value of the extracted point source objects' centroids coordinates. The present case is mostly similar to the former, both assuming a field-constant PSF and relying on the same extraction pipeline; nevertheless, the PSF considered does differ. As such, it is sensible

---

[7]See Figure 2.5.
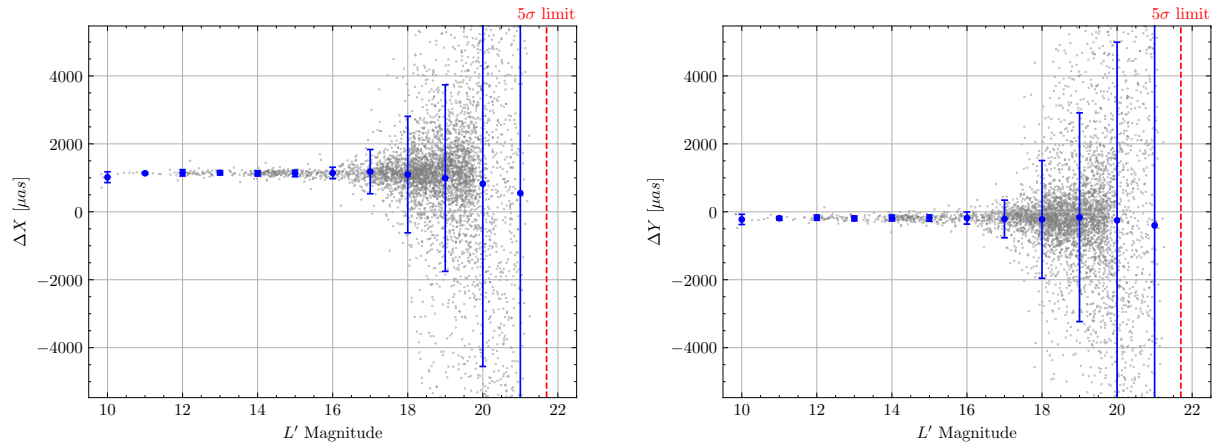
Figure 4.5: Astrometric error as a function of magnitude for the image generated using a simulated field-constant METIS PSF. The blue markers represent the mean and standard deviation of the astrometric errors considering a bin width of $\Delta L' = \pm 0.5$.

to gear our focus towards all the processes that lead to the definition or rely on the estimated effective PSF.

Each point source is effectively a representation of the system's PSF and is therefore used for its estimation from the scientific image. This is the basis of the PSF extraction, as described in Ch. 3. In the proposed astrometry pipeline, the samples of stellar objects are obtained from the initial aperture photometry step, in which the centroid of each sample is calculated by a simple barycenter estimation. As such, the incorrect estimation of this position, e.g. due to the effects of anisoplanatism, would lead to a centroid bias propagated to the samples used for extracting the PSF model and, subsequently, the final PSF photometry stage. To test this hypothesis, let us bypass the aperture photometry and the PSF extraction altogether.

Providing the PSF model

Since the precise simulated PSF is known, it can be directly provided to the photometry pipeline. For this, the central $55 \times 55\,\mathrm{px}^2$ patch of the end-to-end simulated PSF used for image generation is provided[8] as the model to be fitted to the image and, thus, PSF photometry is performed directly. The resulting astrometric error as a function of magnitude is presented in Fig. 4.6.

As expected, without the propagation of the astrometric error derived from the initial aperture photometry step, the bias observed previously is eliminated.

The results are comparable with the case of the diffraction-limited ELT PSF, without noticeable degradation deriving from the inclusion of AO-corrected atmospheric effects nor meaningful improvement due to directly providing the ideal PSF model to be fitted to the image.

4.1.4 Case IV: Image generated with a field-varying end-to-end SCAO simulation PSF

At last, we expand upon the previous case by admitting that the system PSF used for generating the astronomic images varies across the field. The complete PSF grid described in Sec.

---

[8]This procedure is not native to the *SExtractor* software. This is achieved by generating a file template of a PSF model similar to those provided by the `PSFEx` software and manually editing the data table defining the field-constant (i.e. 0-th order) PSF model.
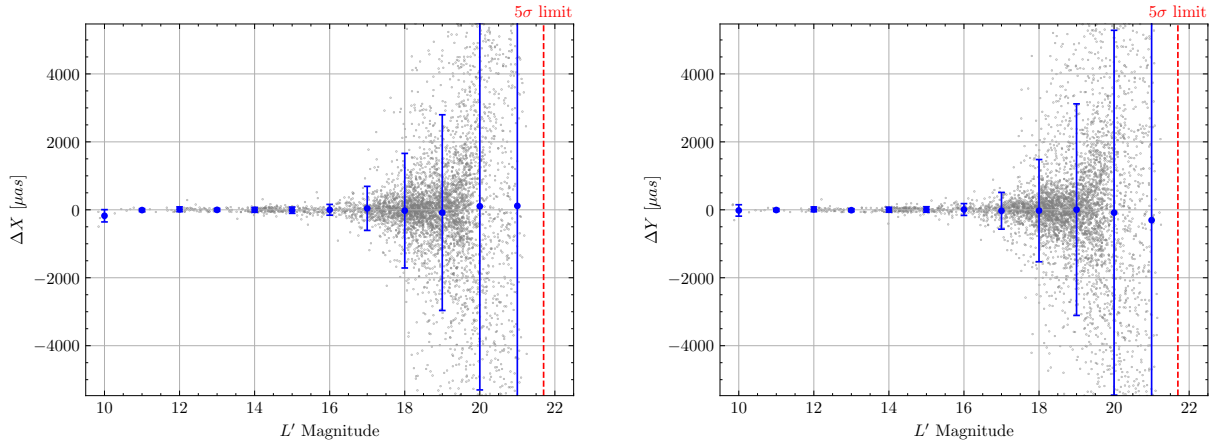
Figure 4.6: Astrometric error as a function of magnitude for the image generated using a simulated field-constant METIS PSF, with the PSF model directly provided to the astrometry pipeline. The blue markers represent the mean and standard deviation of the astrometric errors considering a bin width of $\Delta L' = \pm 0.5$.
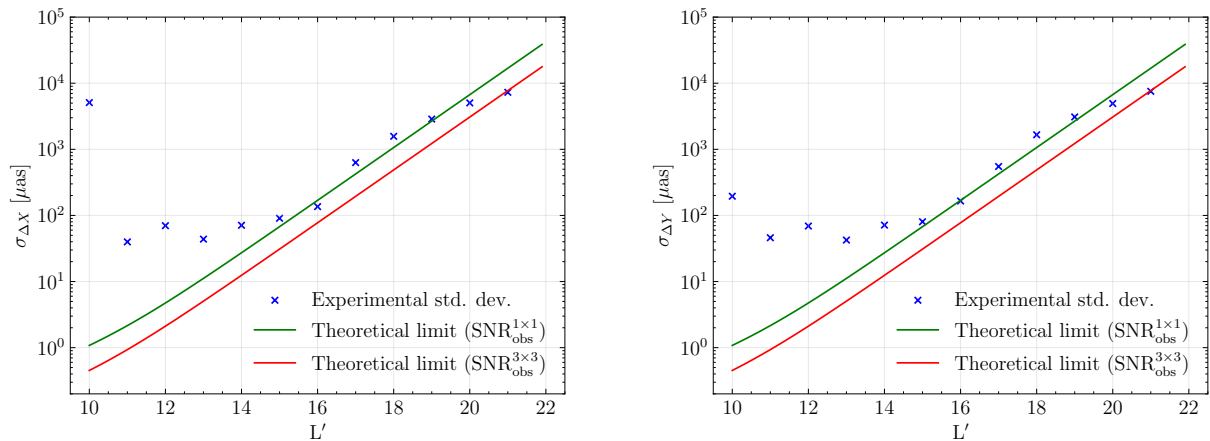
Figure 4.7: Standard deviation of astrometric error as a function of magnitude for the image generated using a simulated field-constant METIS PSF, with the PSF model directly provided to the astrometry pipeline. The red and green lines represent the ideal astrometric error as defined in Eq. (4.1) for SNR defined in $3 \times 3 \, \mathrm{px}^2$ and $1 \times 1 \, \mathrm{px}^2$ reference areas, respectively.

2.1 is used. Despite the marked inadequacy of the three-step photometry/astrometry pipeline discussed in the previous case, it is vital to verify the manifestation of the bias attributed to its utilisation in the current case. Thus, the complete pipeline is considered first. The resulting astrometric error as a function of magnitude is presented in Fig. 4.8.

As expected, a systematic error emerges when analysing images generated with realistic end-to-end simulated PSFs. Replicating the procedure from the previous case, the centre-most PSF of the PSF grid is explicitly provided in the SExtractor model fitting step, thus bypassing the first two steps of aperture photometry and PSF extraction discussed in Section 3.1, with the results presented in Figures 4.9 and 4.10. The resulting astrometric error as a function of magnitude is presented in Fig. 4.9.

From the analysis of Figure 4.9, it is interesting to note that providing a single PSF (e.g. that for the centre of the field) to the pipeline is sufficient to eliminate the otherwise observed bias, despite the underlying field-variability of the PSF used. Nevertheless, it isn't without meaningful degradation that one achieves this. Observing Figure 4.10, it is noticeable that the
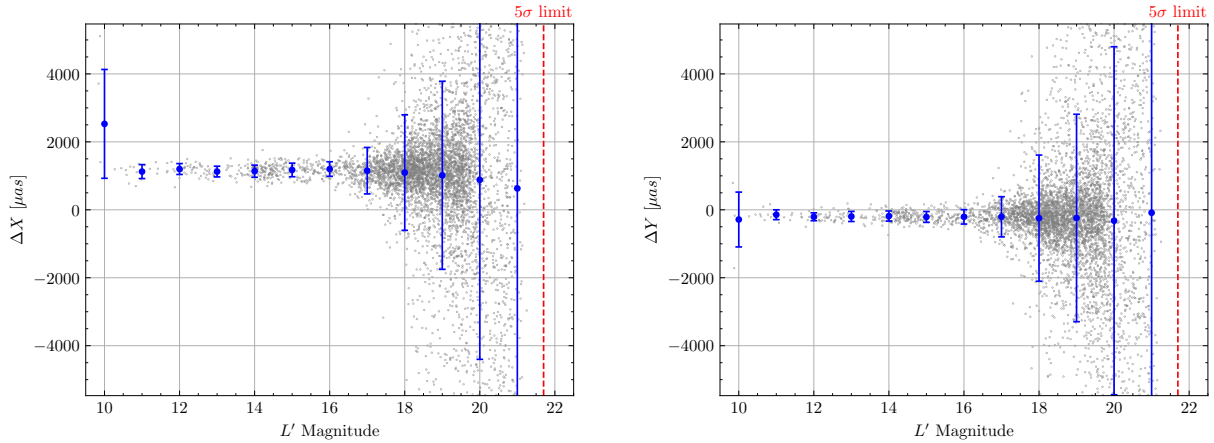
Figure 4.8: Astrometric error as a function of magnitude for the image generated using a simulated field-variable METIS PSF. The blue markers represent the mean and standard deviation of the astrometric errors considering a bin width of $\Delta L' = \pm 0.5$.
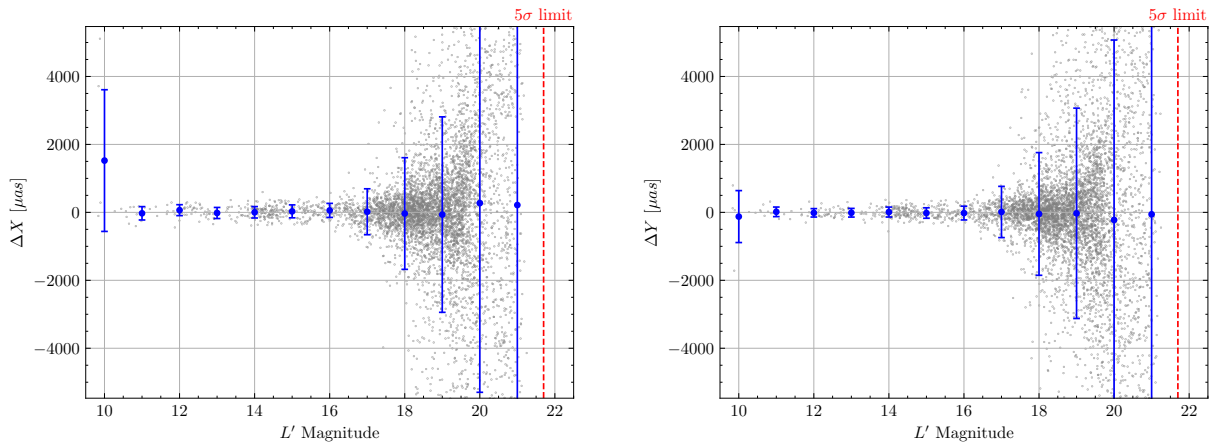
Figure 4.9: Astrometric error as a function of magnitude for the image generated using a simulated field-variable METIS PSF, with the PSF model directly provided to the astrometry pipeline. The blue markers represent the mean and standard deviation of the astrometric errors considering a bin width of $\Delta L' = \pm 0.5$.

limiting astrometric precision for lower magnitudes tapers off at $\sim 150\,\mu$as, which is considerably higher than for the previous tests.

It would be of interest to provide the complete grid of simulated PSFs to the *SExtractor* pipeline so as to minimise the degradation in astrometric precision due to not addressing the variability of the fitted PSF across the field. However, this is not a native functionality of the SExtractor/PSFEx pipelines, and doing so would require manual manipulation of the model files and the decomposition of the simulated PSF with respect to the polynomial basis for field-variability assumed by these packages.

4.1.5 Dicussion

Model fitting seems to be the preferred methodology for precision astrometry, with various works relying on tools such as `DAOPhot` [21], `SExtractor` [22], and `StarFinder` [53, 54] for this purpose. The success of this procedure, however, critically relies on the correct definition of the PSF model to be fitted to the image [31].
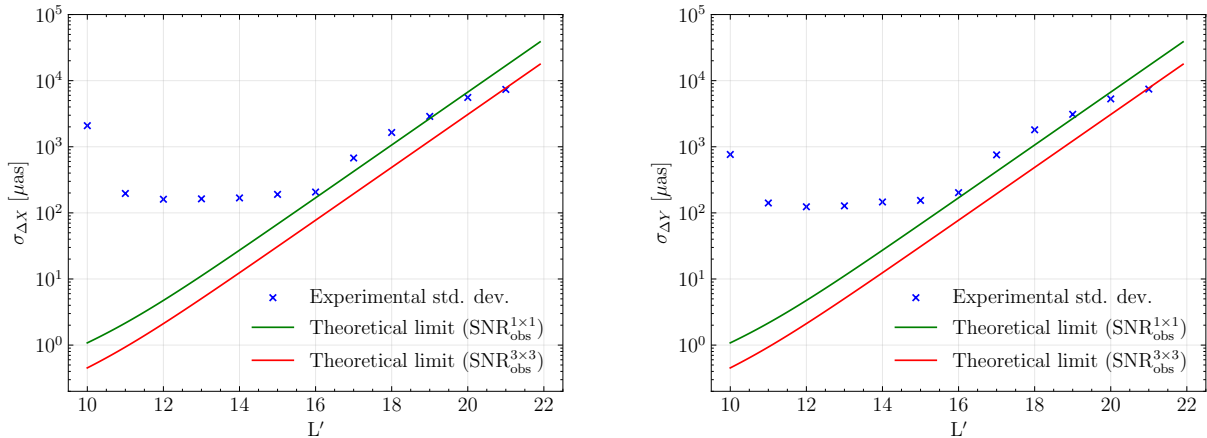
Figure 4.10: Standard deviation of astrometric error as a function of magnitude for the image generated using a simulated field-variable METIS PSF, with the PSF model directly provided to the astrometry pipeline. The red and green lines represent the ideal astrometric error as defined in Eq. (4.1) for SNR defined in $3 \times 3\,\mathrm{px}^2$ and $1 \times 1\,\mathrm{px}^2$ reference areas, respectively.

The model fitting approach has also been considered in this work, where the use of the SEXtractor/PSFEx software packages is explored. Overall, the extraction of the PSF model and its subsequent fitting in the image seem to be achieved with some degree of success. For relatively faint objects - namely $L' \geq 16$ - the derived astrometric precision is compatible with the theoretical precision limit and comparable to the case of providing the noise-free end-to-end simulated PSF as the model to be fitted - cf. Sections 4.1.2 and 4.1.3. However, for lower magnitudes, the results seem to indicate the presence of a limiting precision, regardless of the target object's SNR. This limiting precision varies depending on the case considered, reaching its highest value of $\sim 150\,\mu$as for the image generated from field-varying, end-to-end simulated PSFs. One should note, however, that this limit is not solely physical in nature and is largely intertwined with the limits of the analysis procedure itself - namely, the use of `SExtractor` and PSFEx, as well as the disregard of field-variability in the provided model for PSF phometry/astrometry - cf. Section 4.1.4. In fact, the degradation in performance has been identified in other works such as Neichel, B. et al (2014) [61], where a similar astrometric error floor is observed, in contrast to other software such as StarFinder. Thus, despite the `SExtractor`/`PSFex` suite being one the most promising and few free, non-proprietary, and publicly available software packages for general photometry and astrometry, one should analyse other alternatives - shall this be possible - such as `StarFinder` if precision astrometry is the main goal.

Despite this limitation, the analysis provided so far has allowed to address other important issues related to the task of direct-imaging precision astrometry with the ELT/METIS instrument. This is the case for the emergence of a significant bias when dealing with more realistic images resulting from PSFs with great morphological complexity, namely those deriving from end-to-end simulation of the complete atmospheric and adaptive optics effects. This substantiates the possible inadequacy of approaches based on classical aperture photometry techniques, or variations thereof, for the analysis of sources resulting from such PSFs. These are usually not assumed as the main tool for precision astrometry, but they are often included as part of more substantial pipelines[9].

For pipelines such as the one considered in the present section, the errors propagated from the aperture photometry stage might be constant across the field and result only in a homogeneous

---

[9]Such as is the case here, and similarly with `DAOPhot`, where aperture photometry constitutes the first step for extracting high SNR samples for fitting an effective PSF model.

astrometric shift, thus inconsequential for relative astrometry and easily calibrated, e.g. in the presence of reference sources [16]. However, this might not be the case for AO-driven instruments, such as the METIS, where anisoplanatism might incur a variation - such as a tip/tilt drift - of the peak and morphology of the PSF, which is not constant across the field-of view.

As seen in Section 4.1.3, providing the PSF model directly in the pipeline mitigates this error[10], thus it can be considered as an effective calibration of this effect. As a result, the rigorous extraction of the system PSF associated with observations might be portrayed as a valuable asset for the characterisation of the system and calibration of the astrometry pipeline. This may be achieved by different approaches [63], such as:

- PSF extraction/fitting - such as some of the packages mentioned so far (e.g. `DAOPhot` [21], `SExtractor` [22], `StarFinder` [53, 54]), where point sources - effectively realisations of the PSF - are isolated from astronomic images and fitted to some basis - analytical or otherwise;

- PSF simulation - where based on system parameters and environmental data the PSF is simulated using some underlying analytical and/or empirical model (e.g. `COMPASS` [30], `OOMAO` [64], `SOAPY` [65]);

- PSF reconstruction - where the PSF is estimated from different data products from the telescope and instrument operation, such as system telemetry, AO telemetry and images, and atmosphere monitoring (e.g. [66], [67]);

amongst others, as well as hybrid approaches encompassing several of these methods.

4.2 Astrometric error budget

The generated images and, in consequence, the astrometric estimations established in the previous section encompass a limited set of effects that might contribute to the overall astrometric error demonstrated by the METIS instrument. As such, it is important to further analyse other effects that have been ommited and produce a more in-depth error budget estimation for this instrument.

In the remainder of this section, several sources of astrometric error are identified and their contribution to the error budget estimated based on results from the literature or theoretical considerations.

Measurement error

As discussed in Sec. 4.1, in ideal conditions - i.e. perfect detector and optical system, without atmosphere - the estimation of the centre of a point source is affected by a statistical measurement uncertainty governed by the SNR [60]:

$$\sigma_{\text{meas}} \approx \frac{\lambda}{\pi D} \frac{1}{\text{SNR}} \tag{4.2}$$

where D is the diameter of the telescope aperture.

Considering SNR = 100, one obtains:

---

[10]Mostly due to technical limitations, only the case where the field-constant PSF model for the centre is provided was analysed. This would effectively not solve the problem of calibration for field-variable errors. Nevertheless, this could be achieved provided one could supply `SExtractor` with multiple PSF models.

$$\sigma_{\mathrm{meas}} \approx 64\,\mu\mathrm{as}$$

Evidently, this is just a reference value and it should be adjusted according to the observation target and the exposure time - see Eq. (2.29).

Detector sampling

Detector sampling/binning errors are an intrinsic and unavoidable effect of digital imaging. For the MICADO instrument, this value is estimated to be $\sigma_{\mathrm{samp}} < 2\,\mu\mathrm{as}$ for bands I, J, H, and K considering pixel scales of $3\,\mathrm{mas/px}$; for $4\,\mathrm{mas/px}$ this value reaches $\sigma_{\mathrm{samp}} \approx 3\,\mu\mathrm{as}$ for the K band [16]. The METIS pixel scale is larger at $5.47\,\mathrm{mas/px}$, which leads to a decline in accuracy, though this is somewhat offset by the increase in wavelength of the L' band. Though no estimations are provided for this photometric band, henceforth it shall be assumed the placeholder value of:

$$\sigma_{\mathrm{samp}} = 5\,\mu\mathrm{as}$$

This value is significantly larger than the accuracy achieved during validation of the point source position method in Sec. 4.1. However, that estimation is provided for a noise-free isolated point source; for a more realistic case of a crowded field, this value might be considerably impaired [16]. The estimation considered above is a safer (albeit possibly over-estimated) value for the sampling error. More so, it should be noted that this effect is considerably less significant than others discussed before and from hereon, so slight under- or over-estimation should not be vastly consequential for the overall error estimation.

Telescope instabilities and geometric distortions

Telescope instabilities, such as optical misalignments and rotational errors, are significant contributors to the overall astrometric error of the ELT [40]. These phenomena result mostly in slow plate scale variations, translations, and rotations, which, luckily, can be easily and effectively calibrated by low-order corrections, though requiring frequent on-sky calibration - again, see [40].

Nevertheless, there are other effects which are non-linear and time-variable over small timescales, originating dynamic distortions which are not easily calibrated [16, 29]. These include, e.g. gravitational flexures, vibrations, and thermal variations. One example of this is the ELT secondary (M2) mirror, which due to its high mass and it being supported several meters above the primary mirror, is highly prone to wind disturbances and gravity flexures [36, 40].

In [16], it is assumed that the residuals of these effects amount to $\sim 0.01\,\mathrm{px}$ derived from the analysis in [68] for the WFC instrument aboard the HST. As stated, METIS has a fixed pixel scale of $5.47\,\mathrm{mas}$; thus, following this assumption, the distortions residuals will have a contribution of:

$$\sigma_{\mathrm{dist}} \approx 55\,\mu\mathrm{as}$$

For MICADO, it is proposed [16, 69] the use of an astrometric calibration mask (pinhole grid) in the focal plane of the imager. As far as it was able to uncover, this approach seems to have no parallel in the METIS instrument [70, 37]; thus the calibration efforts will need to rely on on-sky objects. As such, the actual calibration success and the resulting residuals may vary greatly depending on the observation target and the availability of good calibration targets.

Differential atmospheric refraction

Differential atmospheric refraction results from imaging two sources in different positions in the sky, resulting in the light propagation path presenting different refractive properties and, as a result, different apparent positions and separations of sources in the observed field-of-view. This effect can be generally separated into achromatic and chromatic contributions.

The achromatic manifestation of this effect results from differences in zenith angles of sources in the imaged field-of-view. In [71], this effect is estimated to amount to as much as several milliarcseconds of astrometric error for a imaged field-of-view similar to that of the METIS ($\approx 11'' \times 11''$). However, this is shown to be mostly a 1st order effect, with a quadratic term only amounting to:

$$\sigma_{\text{ADR}} \approx 2\,\mu\text{as}$$

The chromatic contribution arises from the dependence of the refractive index with wavelength and the consequent deviation in apparent position for sources of different colours. According to [72], this effect is not critical for current generation telescopes ($D \sim 8\,\text{m}$) operating in the MIR bands due to the relatively flat $n(\lambda)$ at these wavelengths. This is not the case, however, for next-generation ELTs [72, 73], where the use of an ADC might be required to mitigate this effect. This type of correction device is indeed included in the optical plan of the METIS [74], though little to no detail about this optical component was found in public literature. Thus, no further estimation of the impact of this effect on precision astrometry can be estimated. As a result, it is assumed as a placeholder the value adopted for the MICADO instrument in [16]:

$$\sigma_{\text{CDR}} \approx 20\,\mu\text{as}$$

Provided there is more information available regarding this matter, a more in-depth analysis of this effect is paramount. Nevertheless, it should be noted that this effect is only critical, as stated, for sources with different colour profiles; thus its pertinence is dependent on the observation target. Additionally, it can be minimised with the use of narrow-band filters.

Anisoplanatism and Differential tilt jitter

As seen in Sec. 2.1, the AO correction is prone to the effect of anisoplanatism, resulting in a degradation of the PSF Strehl ratio deriving from the angular separation of the observation target and the AO guide star. This degradation leads to a decrease in the SNR, which, in turn, results in an increased statistical measurement error - see Eq. (4.1). Nevertheless, a priori, this reduction in SNR is not expected to introduce a systematic astrometric error apart from the resulting decrease in peak flux. This is motivated further by [75], where it is seen that for the ELT SCAO case, the core of the PSF does not change drastically for angular separations to the guide source similar to the field-of-view of the METIS.

For simplicity, it is assumed that this effect does not incur in appreciable astrometric error for the SCAO case. The loss in measurement precision can be addressed, if needed, by adjusting the SNR of the detection due to anisoplanatism accordingly. Despite this, the variations of the morphology of the PSF may impact PSF extraction/modelling, which may lead to a degradation of the astrometric analysis. Although not detailed further, it is important to address and estimate this effect further in future work.

Another effect arises from the tip-tilt correction[11] of the AO system, in the case of METIS

---

[11]More intuitively, this corresponds to the correction of the 2D motion of the guide source in the image plane or, more correctly, the correction of the 2nd and 3rd Zernike modes [26] of the wavefront aberration.

achieved with the M5 mirror, and the differential offset between the guide star axis and the scientific source. More specifically, the traversal of the wavefront propagated by these two sources through different atmospheric patches (or *columns* results in a decorrelation in the tip-tilt components of the wavefront aberrations, which then might be well-estimated and well-corrected for the guide star, but erroneous for the science source, leading to an achromatic and anisotropic fluctuation in the relative distance of two objects [17]. This effect is known as *differential tilt jitter*, and its first order contribution is estimated by [76]:

$$\sigma_{\mathrm{TJ}} \propto \theta \times D^{-7/6} \times \left(\frac{\tau}{t}\right)^{1/2} \tag{4.3}$$

where θ is the angular separation of two sources, D is the telescope aperture diameter, τ is the aperture wind crossing time (approximately D divided by the wind speed), and t the integration time. Scaling the estimations for a SCAO system provided by [17, 16] assuming the ELT diameter, an exposure time of $t = 3600\,\mathrm{s}$, and $\theta = 10''$, the expected tilt jitter is:

$$\sigma_{\mathrm{TJ}} \approx 18\,\mu\mathrm{as}$$

which is a significant contribution for the overall astrometric error. This value can improved upon by increasing the exposure time, since $\sigma_{\mathrm{TJ}} \propto t^{-1/2}$, though the feasibility of longer exposure times for astrometric observation needs to be verified.

Nevertheless, the spatial correlation of this effect allows for a reduction of this error by a factor of ≈ 2 [16, **?**] by calibration of multiple frames; thus this value can ideally be reduced to:

$$\sigma_{\mathrm{TJ}} \approx 9\,\mu\mathrm{as}$$

It should be noted, however, that for the MCAO case (e.g. MICADO), this error can be reduced by a factor of ≈ 6 [16].

Sky-projected pixel scale and reference sources accuracy

Most of the various effects considered so far result in direct astrometric errors much greater than their specified contribution for the error budget. This is only possible due to all the calibration efforts relying on reference sources in the imaged frame. This is mostly done in the image space (i.e. in units of pixels in the raster frame). However, the pixel scale of the detector projected on-sky - allowing to convert detector positions into angular units - may require calibration using absolute positions of reference sources if the detector plane is tilted with respect to the focal plane [16]. As such, the absolute astrometric accuracy of the reference sources used for this purpose is a contributing factor to the success of the calibration and, as a result, of the relative astrometric accuracy achieved.

For the Galactic Centre, absolute astrometric accuracies of $\approx 1\,\mathrm{mas}$ have been achieved [77]. As defined in [16], for the field-of-view of the METIS ($\approx 11'' \times 11''$), this leads to a relative scaling accuracy of:

$$\delta x/x \approx 1\,\mathrm{mas}/11'' \approx 9.1 \times 10^{-5}$$

which results in a pixel scale error of:

$$\sigma_{\mathrm{scale}} = 46\,\mu\mathrm{as}$$

over an angular distance of $500\,\mathrm{mas}$ - a usual region of interest for the proposed science case, see e.g. [16].

Table 4.1: Astrometric error budget for the MICADO and METIS instruments. The values presented are the root-mean-square (RMS) constitutions of each noise component. (**TBD**=To Be Determined)

	MICADO	METIS
Measurement error (σ_{meas})	$34\,\mu$as	$64\,\mu$as
Detector Sampling (σ_{samp})	$1\,\mu$as	$5\,\mu$as
Geometric distortions (σ_{dist})	$30\,\mu$as	$55\,\mu$as
Achromatic differential refraction (σ_{ADR})	$1\,\mu$as	$2\,\mu$as
Chromatic differential refraction (σ_{CDR})	$20\,\mu$as	$20\,\mu$as
Differential tilt jitter (σ_{TJ})	$2\,\mu$as	$10\,\mu$as
Anisoplanatism (σ_{aniso})	$8\,\mu$as	TBD
Sky-projected pixel scale (σ_{scale})	$10\,\mu$as	$46\,\mu$as
Total ($\sqrt{\sum_i \sigma_i^2}$)	$51\,\mu$as	$99\,\mu$as

In comparison, due to the larger field-of-view of the MICADO instrument ($\approx 50'' \times 50''$), this contribution might be reduced up to a factor of ≈ 5 in comparison with the present case.

4.2.1 Discussion

Over the course of this section, several effects and sources of astrometric error have been identified, and their respective impact on high-precision astrometric work was discussed. The proposed set of sources of error, although not exhaustive, consists of the major sources of astrometric error also identified for MICADO [16]. This allows for a direct comparison of the expected astrometric performance of the METIS instrument with MICADO, the flagship ELT instrument for high-precision astrometry. A comparative summary of the respective error budgets is presented in Tab. 4.1, including the total astrometric error defined by the root-mean-square of all error contributions:

$$\sigma_{\mathrm{tot}} = \sqrt{\sum_i \sigma_i^2} \tag{4.4}$$

The error budget for the MICADO is based on [16], though the values provided may differ from the specified in this work since they have been scaled as a result of some of the assumptions and parameters defined along the course of this section - e.g. by considering a smaller source separation and large exposure time for the estimation of the differential tilt jitter. Nevertheless, the overall estimation of these values follows that proposed in the cited paper, having only been adjusted with scaling laws presented therein and in referenced papers.

From Tab. 4.1, the total astrometic error expected for the METIS instrument is $\sigma_{\mathrm{total}} \approx 100\,\mu$as, approximately a factor of 2 increase in comparison with MICADO instrument. It is noticeable that two of the most significant motivators of this increase are the statistical measurement error, σ_{meas}, and the sky-projected pixel scale calibration, σ_{scale}, which are respectively a factor of ≈ 2 and ≈ 5 higher than estimated for the MICADO instrument. The estimation of these effects derives primarily from the intrinsic characteristics of the instrument itself: the measurement error is increased due to the longer wavelength of the MIR bands (L'/M vs. JHK) - see Eq. (4.1) -, whilst the pixel scale calibration suffers from the small field-of-view and the

limited separation of reference sources that derive from it. This arguably strengthens the proposition that contrary to MICADO, the METIS instrument was not catered for high-precision astrometry, as it was already hinted at previously in this work.

Additionally, the geometric distortions and dynamic telescope instabilities are one of the main limiting factors of astrometric precision, as noticeable directly from the provided estimation and also already identified in the literature [9]. Therefore, a more detailed analysis of their impact for the specific case of METIS - and MICADO as well - is needed. See [19] for an example of a more detailed discussion of these effects, namely in the astrometric error budget analysis of the Thirty Meter Telescope.

Finally, it should be noted the effect of anisoplanatism was disregarded, and other effects, e.g. achromatic differential refraction, were not properly validated for the present case. It is possible that from these it shall arise an increment to the error budget, thus reiterating the importance of further analysing these terms in future work.

In conclusion, it is expected that the METIS instrument will provide an appreciable astrometric precision in L' band direct imaging ($\approx 100\,\mu$as). However, this is not competitive with the high-precision astrometry-oriented MICADO instrument, also integral to the ELT, which is expected to achieve a positional precision of $\approx 50\,\mu$as - cf. [16] and Tab. 4.1. Similar astrometric precision has also been proposed for other ELT-class instruments - see e.g. the case for the Thirty Meter Telescope [19]. As such, the use of METIS as an alternative to the latter is expected to only be advisable in case the distinct wavelength bands (mid-infrared vsnear-infrared) fulfil the requirements of the specific science case under study in such a way that otherwise wouldn't be achievable with MICADO.

Nevertheless, following the discussion presented in Ch. 1, there are a plethora of science objectives that motivate the use of the MIR bands, including several studies related to the Galactic Centre. As such, the METIS holds critical importance in those bands and in pan-spectral studies, in symbiotic cooperation with the remaining ELT instruments.

Chapter 5

Conclusions and Outlook

As described in Ch. 1, this work has been motivated by two main research goals defined by the following questions:

- Are general-purpose photometry pipelines viable for the analysis of images of highly crowded fields provided by the ELT?

- What is the relative astrometry precision that one might expect from the ELT METIS?

To address these questions, in Ch. 2 and Ch. 3 it was described and validated the methodologies for generating realistic images from a catalogue of point sources and performing precision astrometry from the resulting images, respectively. Although the detailed description and validation of the generation pipeline in Ch. 2 is not of major direct scientific pertinence to the scientific goals of this thesis, it is a crucial step for assessing the correctness of the resulting images, and thus critical for guaranteeing the credibility of the results in subsequent chapters and of future work derived from the present thesis. Similarly, the comparison of existing photometry/astrometry software and the description of the adopted astrometry pipeline in Ch. 3, whilst not the core objective of this work, allowed to better grasp the working principles and limitations of the available offerings.

In Sec. 4.1, several images were analysed, ranging from the most simple case of using a Gaussian PSF to the realistic case of assuming a field-variable simulated METIS PSF - see Fig. 2.22. An important result verified throughout this section is that for the central values of magnitude, the astrometric precision was on par with the theoretical measurement limit. This is an important validation of the approaches to both the direct and the inverse problems.

Still, in this section, it was encountered a systematic astrometric bias for images based on the simulated METIS PSF. In the context of relative astrometry, this would not be problematic, granted that this effect was constant across the field or possible to be calibrated in the presence of sufficient reference sources. However, these conditions are not confirmed at this time. The source of this error was narrowed down to the initial aperture photometry step, but no specific description of the cause was obtained. As such, it is not known how the characteristics of the PSF motivate this bias and if it might variate along the field-of-view or differ for other atmospheric conditions, as an example. Nevertheless, calibration was revealed as not required if a correct PSF model was provided. Although in the present case the exact PSF was available, which might not be realistic in an actual observation, several approaches to obtain the observation's PSF were discussed - see Sec. 4.1.5.

The key conclusion of this section - and in answer to the first research goal - is that general photometry pipelines might not be adequate for working with the morphologically complex PSFs of AO-driven segmented-mirror ELTs. In the process of verifying this, it was also reiterated the importance of alternative methods for determining the empirical PSF associated with an observation. This necessity had already been identified to address the difficulties of PSF extraction in the crowded fields [9], though now its motivation is extended by the difficulties experienced in this work regarding PSF extraction in the context of the ELT, deriving from the morphology of its PSF.

Despite the usefulness of this development for assessing the usability of the `SExtractor` [22] package for high-precision astrometry work with ELTs, Sec. 4.1 was concluded to be rather inconsequential for the estimation of the actual achievable astrometric precision with the METIS instrument. This is motivated by several factors, including the astrometric precision limit achieved, which was possibly methodological in nature, the lack of several effects and sources of error discussed subsequently, and the unrealistic procedure of providing the real PSF in the astrometric analysis.

In sight of these limitations, a subsequent analysis of astronomic error contributions was executed based on literature review and theoretical estimations - cf. Sec. 4.2. In this section, several sources of significant astrometric error were identified and summarised in an error budget, leading to an estimate of $\approx 100\,\mu$as of predicted positional error in L' direct imaging. This allowed for direct comparison with the study case of the MICADO, the flagship high-precision astrometry instrument for the ELT, which is expected to achieve an astrometric precision of $\approx 100\,\mu$as. From the analysis of the error contributions, it is concluded that the METIS instrument is impacted in astrometric performance by its intrinsic characteristics, such as increased wavelength and a reasonably small field-of-view. This is further impacted by the omission of internal calibration devices specific for high-precision astrometric work.

Concluding, it has been demonstrated that the METIS will not be a flagship instrument for high-precision astrometric work, demonstrating worse astrometric precision than other instruments planned for ELTs [16, 19]. Nonetheless, it will enable observation of greater precision of current-generation telescopes - cf. Ch. 1 -, whilst operating in the MIR. This is a key motivator for the study of several science targets [13], since the majority of high-precision astrometry instruments have operated exclusively in the visible and near-infrared. Accompanied with its spectrographic capabilities - which were not addressed in this work - it is expected that the METIS will become an invaluable instrument for MIR and pan-spectral studies.

Future work

Various limitations and potential improvements were verified throughout this work. Additionally, the progress in the understanding of the photometric and astrometric capabilities of the METIS instrument harnessed in this thesis, along with the achieved maturity of the methodology used, establishes a solid basis for future endeavours related to the research goals considered. A brief overview of some of these limitations and proposed future developments is presented henceforth.

Firstly, improving the generation pipeline for precision astrometry work is crucial. This endeavour reveals two distinct facets. For one, additional effects that are yet to be included in the pipeline need to be modelled, implemented computationally, and integrated with the existing pipeline. On the other hand, regardless of its complexity or physical nature, any additional effect that is modelled requires to be well parameterised. Additionally, with more extensive and realistic images, the analysis of different observation strategies can also be addressed. In the course of this work, every image was obtained by integrating individual static frames. This is hardly a realistic case for actual observations in the MIR, where techniques such as jitter and nodding are often used. The correct modelling of additional effects - namely those explored in the astrometric error budget in Sec. 4.2 - is an important step to further improve the realism and completeness of the generated images and, consequently, allow for more detailed estimations of the astrometric errors budgets derived directly from the simulations.

Secondly, addressing the limitations encountered with the use of `ScopeSim`, it is of great importance to further investigate the optimisation of the astrometric pipeline. Additionally, it is critical to consider other software packages for this purpose to both establish a baseline and to verify if some of the effects encountered - namely, the astrometric bias and the limiting precision

- are replicated in other methodologies. With this analysis concluded, one might then address the wider problem of estimation and extraction of empirical PSFs, since it has been revealed to be a key method for achieving correct high-precision astrometry. Namely, it is of great interest to consider the various approaches for PSF reconstruction and extraction discussed in Sec. 4.1.5 in the specific context of ELTs.

Finally, either resulting from the analysis of improved simulated images or from additional system modelling and analysis, it is critical to further constrain the various contributions included in the error budget - some of which are simple rough estimations extrapolated from the analysis of the MICADO instrument.

Concluding, these summarise some of the numerous research topics that might derive from this work, and that are increasingly pertinent with the emergence of ELTs.

Appendix A

Testing the PSF grid interpolation method

In Sec. 2.1.1, an interpolation method was proposed for achieving a pseudo-continuous field-variable PSF from a grid of fiducial PSFs. As with any scientific algorithm, the proposed implementation's validity and correctness must be attested. Despite not providing an extensive testing scenario, some conditions - or, one might say, "sanity checks" - were idealised and tested. These are presented from hereon.

> **Condition 1:** The effective (interpolated) PSF (ePSF) funtion evaluated at some position (x_G, y_G) where the PSF grid is defined is identical to the fiducial PSF at said position:
>
> $$\mathbf{ePSF}(x_G, y_G, i, j) = \mathbf{PSF}(x_G, y_G, i, j)$$

This was tested by considering a PSF grid with a Gaussian PSF of FWHM = 5 px defined at the centre of the field. The interpolated PSF was calculated at that position, resulting in a maximum absolute error of $|\mathrm{ePSF} - \mathrm{PSF}| \approx 10^{-26}$ of normalised intensity.

> **Condition 2:** For any position in the detector frame, the resulting ePSF is normalised:
>
> $$\sum_{i=1}^{w} \sum_{j=1}^{h} \mathbf{ePSF}(x, y, i, j) = 1 \,, \; \forall \, x, y \in \mathbb{R}$$
>
> and the respective pixel intensity is preserved upon convolution.

This was tested for PSFs interpolated at positions $i = 0 \wedge j \in \{50k \,|\, k \in \{0, 1, 2, ..., 19\}\}$ and $i \in \{50k \,|\, k \in \{0, 1, 2, ..., 19\}\} \wedge j = 0$, with i, j raster coordinates with respect to the centre of the field. All PSFs were verified to integrate to unity with a relative error of $< 10^{-14}\,\%$. Similarly, convolution with a point source at the position where each PSF was defined resulted in preservation of its flux within an identical error.

> **Condition 3:** The ePSF function evaluated at the centre point of four positions of the PSF grid is equal to the mean of the respective PSFs defined in said positions.

A 3×3 PSF grid was defined at positions $i \in \{-1024, 0, 1024\}$ px $\wedge$ $j \in \{-1024, 0, 1024\}$ px, where i, j are the raster coordinates with respect to the centre of the field where the PSFs of the grid are defined. All the PSFs considered are Gaussian with a size of $128 \times 128\mathrm{px}^2$. The

full-width at half maximum of each Gaussian profile was defined as $\text{FWHM}_x = 5.0 + 5.0 \cdot |i_G| \, \text{px}$ and $\text{FWHM}_y = 5.0 + 5.0 \cdot |j_G| \, \text{px}$, where FWHM_x is the full-width at half maximum along the x direction, FWHM_y is the analogous quantity but for the y direction, and $i_G, j_G \in \{-1, 0, 1\}$ are the grid indices of the PSF.

To assert this conditions, the resulting PSF grid was interpolated at coordinates $(i, j) = (512, 512) \, \text{px}$, i.e. the centre point of the positions of the fiducialPSFs with grid indices $i_G, j_G \in \{0, 1\}$. From the comparison of the resulting PSF with the theoretical prediction - that is, the mean of these four PSFs - it was concluded that to a relative error of $\approx 10^{-16} \, \%$

This procedure was repeated for a similar grid assuming random fiducial PSFs with an uniform distribution $\text{PSF}(i_G, j_G, i, j) \in [0, 1)$ and subsequently normalised by their sum. The maximum relative error observed in this case was $< 10^{-17} \, \%$.

Condition 4: The convolution of a point-source frame with an ePSF mapping resulting from a grid comprised of identical fiducial PSFs provides the same result as the simple convolution of the point source with a single PSF equal to one that of the grid.

To test this, a square grid of 3×3 point sources with a separation of $\Delta = 500 \, \text{px}$ and centred at centre of the field was defined. Each of these sources was defined to have a dimensionless flux of 1.0.

As a baseline, an image was generated by the convolution of these point sources with a single Gaussian PSF of dimension $128 \times 128 \text{px}^2$ with $\text{FWHM} = 5 \, \text{px}$. This procedure was repeated for interpolated PSFs at each point source position using the proposed method. For this, a grid of identical PSFs was considered, each equal to the one used for the baseline case.

The subtraction of the resulting images lead to a maximum absolute (dimensionless) intensity error of $\max |I_{\text{interp}} - I_{\text{baseline}}| \approx 4.0 \times 10^{-17}$, a seemingly negligible difference[1] between the two approaches.

---

[1] As a reference, in these conditions the minimum pixel value of the central $9 \times 9 \text{px}^2$ patch of a point source ($> 90\%$ encircled energy) is $\sim 10^{-4}$.

Appendix B

Testing the PSF resampling method

In Sec. 2.1.2, a method for resampling PSF to different pixel scales was proposed. The reliance on `scipy` [33] - a well-established scientific package based on a test-driven development paradigm - offers some degree of confidence as to the correction of this method. Nevertheless, it is still critical to verify that its integration within the generation pipeline is correct. More so, the use of interpolation methods is expected to incur some degree of error in the resulting PSFs, for which its impact on the extraction of point sources needs to be estimated. With these objectives in mind, several conditions which should ideally be verified and associated tests are now explored.

> **Condition 1:** Two identical, normalised, and well-sampled analytical functions defined in differently sampled support arrays, i.e. assuming distinct pixel scales, should not present pixel intensity differences when interpolated to a common pixel scale.

To measure the error introduced by the interpolation process, two Gaussian PSF arrays[1] with a size of $128 \times 128 \text{px}^2$ and FWHM = 20.03 mas were defined, the first assuming a pixel scale of 5.47 mas/px, and the second with a pixel scale of 6.88 mas/px. These pixel scales correspond to those of the METIS LM imager detector and of the provided E2E PSFs, respectively.

The PSF with sparser pixel scale (6.88 mas/px) was interpolated to the finer scale (5.47 mas/px). From the resulting PSF - henceforth referred to as the *resampled PSF* - it was then subtracted the PSF originally defined in the finer pixel scale - the *direct PSF* or *baseline* from hereon. The resulting residuals of the subtraction for the central region of the PSFs are presented in Fig. B.1. For this central patch of $9 \times 9\text{px}^2$, corresponding to $> 99\%$ encircled energy, the relative error due to interpolation is $< 2.5\%$. For the centre pixel, the error is $\approx 0.1\%$.

The residuals due to the interpolation process are indeed mensurable, though not enough to require a complete alternative to the proposed method. Nevertheless, in the context of precision astrometry and photometry, it is important to acquire some intuiton of the impact on the profile of the PSF - and, in turn, of the resulting point-source objects - due to the interpolation residuals.

To test this, several noise-free images of single point sources near the centre of the field[2] were generated[3] using both the resampled PSF and the baseline PSF. Subsequently, the FWHM of the point source was estimated for every image generated by least-squares fitting of an analytical 2D Gaussian model - see Fig. B.2.

The difference in of the estimated FWHM is presented in Fig. B.3.

---

[1]Although these are vastly different from the METIS PSF, they can be analytically defined for different pixel scales, allowing for direct comparison between interpolated and directly defined PSF arrays.

[2]Namely, $i = 0 \land j \in \{0.05k \,|\, k \in \{0, 2, ..., 19\}\}$ and $i \in \{0.05k \,|\, k \in \{0, 2, ..., 19\}\} \land j = 0$, with i, j raster coordinates with respect to the centre of the field.

[3]This is achieved by the convolution of the PSF with a support frame defining the irradiance distribution function of the point sources - cf. Eq. (2.1). The precise definition of point sources in this support frame is discussed in the next section.
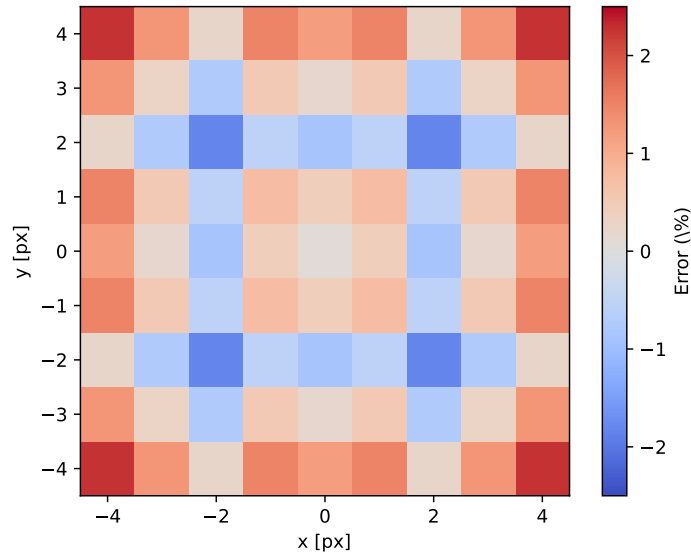
Figure B.1: Residuals map of the central region of the PSF due to pixel resampling (interpolation).
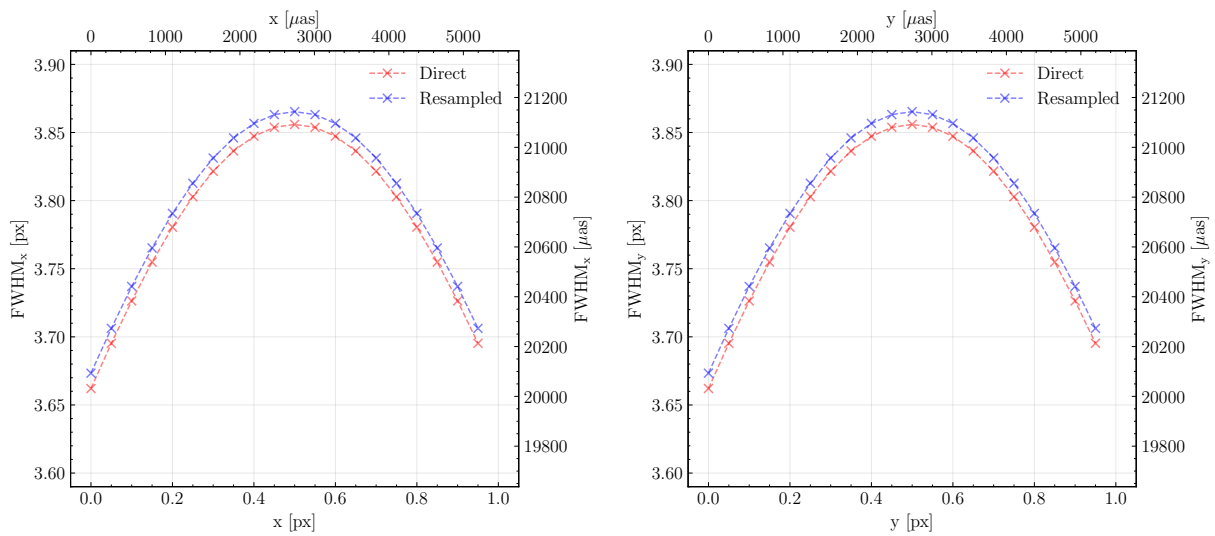
Figure B.2: Fitted values of the full width at half maximum (FWHM) of points sources generated with the direct and resampled PSFs for pixel positions $y = 0$ with variable x (left) and $x = 0$ with variable y (right)

Condition 2: The centroid of a point source generated with an interpolated PSF should be the same as that of a point source generated with a non-interpolated PSF of identical properties.

In the previous test, it has been concluded that the interpolation procedure introduces non-null residual variations in the resulting PSF. This was shown to affect the estimation of the FWHM of the Gaussian profile. As a result, these errors might impair the extraction of the centroid of a point source object.
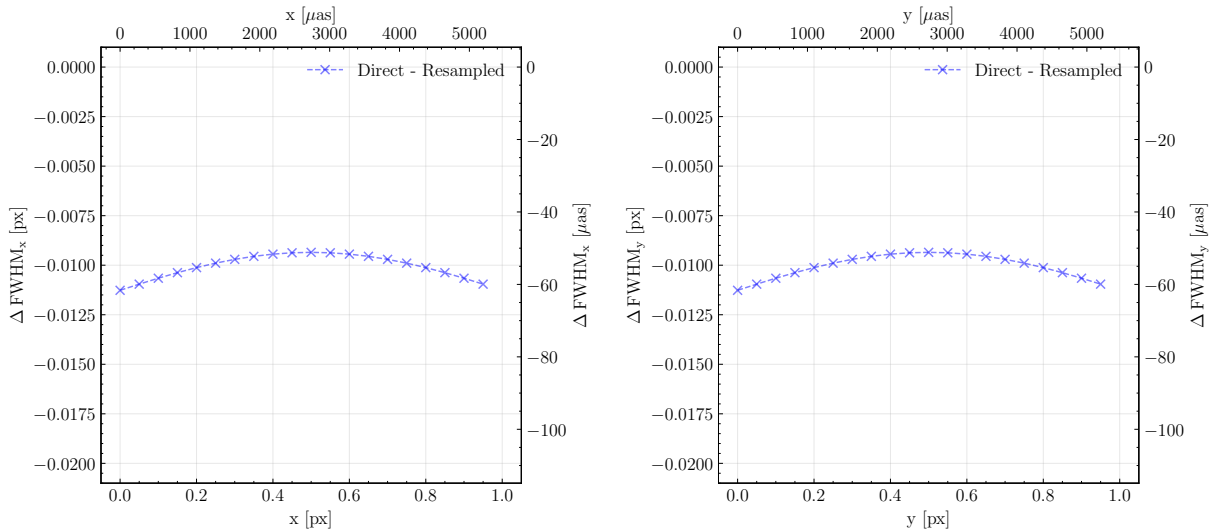
Figure B.3: Absolute difference of fitted values of the full width at half maximum (FWHM) of points sources generated with the direct and resampled PSFs

To test this hypothesis, for each generated imaged used in the previous test the centroid of the point source was estimated using the `fwcentroid` routine [35].
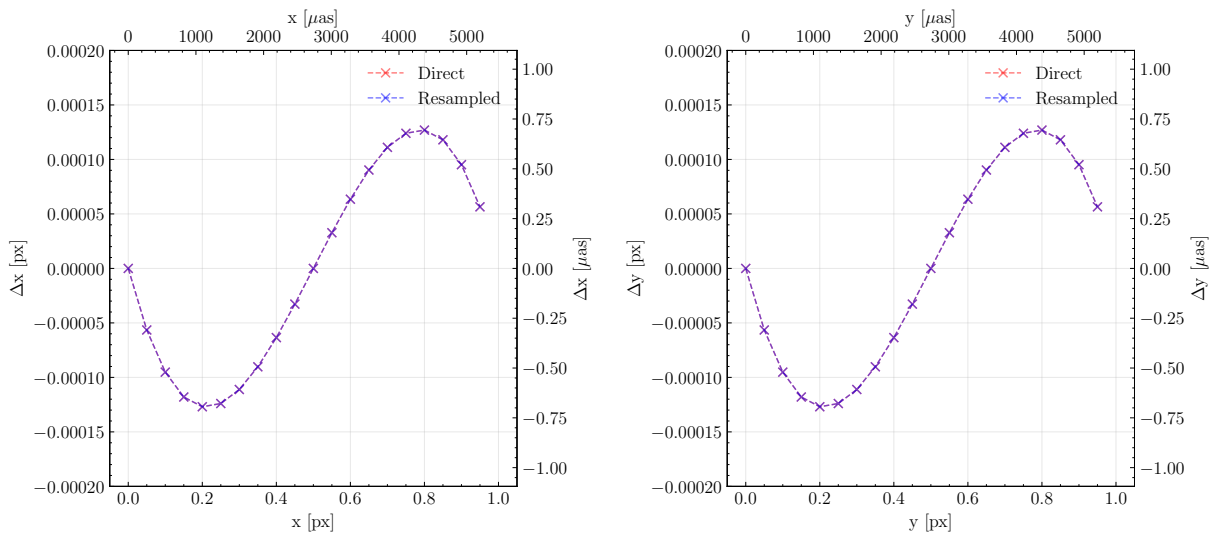
Figure B.4: Estimated x (left) and y (right) centroid coordinates of points sources generated with the direct and resampled PSFs for pixel positions $y = 0$ with variable x (left) and $x = 0$ with variable y (right)

It is interesting to note that there is some error in the centroid estimation which varies with the sub-pixel position of the respective point source object. This is the effect of *pixel phase errors*, and it shall be discussed in further detail in the following section. Regardless of this effect, the deviation of the point source centroid estimation using interpolated and non-interpolated PSFs is bounded to less than 3×10^{-8} px ($\approx 1.5 \times 10^{-4}\,\mu$as) - cf. Fig. B.5.
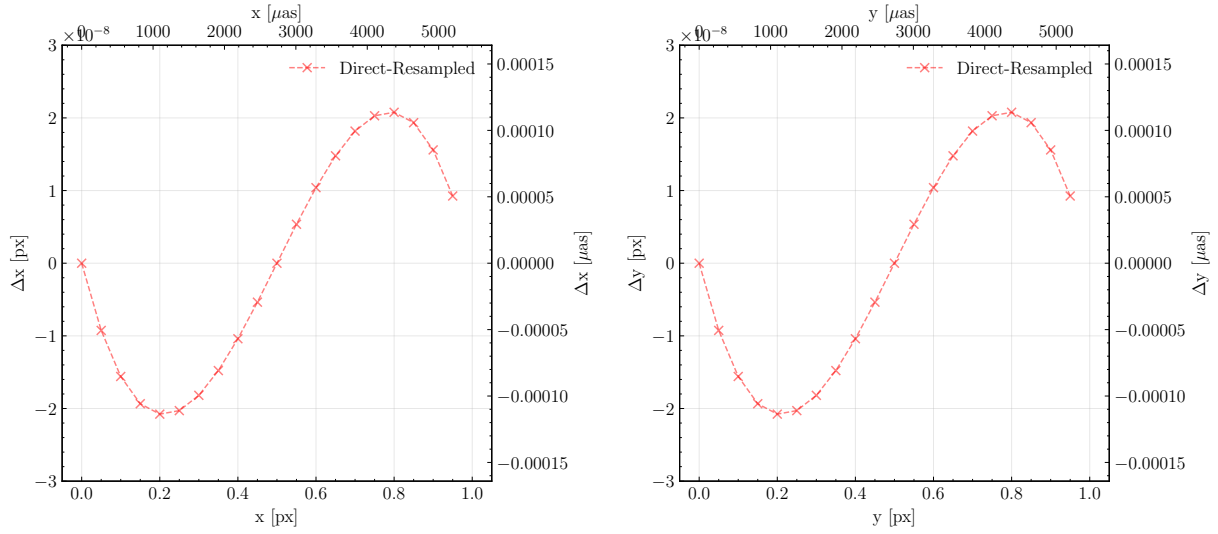
Figure B.5: Difference of estimated x (left) and y (right) centroid coordinates of points sources generated with the direct and resampled PSFs for pixel positions $y = 0$ with variable x (left) and $x = 0$ with variable y (right).

Condition 3: The interpolation of a normalised PSF should result in a PSF which is also normalised:
$$\sum_{i=1}^{w}\sum_{j=1}^{h}\mathbf{PSF}_{\text{interp}}(i,j) = 1$$

This was verified for every interpolated PSF considered in the previous test. Variations of the integral of the PSF were measured to be of the order of $10^{-9}\,\%$.

Appendix C

Intuition of the point source positioning approach

The discrete convolution of an image, f, by a kernel, h, is defined by:

$$f[i,j] * h[i,j] = \sum_{m=-\infty}^{\infty} \sum_{n=-\infty}^{\infty} f[m,n] \, h[i-m,j-n] \tag{C.1}$$

In this case, let us assume these to be a point-source frame, P, and a field-constant system point-spread function, PSF, respectively:

$$P[i,j] * \text{PSF}[i,j] = \sum_{m=-\infty}^{\infty} \sum_{n=-\infty}^{\infty} P[m,n] \, \text{PSF}[i-m,j-n] \tag{C.2}$$

Similarly, by commutativity:

$$P[i,j] * \text{PSF}[i,j] = \sum_{m=-\infty}^{\infty} \sum_{n=-\infty}^{\infty} \text{PSF}[m,n] \, P[i-m,j-n] \tag{C.3}$$

So far, it has been assumed that the entities PSF and P are defined for $m,n \in (-\infty, \infty)$ with, naturally, non-null values only for i,j of interest. Let us assume that we have a single point source at position (x,y) such that, by the previous approach, $P[i,j]$ is non-null for $i \in \{x_1, x_2\} \wedge j \in \{y_1, y_2\}$ - the four neighbouring pixels. As such, equation (C.3) is reduced to:

$$
\begin{aligned}
P[i,j] * \text{PSF}[i,j] \;=\; & P(x_1, y_1) \cdot \text{PSF}[i-x_1, j-y_1] \\
& + P(x_2, y_1) \cdot \text{PSF}[i-x_2, j-y_1] \\
& + P(x_1, y_2) \cdot \text{PSF}[i-x_1, j-y_2] \\
& + P(x_2, y_2) \cdot \text{PSF}[i-x_2, j-y_2]
\end{aligned}
\tag{C.4}
$$

By Eq. (2.15), this can be rewritten as:

$$
\begin{aligned}
P[i,j] * \text{PSF}[i,j] \;=\; P_s \cdot [\; & (x_2 - x)(y_2 - y) \cdot \text{PSF}[i-x_1, j-y_1] \\
& -(x_1 - x)(y_2 - y) \cdot \text{PSF}[i-x_2, j-y_1] \\
& -(x_2 - x)(y_1 - y) \cdot \text{PSF}[i-x_1, j-y_2] \\
& +(x_1 - x)(y_1 - y) \cdot \text{PSF}[i-x_2, j-y_2] \;]
\end{aligned}
\tag{C.5}
$$

Apart from a normalisation factor omitted here, equation (C.5) is similar to the bi-linear interpolation of the fiducial PSF grid in Eq. (2.12). However, contrarily to the former case, the interpolation in Eq. (C.5) does not represent an interpolation of different PSFs defined at various positions in the field; instead, it defines the interpolation of the same PSF shifted by $i \in \{0, 1\} \wedge j \in \{0, 1\}$ pixels. Ergo, we arrive at an intuitive description of the implication of the

method proposed: the convolution of a system PSF with a point source defined by the $2 \times 2\text{px}^2$ kernel as described in this section is equivalent to the convolution of the a point source defined by the closest $1 \times 1\text{px}^2$ detector pixel area - i.e. the previous approach - with a PSF resampled assuming a sub-pixel shift equal the error inherent to the discrete quantisation of the position of said point source.

Appendix D

Settings

Listing D.1: Settings used for the first run of aperture photometry using SExtractor

```
# Catalog
CATALOG_NAME       tmp.cat
CATALOG_TYPE       FITS_LDAC
PARAMETERS_NAME    param_prepsfex.sex

# Extraction
DETECT_TYPE        CCD
DETECT_MINAREA     5
DETECT_THRESH      10.0
ANALYSIS_THRESH    10.0
FILTER             Y
FILTER_NAME        /opt/homebrew/share/sextractor/gauss_2.0_5x5.conv
DEBLEND_NTHRESH    64
DEBLEND_MINCONT    0.1
CLEAN              Y
CLEAN_PARAM        1.0
MASK_TYPE          CORRECT

# Background
BACK_SIZE          256
BACK_FILTERSIZE    5
BACKPHOTO_TYPE     GLOBAL

# Photometry
PHOT_APERTURES     20
PHOT_AUTOPARAMS    2.5, 3.5
SATUR_LEVEL        2160000000.0
MAG_ZEROPOINT      0.0
MAG_GAMMA          4.0
GAIN               1.0
PIXEL_SCALE        0
```

Listing D.2: Settings used for PSF extraction using `SExtractor`

```
#  PSF model
BASIS_TYPE       PIXEL_AUTO
BASIS_NUMBER     20
BASIS_SCALE      1.0
PSF_SAMPLING     0
PSF_PIXELSIZE    1.0
PSF_ACCURACY     0.01
PSF_SIZE         55,55
PSF_RECENTER     Y
MEF_TYPE         INDEPENDENT


#   Point source measurements
CENTER_KEYS      XWIN_IMAGE,YWIN_IMAGE
PHOTFLUX_KEY     FLUX_BEST(1)
PHOTFLUXERR_KEY  FLUXERR_BEST(1)


#  PSF variability
PSFVAR_KEYS      XWIN_IMAGE,YWIN_IMAGE
PSFVAR_GROUPS    1,2
PSFVAR_DEGREES   7,7
PSFVAR_NSNAP     21,21
HIDDENMEF_TYPE   COMMON
STABILITY_TYPE   EXPOSURE


#  Sample selection
SAMPLE_AUTOSELECT    Y
SAMPLEVAR_TYPE       SEEING
SAMPLE_FWHMRANGE     1.0,5.0
SAMPLE_VARIABILITY   0.2
SAMPLE_MINSN         20
SAMPLE_MAXELLIP      0.3
SAMPLE_FLAGMASK      0x00fe
SAMPLE_WFLAGMASK     0x00ff
SAMPLE_IMAFLAGMASK   0x0
BADPIXEL_FILTER      N
BADPIXEL_NMAX        0
```

Listing D.3: Settings used for the final run of PSF photometry using `SExtractor`

```
# Catalog
CATALOG_NAME        tmp.cat
CATALOG_TYPE        FITS_1.0
PARAMETERS_NAME     param.sex

# Extraction
DETECT_TYPE         CCD
DETECT_MINAREA      5
DETECT_THRESH       2.0
ANALYSIS_THRESH     2.0
FILTER              Y
FILTER_NAME         /opt/homebrew/share/sextractor/gauss_3.0_5x5.conv
DEBLEND_NTHRESH     64
DEBLEND_MINCONT     0.1
CLEAN               Y
CLEAN_PARAM         1.0
MASK_TYPE           CORRECT

# Photometry
PHOT_APERTURES      20
PHOT_AUTOPARAMS     2.5, 3.5
SATUR_LEVEL         2160000000.0
MAG_ZEROPOINT       0.0
MAG_GAMMA           4.0
GAIN                1.0
PIXEL_SCALE         0

# Background
BACK_SIZE           256
BACK_FILTERSIZE     5
BACKPHOTO_TYPE      GLOBAL
```

Bibliography

[1] J.W. Hardy. *Adaptive Optics for Astronomical Telescopes*. Oxford series in optical and imaging sciences. Oxford University Press, 1998.

[2] *THE E-ELT CONSTRUCTION PROPOSAL*.

[3] Bernhard R. Brandl, Olivier Absil, Tibor Agócs, Nicola Baccichet, Thomas Bertram, Felix Bettonvil, Roy van Boekel, Leonard Burtscher, Ewine van Dishoeck, Markus Feldt, Paulo J. V. Garcia, Alistair Glasse, Adrian Glauser, Manuel Güdel, Christoph Haupt, Matthew A. Kenworthy, Lucas Labadie, Werner Laun, Dirk Lesman, Eric Pantin, Sascha P. Quanz, Ignas Snellen, Ralf Siebenmorgen, and Hans van Winckel. Status of the mid-IR ELT imager and spectrograph (METIS). In Christopher J. Evans, Luc Simard, and Hideki Takami, editors, *Ground-based and Airborne Instrumentation for Astronomy VII*, volume 10702, page 107021U. International Society for Optics and Photonics, SPIE, 2018.

[4] Karen M. Hampson, Raphaël Turcotte, Donald T. Miller, Kazuhiro Kurokawa, Jared R. Males, Na Ji, and Martin J. Booth. Adaptive optics for high-resolution imaging. *Nature Reviews Methods Primers 2021 1:1*, 1:1–26, 10 2021.

[5] R. Schödel, T. Ott, R. Genzel, R. Hofmann, M. Lehnert, A. Eckart, N. Mouawad, T. Alexander, M. J. Reid, R. Lenzen, M. Hartung, F. Lacombe, D. Rouan, E. Gendron, G. Rousset, A.-M. Lagrange, W. Brandner, N. Ageorges, C. Lidman, A. F. M. Moorwood, J. Spyromilio, N. Hubin, and K. M. Menten. A star in a 15.2-year orbit around the supermassive black hole at the centre of the milky way. *Nature*, 419:694–696, 10 2002.

[6] S. Gillessen, F. Eisenhauer, S. Trippe, T. Alexander, R. Genzel, F. Martins, and T. Ott. Monitoring stellar orbits around the massive black hole in the galactic center. *The Astrophysical Journal*, 692:1075–1109, 2 2009.

[7] A. M. Ghez, M. Morris, E. E. Becklin, A. Tanner, and T. Kremenek. The accelerations of stars orbiting the milky way's central black hole. *Nature*, 407:349–351, 9 2000.

[8] A. M. Ghez, S. Salim, N. N. Weinberg, J. R. Lu, T. Do, J. K. Dunn, K. Matthews, M. R. Morris, S. Yelda, E. E. Becklin, T. Kremenek, M. Milosavljevic, and J. Naiman. Measuring distance and properties of the milky way's central supermassive black hole with stellar orbits. *The Astrophysical Journal*, 689:1044–1062, 12 2008.

[9] T. Fritz, S. Gillessen, S. Trippe, T. Ott, H. Bartko, O. Pfuhl, K. Dodds-Eden, R. Davies, F. Eisenhauer, and R. Genzel. What is limiting near-infrared astrometry in the galactic centre? *Monthly Notices of the Royal Astronomical Society*, 401:1177–1188, 1 2010.

[10] E. Gendron, Y. Clénet, T. Fusco, and G. Rousset. New algorithms for adaptive optics point-spread function reconstruction. *Astronomy Astrophysics*, 457:359–363, 10 2006.

[11] S. Gillessen, F. Eisenhauer, G. Perrin, W. Brandner, C. Straubmeier, K. Perraut, A. Amorim, M. Schöller, C. Araujo-Hauck, H. Bartko, H. Baumeister, J.-P. Berger, P. Carvas, F. Cassaing, F. Chapron, E. Choquet, Y. Clenet, C. Collin, A. Eckart, P. Fedou, S. Fischer, E. Gendron, R. Genzel, P. Gitton, F. Gonte, A. Gräter, P. Haguenauer, M. Haug,

X. Haubois, T. Henning, S. Hippler, R. Hofmann, L. Jocou, S. Kellner, P. Kervella, R. Klein, N. Kudryavtseva, S. Lacour, V. Lapeyrere, W. Laun, P. Lena, R. Lenzen, J. Lima, D. Moratschke, D. Moch, T. Moulin, V. Naranjo, U. Neumann, A. Nolot, T. Paumard, O. Pfuhl, S. Rabien, J. Ramos, J. M. Rees, R.-R. Rohloff, D. Rouan, G. Rousset, A. Sevin, M. Thiel, K. Wagner, M. Wiest, S. Yazici, and D. Ziegler. Gravity: a four-telescope beam combiner instrument for the vlti. page 77340Y, 7 2010.

[12] R. Abuter, M. Accardo, A. Amorim, N. Anugu, G. Ávila, N. Azouaoui, M. Benisty, J. P. Berger, N. Blind, H. Bonnet, P. Bourget, W. Brandner, R. Brast, A. Buron, L. Burtscher, F. Cassaing, F. Chapron, É. Choquet, Y. Clénet, C. Collin, V. Coudé du Foresto, W. de Wit, P. T. de Zeeuw, C. Deen, F. Delplancke-Ströbele, R. Dembet, F. Derie, J. Dexter, G. Duvert, M. Ebert, A. Eckart, F. Eisenhauer, M. Esselborn, P. Fédou, G. Finger, P. Garcia, C. E. Garcia Dabo, R. Garcia Lopez, E. Gendron, R. Genzel, S. Gillessen, F. Gonte, P. Gordo, M. Grould, U. Grözinger, S. Guieu, P. Haguenauer, O. Hans, X. Haubois, M. Haug, F. Haussmann, Th. Henning, S. Hippler, M. Horrobin, A. Huber, Z. Hubert, N. Hubin, C. A. Hummel, G. Jakob, A. Janssen, L. Jochum, L. Jocou, A. Kaufer, S. Kellner, S. Kendrew, L. Kern, P. Kervella, M. Kiekebusch, R. Klein, Y. Kok, J. Kolb, M. Kulas, S. Lacour, V. Lapeyrère, B. Lazareff, J.-B. Le Bouquin, P. Lèna, R. Lenzen, S. Lévêque, M. Lippa, Y. Magnard, L. Mehrgan, M. Mellein, A. Mérand, J. Moreno-Ventas, T. Moulin, E. Müller, F. Müller, U. Neumann, S. Oberti, T. Ott, L. Pallanca, J. Panduro, L. Pasquini, T. Paumard, I. Percheron, K. Perraut, G. Perrin, A. Pflüger, O. Pfuhl, T. Phan Duc, P. M. Plewa, D. Popovic, S. Rabien, A. Ramírez, J. Ramos, C. Rau, M. Riquelme, R.-R. Rohloff, G. Rousset, J. Sanchez-Bermudez, S. Scheithauer, M. Schöller, N. Schuhler, J. Spyromilio, C. Straubmeier, E. Sturm, M. Suarez, K. R. W. Tristram, N. Ventura, F. Vincent, I. Waisberg, I. Wank, J. Weber, E. Wieprecht, M. Wiest, E. Wiezorrek, M. Wittkowski, J. Woillez, B. Wolff, S. Yazici, D. Ziegler, and G. Zins. First light for gravity: Phase referencing optical interferometry for the very large telescope interferometer. *Astronomy Astrophysics*, 602:A94, 6 2017.

[13] E-rep-eth-met-1014 - metis science case. 2019.

[14] R. G. Carlberg. An overview on extremely large telescope projects. *Proceedings of the International Astronomical Union*, 1:25–33, 11 2005.

[15] Bernhard R. Brandl, Rainer Lenzen, Eric Pantin, Alistair Glasse, Joris Blommaert, Lars Venema, Frank Molster, Ralf Siebenmorgen, Sarah Kendrew, Maarten Baes, Hermann Böhnhardt, Wolfgang Brandner, Ewine van Dishoeck, Thomas Henning, Hans Ullrich Käufl, Pierre-Olivier Lagage, Toby J. T. Moore, Christoffel Waelkens, and Paul van der Werf. Instrument concept and science case for the mid-ir e-elt imager and spectrograph metis. page 77352G, 7 2010.

[16] S. Trippe, R. Davies, F. Eisenhauer, N. M. Förster Schreiber, T. K. Fritz, and R. Genzel. High-precision astrometry with micado at the european extremely large telescope. *Monthly Notices of the Royal Astronomical Society*, 402:1126–1140, 2 2010.

[17] P. B. Cameron, M. C. Britton, and S. R. Kulkarni. Precision astrometry with adaptive optics. *The Astronomical Journal*, 137:83–93, 1 2009.

[18] R Davies, J Alves, Y Clénet, F Lang-Bardl, H Nicklas, J.-U. Pott, R Ragazzoni, E Tolstoy, P Amico, H Anwand-Heerwart, S Barboza, L Barl, P Baudoz, R Bender, N Bezawada, P Bizenberger, W Boland, P Bonifacio, B Borgo, T Buey, F Chapron, F Chemla, M Cohen, O Czoske, V Déo, K Disseau, S Dreizler, O Dupuis, M Fabricius, R Falomo, P Fedou, N Förster Schreiber, V Garrel, N Geis, H Gemperlein, E Gendron, R Genzel, S Gillessen,

M Glück, F Grupp, M Hartl, M Häuser, H.-J. Hess, R Hofferbert, U Hopp, V Hörmann, Z Hubert, E Huby, J.-M. Huet, V Hutterer, D Ives, A Janssen, W Jellema, W Kausch, F Kerber, H Kravcar, B Le Ruyet, K Leschinski, C Mandla, M Manhart, D Massari, S Mei, F Merlin, L Mohr, A Monna, N Muench, F Müller, G Musters, R Navarro, U Neumann, N Neumayer, J Niebsch, M Plattner, N Przybilla, S Rabien, R Ramlau, J Ramos, S Ramsay, P Rhode, A Richter, J Richter, H.-W. Rix, G Rodeghiero, R.-R. Rohloff, M Rosensteiner, G Rousset, J Schlichter, J Schubert, A Sevin, R Stuik, E Sturm, J Thomas, N Tromp, G Verdoes-Kleijn, F Vidal, R Wagner, M Wegner, W Zeilinger, J Ziegleder, B Ziegler, and G Zins. The micado first light imager for the elt: overview, operation, simulation. volume 10702, page 107021S. SPIE, 2018.

[19] Matthias Schoeck, Tuan Do, Brent L. Ellerbroek, Luc Gilles, Glen Herriot, Leo Meyer, Ryuji Suzuki, Lianqi Wang, and Sylvana Yelda. Thirty meter telescope astrometry error budget. page 91482L, 7 2014.

[20] Antonella Vallenari. The future of astrometry in space. *Frontiers in Astronomy and Space Sciences*, 5, 4 2018.

[21] Peter B. Stetson. Daophot - a computer program for crowded-field stellar photometry. *Publications of the Astronomical Society of the Pacific*, 99:191, 3 1987.

[22] E. Bertin and S. Arnouts. Sextractor: Software for source extraction. *Astronomy and Astrophysics Supplement Series*, 117:393–404, 6 1996.

[23] Scopesim.

[24] irdb.

[25] Andrei Nikolaevich Kolmogorov, V Levin, Julian Charles Roland Hunt, Owen Martin Phillips, and David Williams. The local structure of turbulence in incompressible viscous fluid for very large reynolds numbers. *Proceedings of the Royal Society of London. Series A: Mathematical and Physical Sciences*, 434:9–13, 1991.

[26] Robert J Noll. Zernike polynomials and atmospheric turbulence. *J. Opt. Soc. Am.*, 66:207–211, 3 1976.

[27] D L Fried. Optical resolution through a randomly inhomogeneous medium for very long and very short exposures. *J. Opt. Soc. Am.*, 56:1372–1379, 10 1966.

[28] J Osborn, R W Wilson, M Sarazin, T Butterley, A Chacón, F Derie, O J D Farley, X Haubois, D Laidlaw, M LeLouarn, E Masciadri, J Milli, J Navarrete, and M J Townson. Optical turbulence profiling with stereo-scidar for vlt and elt. *Monthly Notices of the Royal Astronomical Society*, 478:825–834, 7 2018.

[29] François Roddier. Adaptive optics in astronomy. *Adaptive Optics in Astronomy*, 6 1999.

[30] F. Ferreira, E. Gendron, G. Rousset, and D. Gratadour. Numerical estimation of wavefront error breakdown in adaptive optics. *Astronomy Astrophysics*, 616:A102, 8 2018.

[31] Jay Anderson and Ivan R. King. Toward high-precision astrometry with wfpc2. i. deriving an accurate point-spread function. *Publications of the Astronomical Society of the Pacific*, 112:1360–1382, 10 2000.

[32] Jay Anderson and Ivan R King. Psfs, photometry, and astronomy for the acs/wfc, 2 2006.

[33] Pauli Virtanen, Ralf Gommers, Travis E. Oliphant, Matt Haberland, Tyler Reddy, David Cournapeau, Evgeni Burovski, Pearu Peterson, Warren Weckesser, Jonathan Bright, Stéfan J. van der Walt, Matthew Brett, Joshua Wilson, K. Jarrod Millman, Nikolay Mayorov, Andrew R. J. Nelson, Eric Jones, Robert Kern, Eric Larson, C J Carey, İlhan Polat, Yu Feng, Eric W. Moore, Jake VanderPlas, Denis Laxalde, Josef Perktold, Robert Cimrman, Ian Henriksen, E. A. Quintero, Charles R. Harris, Anne M. Archibald, Antônio H. Ribeiro, Fabian Pedregosa, Paul van Mulbregt, and SciPy 1.0 Contributors. SciPy 1.0: Fundamental Algorithms for Scientific Computing in Python. *Nature Methods*, 17:261–272, 2020.

[34] STScI Development Team. synphot: Synthetic photometry using Astropy. Astrophysics Source Code Library, record ascl:1811.001, November 2018.

[35] Marshall Perrin, Joseph Long, Ewan Douglas, Anand Sivaramakrishnan, Christine Slocum, and others. POPPY: Physical Optics Propagation in PYthon. Astrophysics Source Code Library, record ascl:1602.018, February 2016.

[36] M. Cayrel. E-elt optomechanics: overview. page 84441X, 9 2012.

[37] Rainer Lenzen, Bernhard R. Brandl, Eric Pantin, Alistair Glasse, Joris Blommaert, Lars Venema, Rik ter Horst, Ad Oudenhuysen, Frank Molster, Ralf Siebenmorgen, Hermann Böhnhardt, Ewine van Dishoeck, Paul van der Werf, Wolfgang Brandner, Thomas Henning, Stefan Hippler, Pierre-Olivier Lagage, Toby J. T. Moore, Maarten Baes, Christoffel Waelkens, Chris Wright, Hans Ulrich Käufl, Sarah Kendrew, Remko Stuik, and Laurent Jolissaint. Metis: system engineering and optical design of the mid-infrared e-elt instrument. page 77357O, 7 2010.

[38] R. Stuik, L. Jolissaint, S. Kendrew, S. Hippler, B. Brandl, L. Venema, R. Lenzen, E. Pantin, J. Blommaert, and A. Glasse. The metis ao system: bringing extreme adaptive optics to the mid-ir. page 77363G, 7 2010.

[39] Tibor Agócs, Willem Jellema, Joost van den Born, Rik ter Horst, Peter Bizenberger, Nicola Baccichet, Christian Straubmeier, Sara Zuccon, María Concepción Cárdenas Vázquez, and Stephen Todd. End to end optical design and wavefront error simulation of metis. page 353. SPIE, 7 2018.

[40] G Rodeghiero, J-U Pott, C Arcidiacono, D Massari, M Glück, H Riechert, and E Gendron. The impact of elt distortions and instabilities on future astrometric observations. *Monthly Notices of the Royal Astronomical Society*, 479:1974–1985, 9 2018.

[41] Gabriele Rodeghiero, Carmelo Arcidiacono, Jörg-Uwe Pott, Saavidra Perera, Giorgio Pariani, Demetrio Magrin, Hannes Riechert, Martin Glück, Eric Gendron, Davide Massari, Jonas Sauter, Maximilian Fabricius, Maximilian Häberle, Sebastian Meßlinger, Ric Davies, Paolo Ciliegi, Matteo Lombini, and Laura Schreiber. Performance and limitations of using elt and mcao for 50 as astrometry. *Journal of Astronomical Telescopes, Instruments, and Systems*, 7, 8 2021.

[42] S. Noll, W. Kausch, M. Barden, A. M. Jones, C. Szyszka, S. Kimeswenger, and J. Vinther. An atmospheric radiation model for cerro paranal. *Astronomy Astrophysics*, 543:A92, 7 2012.

[43] A. Jones, S. Noll, W. Kausch, C. Szyszka, and S. Kimeswenger. An advanced scattered moonlight model for cerro paranal. *Astronomy Astrophysics*, 560:A91, 12 2013.

[44] K N Liou. *An Introduction to Atmospheric Radiation*, volume 84. Elsevier, 2002.

[45] F. Patat, S. Moehler, K. O'Brien, E. Pompei, T. Bensby, G. Carraro, A. de Ugarte Postigo, A. Fox, I. Gavignaud, G. James, H. Korhonen, C. Ledoux, S. Randall, H. Sana, J. Smoker, S. Stefl, and T. Szeifert. Optical atmospheric extinction over cerro paranal. *Astronomy Astrophysics*, 527:A91, 3 2011.

[46] Philip Massey and George H. Jacoby. CCD Data: The Good, The Bad, and The Ugly. In Steve B. Howell, editor, *Astronomical CCD Observing and Reduction Techniques*, volume 23 of *Astronomical Society of the Pacific Conference Series*, page 240, January 1992.

[47] W. J. Merline and Steve B. Howell. A Realistic Model for Point-sources Imaged on Array Detectors: The Model and Initial Results. *Experimental Astronomy*, 6(1-2):163–210, January 1995.

[48] E-spe-mpia-met-1060 exposure time calculator specification (private publication).

[49] Gallego-Cano E. Shahzamanian B. Gallego-Calvente A.T. Gardini A. Schoedel R., Nogueras-Lara F. Milky way nuclear star cluster hks photometry, 2020.

[50] R. Schödel, F. Nogueras-Lara, E. Gallego-Cano, B. Shahzamanian, A. T. Gallego-Calvente, and A. Gardini. The milky way's nuclear star cluster: Old, metal-rich, and cuspy. *Astronomy Astrophysics*, 641:A102, 9 2020.

[51] R. Schödel, F. Najarro, K. Muzic, and A. Eckart. Peering through the veil: near-infrared photometry and extinction for the galactic nuclear star cluster. *Astronomy and Astrophysics*, 511:A18, 2 2010.

[52] E Bertin. Automated morphometry with sextractor and psfex. volume 442, page 435, 7 2011.

[53] E Diolaiti, O Bendinelli, D Bonaccini, L Close, D Currie, and G Parmeggiani. Starfinder: a code for crowded stellar fields analysis. volume 216, page 623, 1 2000.

[54] E. Diolaiti, O. Bendinelli, D. Bonaccini, L. Close, D. Currie, and G. Parmeggiani. Analysis of isoplanatic high resolution stellar fields by the starfinder code. *Astronomy and Astrophysics Supplement Series*, 147:335–346, 12 2000.

[55] AFJ Moffat. A theoretical investigation of focal stellar images in the photographic emulsion and application to photographic photometry. *Astronomy and Astrophysics, Vol. 3, p. 455 (1969)*, 3:455, 1969.

[56] Kenneth Levenberg. A method for the solution of certain non-linear problems in least squares. *Quarterly of Applied Mathematics*, 2:164–168, 1944.

[57] Donald W. Marquardt. An algorithm for least-squares estimation of nonlinear parameters. *Journal of the Society for Industrial and Applied Mathematics*, 11:431–441, 6 1963.

[58] M.I.A. Lourakis. levmar: Levenberg-marquardt nonlinear least squares algorithms in C/C++. [web page] http://www.ics.forth.gr/~lourakis/levmar/, 2004.

[59] R. Schödel. Accurate photometry with adaptive optics in the presence of anisoplanatic effects with a sparsely sampled psf. *Astronomy and Astrophysics*, 509:A58, 1 2010.

[60] L. Lindegren. Photoelectric astrometry: a comparison of methods for precise image location. *International Astronomical Union Colloquium*, 48:197–217, 9 1978.

[61] Benoit Neichel, Jessica R. Lu, François Rigaut, S. Mark Ammons, Eleazar R. Carrasco, and Emmanuel Lassalle. Astrometric performance of the gemini multiconjugate adaptive optics system in crowded fields. *Monthly Notices of the Royal Astronomical Society*, 445:500–514, 11 2014.

[62] Tristan Roell, Andreas Seifahrt, and Ralph Neuhäuser. Search for extrasolar planets with high-precision relative astrometry by ground-based and single-aperture observations. *Proceedings of the International Astronomical Union*, 3:57–60, 10 2007.

[63] Olivier Beltramo-Martin, Sam Ragland, Romain Fétick, Carlos Correia, Trent Dupuy, Giulian Fiorentino, Thierry Fusco, Laurent Jolissaint, Sebastian Kamann, Antonino Marasco, Davide Massari, Benoit Neichel, Laura Schreiber, and Peter Wizinowich. Review of psf reconstruction methods and application to post-processing. page 5. SPIE, 12 2020.

[64] R. Conan and C. Correia. Object-oriented matlab adaptive optics toolbox. page 91486C, 8 2014.

[65] Andrew Reeves. Soapy: an adaptive optics simulation written purely in python for rapid concept development. page 99097F, 7 2016.

[66] Carlos M. Correia and Joel Teixeira. Anti-aliasing wiener filtering for wave-front reconstruction in the spatial-frequency domain for high-order astronomical adaptive-optics systems. *Journal of the Optical Society of America A*, 31:2763, 12 2014.

[67] J. Exposito, D. Gratadour, Y. Clénet, G. Rousset, and L. Mugnier. Estimation of errors on the psf reconstruction process for myopic deconvolution. pages 84475X–84475X–11, 9 2012.

[68] J. Anderson. Astrometry with the advanced camera: Psfs and distortion in the wfc and hrc. page 13, 1 2003.

[69] G. Rodeghiero, M. Sawczuck, J.-U. Pott, M. Glück, E. Biancalani, M. Häberle, H. Riechert, C. Pernechele, V. Naranjo, J. Moreno-Ventas, P. Bizenberger, S. Perera, and L. Lessio. Development of the warm astrometric mask for micado astrometry calibration. *Publications of the Astronomical Society of the Pacific*, 131:054503, 5 2019.

[70] Nicola Baccichet, Lucas Labadie, Steffen Rost, Christian Straubmeier, Michael Wiest, Leonard Burtscher, Tibor Agócs, Willem Jellema, Roy van Boekel, Adrian M. Glauser, Bernhard R. Brandl, Felix Bettonvil, Jeff Lynn, Andreas Eckart, and Ronald Roelfsema. The calibration unit of the mid-infrared e-elt instrument metis. page 330. SPIE, 7 2018.

[71] Joseph Gubler and David Tytler. Differential atmospheric refraction and limitations on the relative astrometric accuracy of large telescopes. *Publications of the Astronomical Society of the Pacific*, 110:738–746, 6 1998.

[72] Sarah Kendrew, Laurent Jolissaint, Richard J. Mathar, Remko Stuik, Stefan Hippler, and Bernhard Brandl. Atmospheric refractivity effects on mid-infrared elt adaptive optics. page 70155T, 7 2008.

[73] Andrew J. Skemer, Philip M. Hinz, William F. Hoffmann, Laird M. Close, Sarah Kendrew, Richard J. Mathar, Remko Stuik, Thomas P. Greene, Charles E. Woodward, and Michael S. Kelley. A direct measurement of atmospheric dispersion in n -band spectra: Implications for mid-ir systems on elts1. *Publications of the Astronomical Society of the Pacific*, 121:897–904, 8 2009.

[74] Bernhard Brandl, Felix Bettonvil, Roy van Boekel, Adrian Glauser, Sascha Quanz, Olivier Absil, António Amorim, Markus Feldt, Alistair Glasse, Manuel Güdel, Paul Ho, Lucas Labadie, Michael Meyer, Eric Pantin, Hans van Winckel, and The METIS Consortium. Metis: The mid-infrared elt imager and spectrograph. 2021.

[75] Y. Clénet, E. Gendron, D. Gratadour, G. Rousset, and F. Vidal. Anisoplanatism effect on the e-elt scao point spread function. a preserved coherent core across the field. *Astronomy Astrophysics*, 583:A102, 11 2015.

[76] Richard J. Sasiela. *Electromagnetic Wave Propagation in Turbulence*, volume 18. Springer Berlin Heidelberg, 1994.

[77] M. J. Reid, K. M. Menten, S. Trippe, T. Ott, and R. Genzel. The position of sagittarius a*. iii. motion of the stellar cusp. *The Astrophysical Journal*, 659:378–388, 4 2007.